POLITECNICO DI TORINO

Master Degree in Energy and Nuclear Engineering

Politecnico di Torino

Master Degree Thesis

Reduction of iron oxides for chemical looping technology through concentrated solar power

Supervisors

Prof. Davide PAPURELLO

Prof. Domenico FERRERO

PhD Francesco ORSINI

Candidate

Francesca MARINUCCI

November 2023

Abstract

Climate change is a crucial challenge for the entire humankind, resulting from too high anthropogenic emissions of greenhouse gases in the atmosphere.
The implications of global warming are huge and alarming, requiring us a deep, radical change and a gradual desertion of fossil fuels.
The production of syngas and hydrogen, a promising energy vector, is one of the available solutions to mitigate climate change.
In particular, hydrogen is able to store and deliever large amounts of energy per unit mass, without releasing carbon dioxide during the combustion.
Syngas is a mixture of mainly hydrogen and carbon monoxide, that acts as an intermediate for the generation of other high value products, such as methanol, gasoline, ammonia.
Among the several existing methods for the production of these two outputs, chemical looping technology through concentrated solar power (CSP) is definitely a rising star.
This technique involves a solid material, commonly called *oxygen carrier*, that is initially heated to obtain its reduction and the release of oxygen. In a subsequent exothermic process at a lower temperature, the oxygen carrier is re-oxidized by means of H_2O or CO_2, releasing H_2 or CO.
Concentrated solar power systems can provide the heat needed in the first step of these thermochemical processes, enabling the intermittent solar energy to be converted and stored into easily transportable and ready to use solar fuels.
In this work thesis iron oxides have been chosen as oxygen carriers, since they are characterized by large availability, low cost and environmental safety.
An experimental test (i.e. thermogravimetric analysis (TGA)) has been performed to investigate the behaviour of iron oxides undergoing 20 redox cycles at constant temperature (820°C).
Thus the efficiency of the two steps (reduction and oxidation) has been evaluated, showing good results.
At last a numerical simulation in COMSOL Multiphysics is presented, taking into account an actual solar receiver, belonging to the paraboloidal CSP system, located on the rooftop of the Energy Center, in Turin.
The aim was to obtain the temperature distribution of the cylindrical receiver, starting from experimental data about solar radiation and wind speed and a further simulation of the reduction reaction within the cylinder itself.

Alle mie nonne Assunta e Ada

Table of Contents

List of Tables

List of Figures

Chapter 1

Introduction

1.1 Climate change: the problem

Climate change is one of the most critical issues in the history of humankind, representing a crisis embedded in the social, economic and energetic fabric.
It is characterized by protracted variations in temperature and weather patterns, that have always been caused by the sun's activity and massive volcanic eruptions [1]. Nonetheless, since 1800s the paramount cause of climate change has been anthropogenic emissions.
Figure 1.1 shows how much the global average temperatures for the years 1850-2023 has been above or below the 1961-1990 average value. The result is that nowadays the global average temperature is 1,07 °C higher than that average temperature.

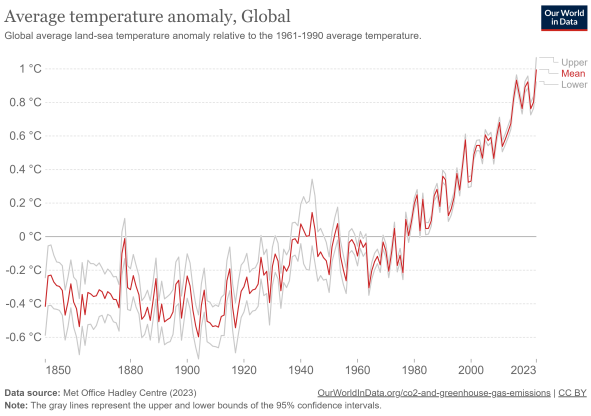

Figure 1.1: Global average temperature anomaly[2]

Unfortunately the increase of temperature is just the tip of the iceberg and the aftermaths of climate change are terrifying: rising sea levels, extreme weather events

(hurricanes, droughts, heat waves), destruction of natural habitats, extinction of certain species, more infectious diseases, water shortages, desertification.

The main cause of global warming is the excessive emission of greenhouse gases (GHG), such as carbon dioxide, methane, nitrous oxide, hydrochlorofluorocarbons (HCFCs) and ozone, that trap heat in the atmosphere.
Figure 1.2 depicts the global anthropogenic GHG emissions by gas, witnessing a predominance of CO_2 emissions over the others.

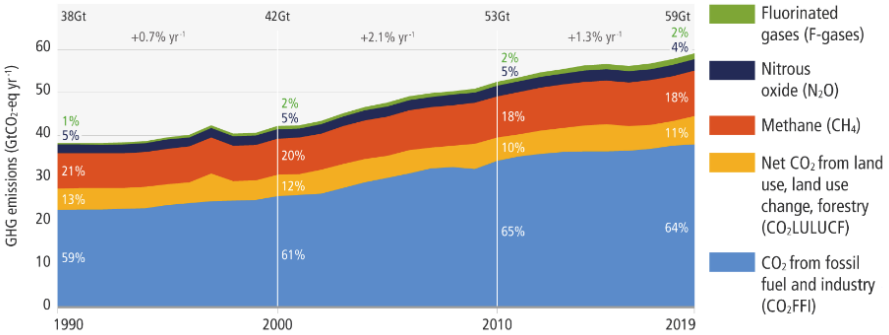

Figure 1.2: Global net anthropogenic emissions [3]

In fact, as shown in figure 1.3 CO_2 concentration in the atmosphere is getting higher and higher as time goes by, reaching the current value of 421 ppm [4].

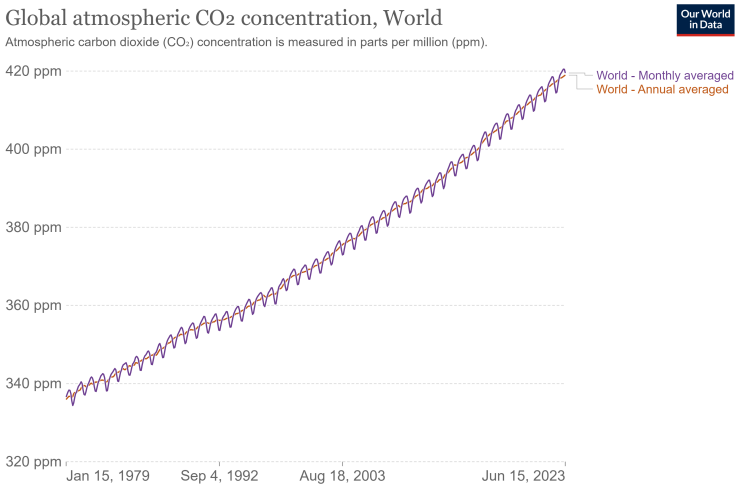

Figure 1.3: Global atmospheric CO_2 concentration [5]

Even though CO_2 has a GWP [1] equal to 1 (the lowest among all the GHGs), it is the one that lasts in the atmosphere the longest, with a lifetime of 1000 years.

Regarding the responsibility of climate change, figure 1.4 shows how much CO_2 each country emits every year. Asia is the region that emits the most CO_2 today with 53% of global emissions. In particular, China is by far the world's largest emitter with 10 billion tonnes of CO_2 every year (27% of global emissions). On the podium there are also USA with 15% of global emissions, followed by Europe [4].

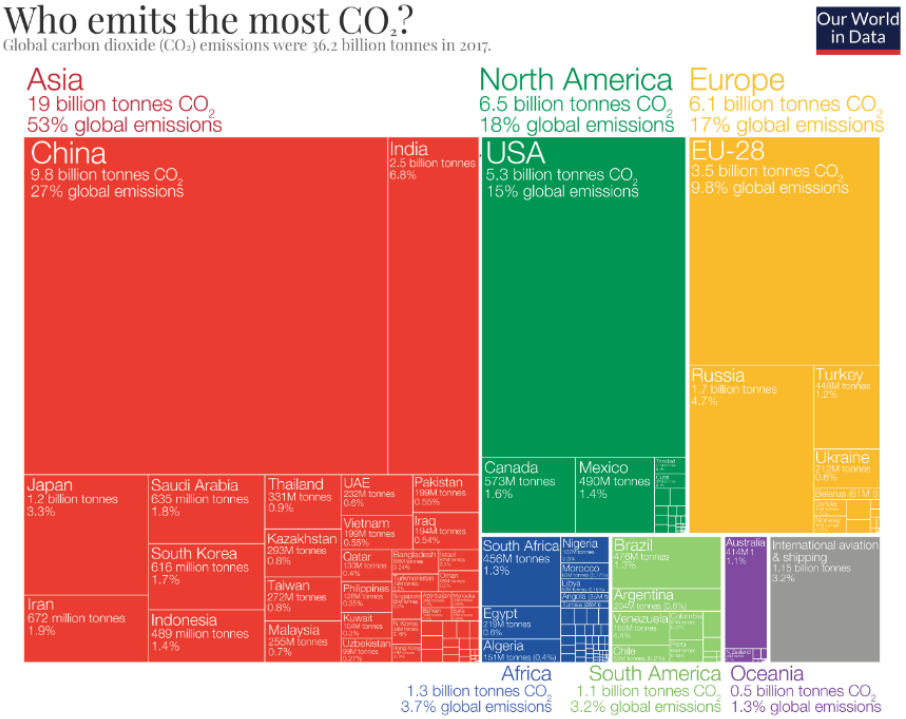

Figure 1.4: Treemap of CO_2 emissions by country [4]

However, taking a look at the CO_2 emissions throughout history (fig. 1.5), the outlook drastically changes: US and Europe knock China off the top spot with respectively 25% and 22% of responsability for the world's historical emissions[4].

[1]GWP is the Global Warming Potential, expressing a greenhouse gas's relative potency, considering how long the gas is active in the atmosphere, with respect to CO_2 (reference gas) [6]

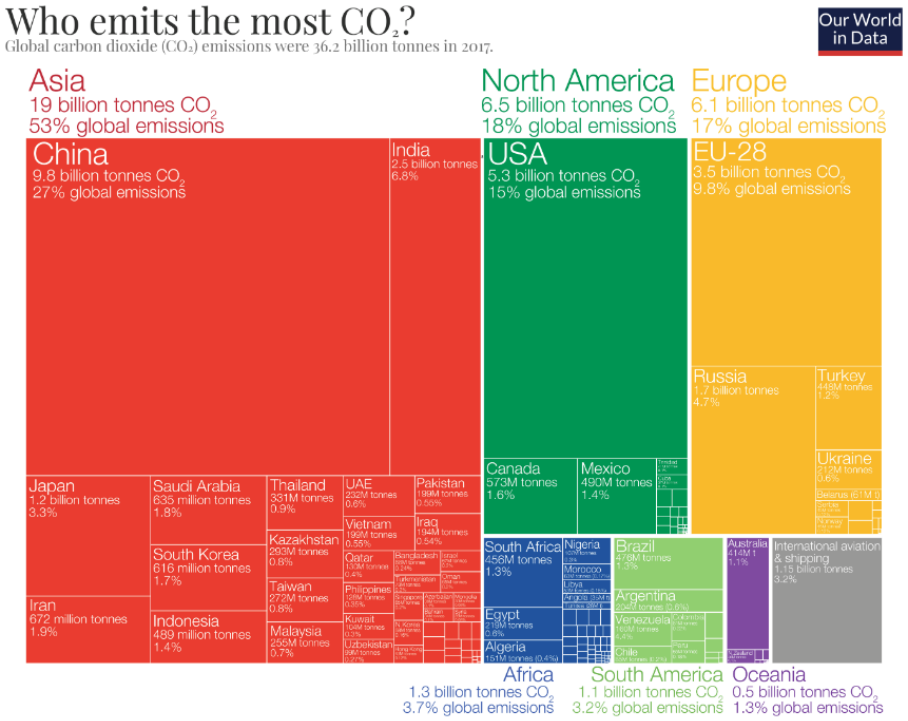

Figure 1.5: Cumulative CO_2 emissions by country [4]

It is also essential to highlight the fact that the distribution of the costs of global warming is uneven across the countries; indeed, much of the burden falls on developing countries, who were not even responsible for climate change in the first place. Thus, there is not only need for mitigation, but also for adaptation.
Moreover, in order to avoid poorer, developing countries to become as fossil fuel dependent as the richest countries are, the necessity of low cost and available low carbon technology is more and more urgent.

Taking into account the greenhouse gases in terms of sectors, figure 1.6 depicts, without surprises, that the most affecting one is the energy sector. The main source of emissions worldwide is the generation of electricity and heat, that together with the transport sector, achieve a 73,2% of the global emissions [7] .

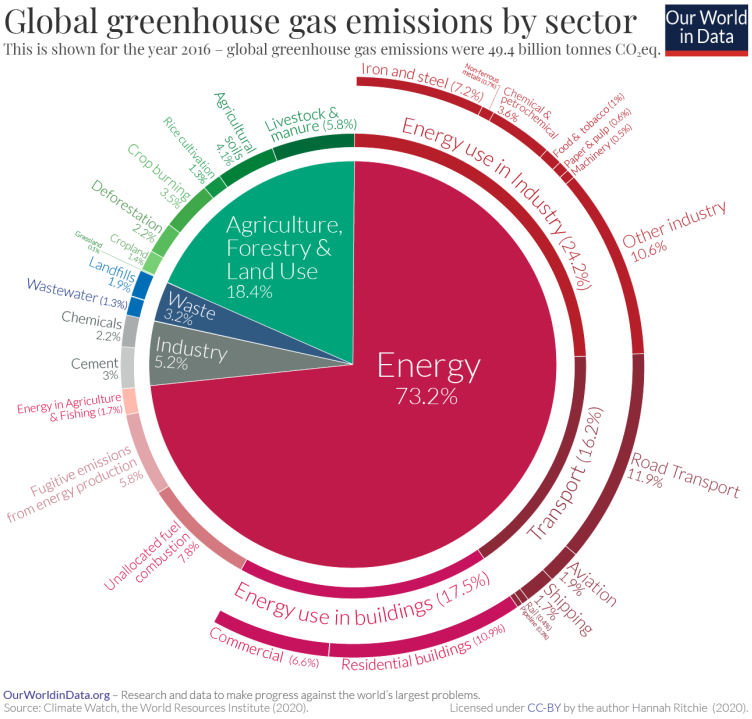

Figure 1.6: GHG emissions by sector [7]

1.2 Latest policies and solutions

The policy pathway regarding climate change started in the early 1990s with the Rio Earth Summit (1992), but focusing on the latest arrangements we can recall the Paris Agreement (COP21) of 2015; in this case, the goal was to limit the increase of temperature well below 2 °C with regard to pre-industrial levels and making efforts to remain below 1,5 °C.
In 2019 the Green Deal was introduced as the new strategy for a sustainable future, while leaving no one behind. It involves a new climate target with a reduction of the GHG emissions of at least 55% by 2030 compared to 1990 and climate neutrality by 2050 [8].

In order to achieve the goals set by these agreements, a decarbonisation of the energy sector is essential. However, this crucial step cannot be made out of the blue: fossil fuels will not disappear from Europe's energy mix in the short term.
In this framework, carbon capture, utilization and storage (CCUS) technologies can be seen as a feasible solution.
In CCUS, CO_2 is capture from sources of emissions, like industrial sites or power

plants that run on fossil fuels; if not immediately employed on-site, the compressed CO_2 is injected into profound geological formations or transferred via pipeline, ship, truck for use in a variety of applications.
Moreover, in the clean energy transition scenario, carbon capture, utilisation and storage can be used to retrofit existing power plants and to reduce emissions in difficult to abate industries (such as cement, steel, chemicals).
Furthermore, this technology can be also employed for the removal of CO_2 from the atmosphere, in order to compensate for emissions that are either inevitable or technically challenging to eliminate [9].
Nonetheless, CCUS technologies come with some remarkable challenges; first of all they are energy intensive, requiring large amounts of energy and thus consuming part of the power plant output itself.
Also the costs of these technologies are quite expensive: from the capital expenditures to the maintenance and operation ones, limiting the widespread adoption of CCUS.
At last the environmental risks should be taken into account, particularly regarding the underground storage of carbon dioxide and its possible leakages, that would compromise the aimed climate benefits.

Some of these issues may be overcome by exploiting the captured CO_2 for the production of high value outputs, such as *syngas*.
Synthetic gas is a flexible mixture mainly made up of carbon monoxide and hydrogen and varying amounts of carbon dioxide, methane, water vapor. It is characterized by high versatility, since it can be used for the production of ammonia (via the Haber process), liquid hydrocarbons (via the Fischer-Tropsch process) or methanol and consequently ethylene, dimethyl ether (DME), acetic acid [10].
In addition, syngas can be used as fuel for gas engines in power and heat generation systems. This last application is very appealing, since the global syngas demand is predicted to rise at an annual growth rate of 6,1% between 2020 and 2027 [11].

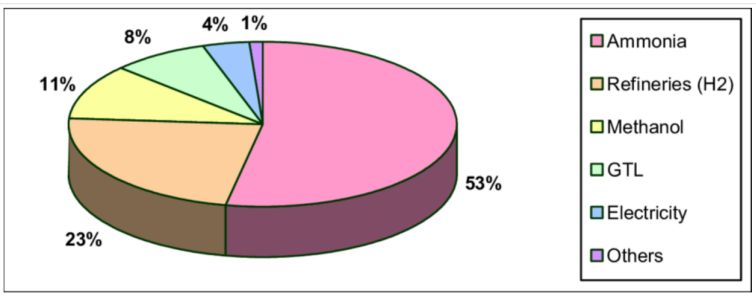

Figure 1.7: Current breakdown of world syngas market by application[12]

Regarding the production methods, syngas can be obtained from gasification of biomass or coal or through reforming of natural gas [13].
But our interest is focused on a greener and more sustainable production process of syngas: via chemical looping technology, coupled to concentrated solar power, yielding the useful *solar syngas*. It has to be noted that these thermochemical cycles can be used also for the solar hydrogen production.
Figure 1.8 shows a schematic illustration of the two steps of chemical looping technology, exploiting concentrated solar power, that will be deeply investigated in the following chapters.

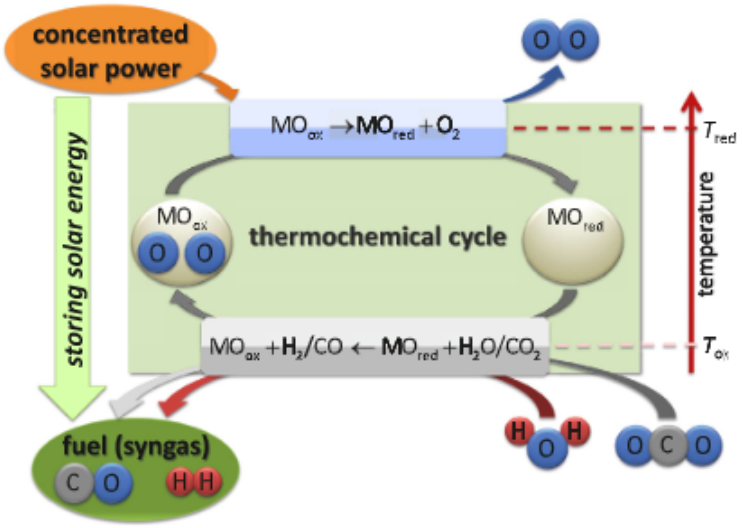

Figure 1.8: Solar syngas production via thermochemical cycles[14]

Hence the impact and the importance of solar-driven chemical looping processes is loud and clear in the energy context we are living in.

Chapter 2

Solar power

The goal of this chapter is a deep investigation of the Sun's structure and its radiation, which is a key aspect for the operation of concentrated solar power (CSP) plants.

2.1 The Sun

The Sun is a 4,5 billion year old star placed at the center of our solar system. It has a radius of about 695 000 kilometers (in other words, 109 times the one of the Earth) and a mass of about $2 \cdot 10^{30}$ kg.

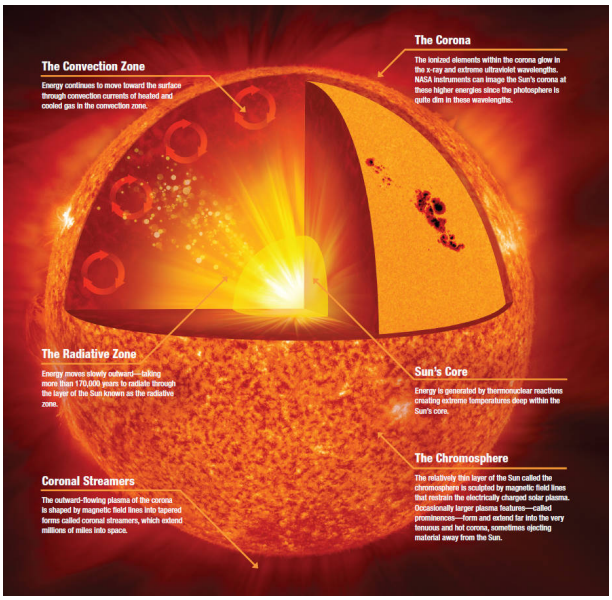

Figure 2.1: Anatomy of the Sun[15]

The Sun's mass is made of about 75% hydrogen, 23% helium and 2% other elements and shows a layered structure; in particular, moving from the outermost shell towards the inner ones we have:

- **Corona**: it consists of plasma and extends up to 20 solar radii.
- **Cromosphere**: it is a quite thin layer (around 10 000 km) with a slightly reddish color. Both the corona and the cromosphere are visible only during a solar eclipse.
- **Photosphere**: it is the visible surface of the Sun, characterized by very low density and a temperature of about 5800 K. It is also the surface from which the visible solar radiation is emitted into space.
- **Convective zone**: it extends from 0,7 solar radii to the entire solar radius. In this region the solar plasma shows very low density (0,15 g/m^3) and low temperature (2 000 000 K); as a consequence, the Sun's energy is transferred towards its surface by means of convective processes.
- **Radiative zone**: it extends from 0,23 to 0,7 solar radii, representing the thickest layer. Its temperature is about 7 000 000 K. The energy produced at the centre of the Sun is conveyed through radiative phenomena.
- **Core**: it extends up to 0,23 solar radii and it is the centre of the Sun. It shows very high temperature (about 15 000 000 K) as well as very high pressure and density.

Thus we can notice that temperature keeps on decreasing from the core to the chromosphere and then it increases in the corona. As regards density and pressure, they incessantly reduce from the core to the outer layers.
Furthermore, in the core we have the heat production by nuclear fusion processes, in which hydrogen is turned into helium, according to the equation 2.1:

$$4p^+ \rightarrow 4He^{2+} + 2e^+ + 2\nu + \Delta mc^2 \tag{2.1}$$

In the conversion from hydrogen protons into helium, there is also the release of positrons ($2e^+$), neutrino (2ν) and an energy production of 26,7 MeV, due to the mass defect that characterizes the process:

$$E = \Delta mc^2 = 26{,}7 \quad MeV \tag{2.2}$$

2.2 Solar radiation

The radiation energy released in the fusion processes occurring in the core is made up of a portion of solar wind, but mainly of electromagnetic radiation, that we exploit in the CSP systems.
In particular, the radiation spectrum of the Sun is very similar to the one of a black body at 5780 K. A black body is just a useful ideal construction, representing a body that absorbs all the incident electromagnetic radiation, whatever the frequency or the incident angle. Indeed, the name "black body" is related to the fact that it absorbs all colors of light. Starting from the radiation emitted by this kind of body, it is possible to derive the radiative behaviour of real bodies.
We can now introduce three different laws, interconnected to each other, that allow us to describe the phenomenon of the thermal radiation:

- **Planck's law**: it depicts the spectral distribution of the radiation of a black body, in thermal equilibrium at a certain temperature T. There are several forms of this law, depending on the spectral variables we take into account. The Planck's law expressed in terms of temperature T and wavelength λ is:

$$M(\lambda, T) = \frac{2\Pi h c^2}{\lambda^5} \frac{1}{\frac{hc}{e^{\lambda K T} - 1}} \tag{2.3}$$

  where:

  - $h = 6{,}626 \cdot 10^{-34}\ J \cdot s$ is the Planck constant
  - $K = 1{,}38 \cdot 10^{-23}\ J/K$ is the Boltzmann constant
  - $c = 3 \cdot 10^{8}\ m/s$ is the speed of light

  In picture 2.2 the spectral radiance of a black body at different temperatures, against wavelength is shown.

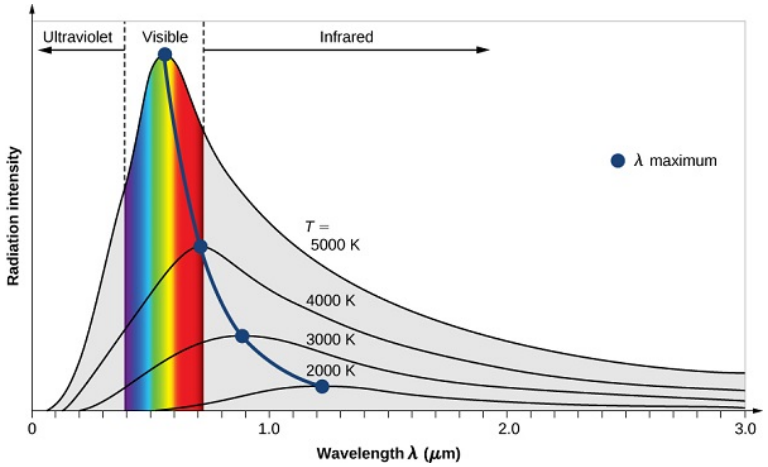

Figure 2.2: Spectral distribution of blackbody radiation at different temperatures[16]

It is clear that the thermal radiation shows a continuous spectrum. Moreover, each curve (characterized by a certain temperature) has a maximum value of the emitted radiation at a given wavelength and then it keeps on decreasing on both sides of that peak.

- **Wien's law**: it exactly describes this last concept; the spectral radiance of a black body will peak at different wavelengths, that are inversely proportional to the temperature:

$$\lambda_{max} = \frac{b}{T} \tag{2.4}$$

where $b = 2{,}8978 \cdot 10^{-3}\, mK$ is a constant of proportionality, while T is the absolute temperature.
Thus the wavelength and the temperature of the thermal radiation are inversely proportional to each other. In addition, starting from the spectral radiation emitted by a body, Wien's law makes it possible to obtain the temperature of the body itself.

- **Stefan-Boltzmann law**: it states that the total power emitted by a black body is directly proportional to the fourth power of the black body's temperature:

$$P = A\sigma T^4 \tag{2.5}$$

where A is the body surface area and $\sigma = 5{,}67 \cdot 10^{-8}\ W/(m^2K^4)$ is the Stefan-Boltzmann constant.

As already mentioned, the solar spectrum resembles the spectrum of a black body at 5780 K. By comparing them, we can notice that the area below the two curves in figure 2.3 is the same, even though the curves do not perfectly match, since the Sun is not exactly a black radiator and it does not show a single uniform temperature, as we have seen in the previous section.

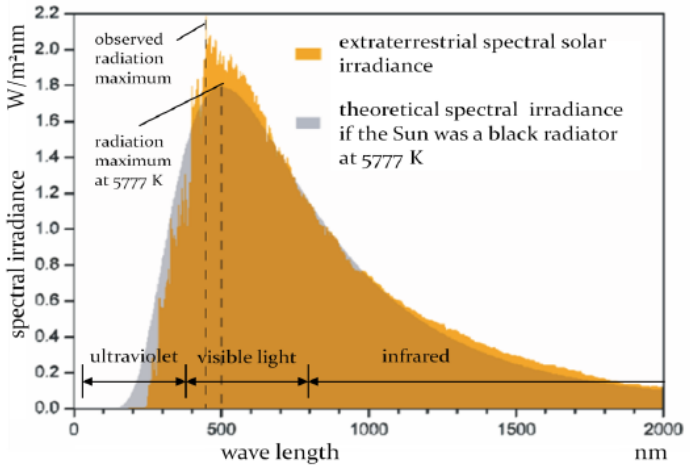

Figure 2.3: Comparison between solar spectrum and the spectrum of a black radiator at 5777 K[17]

The solar spectrum is primarly made up of the visible light (with a wavelength ranging from about 360 nm to 760 nm). Furthermore, solar radiation with a wavelength above 800 nm is called infrared radiation and features a lower energy than the one of the ultraviolet radiation (wavelength below 400 nm).

2.3 The Sun's impact on the Earth

The solar radiation that reaches the Earth's ground is the source of energy for the CSP plants we are interested in.
Firstly, let's analyze a remarkable parameter, that quantifies the solar radiant power outside the earth's atmosphere: the solar constant G_{sc}; it can be defined as the total radiation energy received from the Sun per unit of time per unit of area on a theoretical surface perpendicular to the Sun's rays and at Earth's mean distance from the Sun [18]. It depends on three factors: the temperature of the Sun (whose surface can be considered to be at 5777 K), the radius of the Sun (about $6{,}965 \cdot 10^8$ m) and the mean distance between the Sun and the Earth, r_{se}(approximately

$1{,}496 \cdot 10^{11}$ m).
The solar constant G_{sc} can be evaluated as the ratio between the total power of solar radiation (according to Stefan-Boltzmann law is given by $P_s = \sigma T^4 4\pi r$) and the area of a sphere with radius r_{se}:

$$G_{sc} = \frac{P_s}{4\pi r_{se}^2} = 1367 \quad \frac{W}{m^2} \tag{2.6}$$

Thus we can notice that G_{sc} represents the solar power acting on a surface on top of the Earth's atmosphere. Actually, the solar constant G_{sc} is not constant at all; the reason is due to the fact that the distance Sun-Earth is not steady itself and to the embraced hypothesis of the Sun as a black body. In particular, the mean Earth-Sun distance changes by $\pm 1{,}7\%$ during the year, causing a variation of the solar constant of about $\pm 3{,}3\%$ [19]
Nonetheless, the fixed value of G_{sc} equal to 1367 $\frac{W}{m^2}$ and established by the World Radiometric Center is the generally accepted one [20]
Moreover starting from the solar constant, it is possible to evaluate the solar power received by the Earth as follows:

$$P_{tot} = \pi r^2 G_{sc} = 1{,}74 \cdot 10^{17} \quad W \tag{2.7}$$

in which $r = 6371$ km is the mean Earth radius and taking into account one year (8760 h):

$$Q = P_{tot} \cdot 8760 = 1{,}52 \cdot 10^{18} \quad kWh \tag{2.8}$$

However, even though the amount of energy provided by the Sun (eq.2.8) is impressive, the solar radiation that reaches the Earth's ground is much lower, because of the *extinction processes* occurring in the atmosphere, that reduce the amount of solar radiation on the Earth's surface. These phenomena depend on conditions that are deeply mutable, such as humidity, aerosol concentration and the presence of clouds.
The extinction processes are made up of absorption and scattering, that are depicted as follows:

- **absorption**: in the atmosphere there are some elements that absorb the solar radiation; in particular, the infrared solar radiation is heavily absorbed by water vapour and carbon dioxide, ozone tends to absorb solar radiation with wavelengths below 290 nm, while oxygen and nitrogen absorb radiation over a wide range of wavelengths. Approximately 23% of incoming solar energy is absorbed by the atmosphere, while 48% is able to reach the Earth's surface and it is absorbed by it [21]

- **scattering**: it causes part of the direct solar radiation to turn into diffuse radiation, by means of certain particles, called *non-uniformities*. Depending on the size and shape of those non-uniformities, we may have **Rayleigh-scattering** or **Mie-scattering**. In the first case, the dimension of the particles causing scattering is much lower than the wavelength of the solar radiation, following a λ^{-4} law: this also explains the blue color of the sky: indeed, having the blue light a shorter wavelength, it is much more scattered with respect to light with longer wavelengths.
  As regards the Mie-scattering, the non-uniformities are mainly water droplets, ice crystals, aerosol particles, showing a diameter that is equal or higher than the radiation wavelength. In this case, the scattering has a weak dependance on the wavelength of the radiation, while it deeply varies according to paramenters such as air pollution and cloudiness. Thus, approximately 30% [21] of the incoming solar radiation is reflected back to space and it does not hit the Earth's surface.

Figure 2.4 shows that much of the radiation emitted by the Sun is attenuated by the previously listed phenomena; the portion that reaches the Earth's surface is mainly made up of visible, infrared light and a tiny amount of ultraviolet beams.

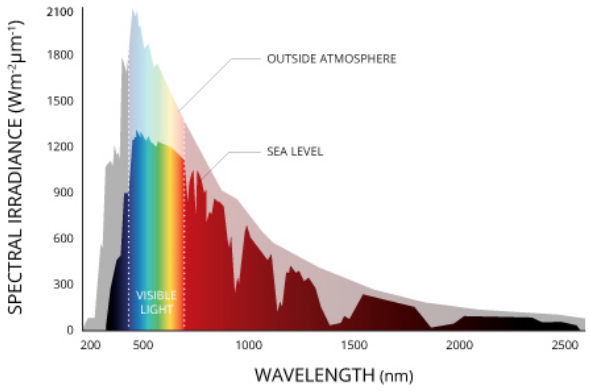

Figure 2.4: Solar radiation reaching the Earth's surface[22]

2.3.1 Global irradiance

Global irradiance corresponds to the quantity of power per unit area received from the Sun, over all wavelengths [23]. It is expressed in W/m^2. This parameter takes into account three contributions: the direct radiation, the reflected and the diffuse one. The only one that can be exploited by CSP systems is the direct share, the directionally fixed one, that has not experienced scattering in the atmosphere.

On the other hand, both the reflected and diffuse radiation have not a privileged direction and thus cannot be focused on CSP systems.
Hence the total irradiance is given by the sum:

$$G = G_B + G_D + G_R \tag{2.9}$$

where:

- G_B is the direct solar radiation
- G_D is the diffuse solar radiation, whose direction has changed over time due to scattering phenomena
- G_R is the reflected solar radiation, that depends on the ground reflectivity

Equation 2.9 can be rewritten considering the most general case of total irradiance on tilted planes, leading to eq. 5.1:

$$G = G_{bn} \cdot cos\theta + G_{dn} \cdot F_{sc} + G_{bt} \cdot \rho \cdot (1 - F_{sc}) \tag{2.10}$$

in particular:

- G_{bn} is the direct normal irradiance
- θ is the incident angle, the one between the direction of the beams and the normal of the plane
- G_{dn} is the diffuse irradiance, perpendicular to the horizontal plane
- F_{sc} is the view factor between the sky and the solar collector, defined as:

$$F_{sc} = \frac{1 + cos\beta}{2} \tag{2.11}$$

- G_{bt} is the irradiance of the direct solar radiation on a tilted plane
- ρ is the reflecticity of the Earth's surface (i.e. albedo)
- F_{cg} is the view factor between the ground and the solar collector, defined as:

$$F_{cg} = \frac{1 - cos\beta}{2} \tag{2.12}$$

- β is the tilt angle of the receiver's plane

In conclusion, knowing the direction of the beam radiation is essential for being able to concentrate the solar power.
The resolution of this parameter, that can be also seen as the apparent position of the Sun with respect to an observer on the Earth, depends on several elements, such as time, the geometry of the Sun and the Earth, the exact position of the observer.
To obtain the value of the beams direction, many different algorithms are available, including Michalsky and NREL ones [17].

2.4 Sun-Earth geometry

Taking into account a geocentric perspective, the Sun apparently rotates around the Earth in the equatorial plane (in case of spring or fall equinox) and in planes parallel to the latter one during all the other days.

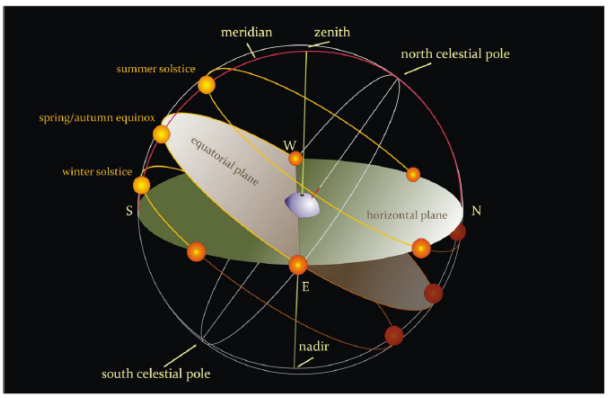

Figure 2.5: Geocentric point of view of Sun and Earth[17]

In particular, the equatorial plane is the one including the Earth's equator, that divides the planet in Northern and Southern hemisphere.
The other plane depicted in figure 2.5 is the one that contains the observer's horizontal line and is thus known as *horizontal plane*.
The intersection between these two planes forms an angle equal to $90°-\Phi$, in which Φ is the observer's latitude.

In order to define the position of the Sun with respect to an observer in the geocentric perspective, two angles are needed. Taking into consideration an equatorial coordinate system (fig. 2.6), the parameters involved are the declination δ and the hour angle ω.

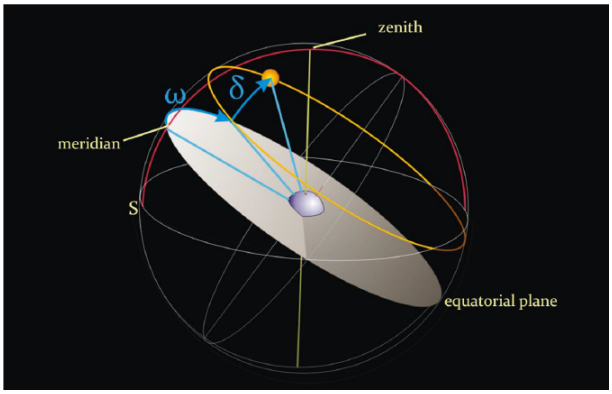

Figure 2.6: Declination and hour angle[17]

- The declination δ is the angle between the equatorial plane and a line connecting the observer to the Sun. It does not depend on the position of the observer but only on time. Among the many formulations available, the Cooper one is reported:

$$\delta = 23{,}45° \cdot sin\frac{360° \cdot (284 + DoY)}{365} \tag{2.13}$$

  in which DoY is the day of the year.
  Remembering that the Earth's axial tilt is approximately 23,45°, table 2.1 reports the values of δ according to four specific days of the year:

Table 2.1: Values of declination as function of DoY

δ	Day of the year
0°	spring equinox
0°	fall equinox
-23,45°	winter solstice
+23,45°	summer solstice

- The hour angle ω shows how much time has elapsed since the Sun passed the meridian of the observer's location. It depends on time and particularly it changes during the day. It is defined by equation 2.14 [17]:

$$\frac{\Delta\omega}{\Delta t} = \frac{15°}{h} \tag{2.14}$$

  At solar noon, $\omega = 0°$; in the morning it is expressed as negative degrees, while in the afternoon as positive ones.

In addition, Δt is not standard time [1] but solar time, under which the value of time depends on the Sun's location in the sky; it is a function of standard time and the longitude of the position considered.

In the horizontal reference system (fig.2.7) the two angles involved are:

- The solar altitude angle α_s:

$$sin\alpha_s = cos\Phi \cdot cos\delta \cdot cos\omega + sin\Phi \cdot sin\delta \tag{2.15}$$

in which Φ is the latitude of the observer's position.
α_s represents the Sun's angle with respect to the Earth's horizon; it can be replaced by the *zenith angle* Θ_z that is expressed as:

$$\Theta_z = 90^\circ - \alpha_s \tag{2.16}$$

and thus

$$cos\Theta_z = cos\Phi \cdot cos\delta \cdot cos\omega + sin\Phi \cdot sin\delta \tag{2.17}$$

Θ_z represents the angle formed by the Sun's beams with respect to the vertical.

- The solar azimuth γ_s that calculates the Sun's angle in an easterly direction with respect to the North

$$\gamma_s = sign(\omega) \left| cos^{-1} \frac{(sin\Phi \cdot cos\Theta_z - sin\delta)}{cos\Phi \cdot sin\Theta_z} \right| \tag{2.18}$$

in which the sign function:

$$\text{sign}(\omega) = \begin{cases} +1 & if \ \ \omega > 0 \\ \\ -1 & if \ \ \omega < 0 \end{cases}$$

It can be noted that α_s, Θ_z and γ_s vaty during the day.

[1] Standard time is the one in a specific time zone

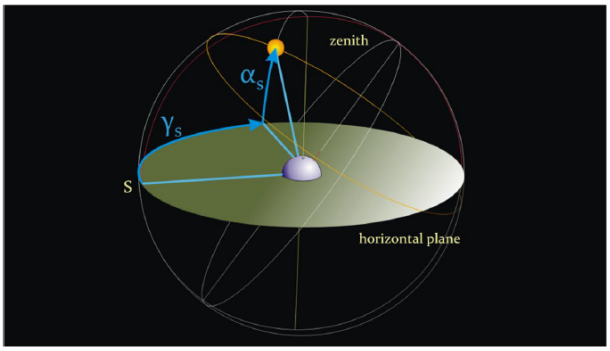

Figure 2.7: Horizontal reference system[17]

Chapter 3

Concentrated solar power (CSP) technology

Concentrated solar power (CSP) is a key technology for the production of clean energy, harnessing the plentiful solar source.
Sunlight is concentrated in CSP facilities and turned into high temperature heat for the direct or indirect running of electricity generators.
Particularly, CSP plants need the direct normal irradiation (DNI) [1] that, has shown in figure 3.1, is generally achievable in subtropical zones.

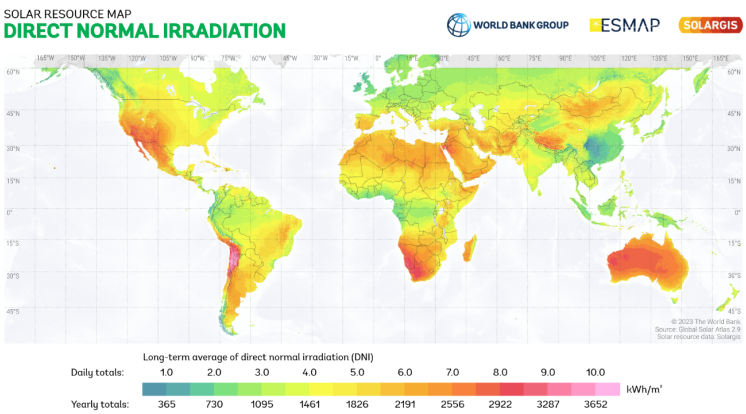

Figure 3.1: Direct Normal Irradiance[25]

A fascinating aspect is the possibility to couple this technology to thermal energy

[1] DNI represents the amount of energy received on a surface perpendicular to the Sun's rays, per unit surface [24]. It is also called *beam radiation*

storage (TES); in this case when the weather is cloudy and during the night, the thermal energy stored can ensure the production of electricity, without seeking for fossil resources. Hence the dispatchability and flexibility of CSP technology is enhanced.
Even though concentrated solar power systems are mainly employed for renewable electricity generation, they are making inroads into developing sectors, such as desalination, solar fuels and process heat [26].
In 2023 the installed capacity worldwide of this technology is 7,5 GW [27], with two leader countries: Spain (2,3 GW) and US (1,7 GW) [28].
As regards the costs, according to the International Energy Agency (IEA), as technologies get more advanced, the cost of CSP facilities is predicted to be cut in half by 2030, with respect to 2015 costs [29].
The installation sizes usually range from 30 to 200 MW; new CSP facilities costs currently account for $3500 \div 6000$ \$/kW, while in case of plants coupled with 6-hour thermal storage, the costs rise up to $6000 \div 9000$ \$/kW [28].

CSP systems harvest solar radiation and they concentrate it on a receiver, by means of reflective surfaces. The heat absorbed by the receiver is transferred to a fluid that in turn drives a standard power cycle (i.e. Rankine, Brayton, Stirling) to produce electricity.
The heat transfer fluid (HTF) circultaing in the receiver is heated up to 600-1200 °C, according to the selected kind of CSP facility.
The aim of this fluid is to accumulate thermal energy and to bring it to the power block, that usually uses a Rankine cycle to turn heat into electricity. In particular, two ways are possible:

- Indirect steam generation: the heat is transferred from the HTF to the Rankine cycle working fluid (water). The most used HTF are molten salts and synthetic oils, since they have to guarantee an elevated evaporating temperature and a low freezing point.

- Direct steam generation: the steam for the Rankine cycle is directly generated in the absorber tubes and transported to the turbine. There is only one fluid cycle, the steam one.

3.1 Types of CSP systems

CSP technology can be classified according to four different layouts: parabolic trough, linear Fresnel, solar tower and parabolic dish (fig.3.2).

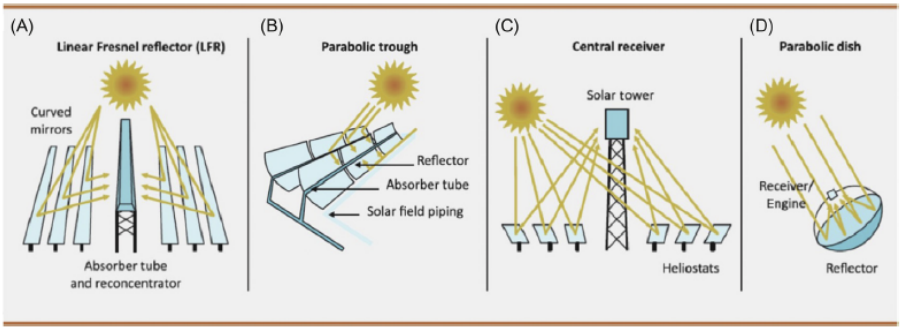

Figure 3.2: Four kinds of CSP configuration systems: (a)Linear Fresnel (b)Parabolic trough (c) Solar tower (d)Parabolic dish[28]

Following a more detailed analysis:

- **Parabolic trough collectors**: the direct solar radiation is focused onto a tubular receiver, that is placed along the parabolic channel's focal line.
  The majority of installed concentrated solar power technology is represented by parabolic trough facilities, providing over 90% of the entire capacity of CSP systems [30].
  The first commercial power plant in Europe using parabolic troughs is the 50 MW Andasol 1 solar power station, in Andalusia, Spain and it has been in operation since 2009 [31].
  Besides electricity generation, these systems can be used to provide process heat for industrial processes (e.g. chemical, food, textile ones).
  A tracking system is essential to let the mirrors follow the direction of sunlight.
  Almost all parabolic trough collectors adopt synthetic thermo oil as heat transfer fluid; it is an eutectic mixture with a maximum working temperature of 400 °C that has not to be exceeded, to avoid thermal cracking of the fluid [30].

Figure 3.3: Andasol 1 solar power plant, Andalusia, Spain[32]

- **Linear Fresnel collectors**: the direct solar radiation is focused onto a tubular receiver, by means of thin, flat mirror stripes, that are mechanically bent to acquire a little curvature. By splitting the lens into a series of concentric annular parts, Fresnel lens require less material and thus a lower thickness with respect to usual lens [33].
  Figure 3.5 depicts how Fresnel mirrors can approximate the optical features of a parabolic trough mirror, by means of linear sections that concentrate the incoming radiation onto a focal line [34].

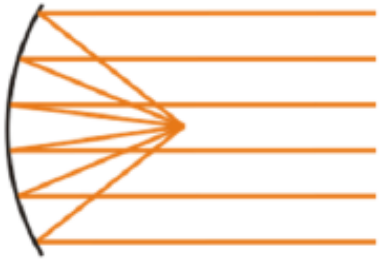

Figure 3.4: Parabolic trough mirror [34]

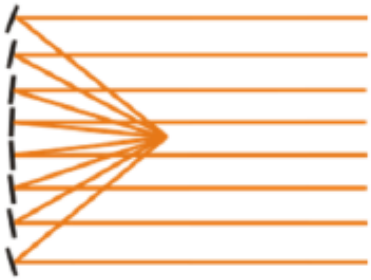

Figure 3.5: Fresnel mirror [34]

Linear Fresnel collectors guarantee lower costs, in terms of construction, installation and maintenance, compared to other CSP facilities. However their solar-to-electric efficiency is lower than parabolic trough collectors, mainly because of higher optical losses [34].
Novatec Solar constructed Europe's first commercial power plant, Puerto Errado 1 (PE 1) in Murcia, Spain, with an electrical output of 1,4 MW [34].

Figure 3.6: Puerto Errado 1 solar power station, Murcia, Spain[35]

The lack of experience with Fresnel power plants is a further drawback; being a less proven technology can result in a lower perceived reliability and higher efforts in finding economic investements [34].

- **Central tower system (or central receiver)**: the receiver is situated on the top of the solar tower and it absorbs the direct solar radiation from a multitude of sun-tracking mirrors; these latter ones are also called *heliostats* and they constitute a *solar field*. Approximately 50% of the investment costs are required by the heliostat field [36].
  This technology is mainly aimed at producing electricity, but is also making inroads into other applications, such as hydrogen production and desalination of seawater [36].
  When molten salts or thermo oils are employed as heat transfer fluids, the temperature reached in the receiver are in the range $600 \div 1200$ °C [28].
  The power block suitable for this technology are not only Rankine cycles, but also Brayton ones, thanks to the high temperatures available.
  These systems are able to produce electricity whether the Sun is shining or not, when coupled to thermal energy storage.

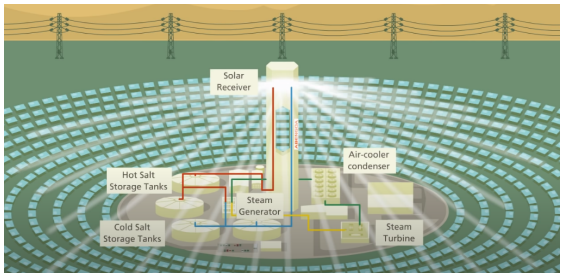

Figure 3.7: Solar power tower scheme[37]

Figure 3.8: PS20 and PS10 solar tower plants, Andalusia, Spain[38]

- **Parabolic dish collector**: a parabolic dish focuses the incoming solar radiation onto its focus, where the solar receiver is located.
  By means of a tracking control system, the dish is always pointed toward the Sun during the day.
  The heat absorbed by the receiver can be turned into electricity by using typically a Stirling engine or it can be exploited to perform thermochemical reactions. In the first case, th heat collected is turned into mechanical energy, by means of the heat engine (either Stirling engine or micro gas turbine) and eventually converted into electricity, by the generator [39].
  The installation sizes are typically between 5 and 25 kW and thus they are perfect for decentralized and off-grid applications [39]. Moreover, by grouping lots of solar dishes in arrays, this solution is suitable for large scale power plants [40].
  Since parabolic dish collector concentrates the solar radiation in one point, the concentration ratios achieved are very high thus resulting in elevated temperatures (above 800 °C) and the highest efficiency (30%) among all CSP technologies described [39]. *Hafez et al.* showed that this facility is plenty of benefits: elevated power density, high efficiency, resistance against moisture, but also an eye-catching modularity and flexibility [41].

Figure 3.9: Solar dish technology[42]

Table 3.1 illustrates the main features of the current concentrating solar power technologies: Parabolic Trough (PT), Linear Fresnel (LF), Central receiver (SR) and Parabolic Dish (PD).

Table 3.1: Characteristics of the four technologies[43]

Concentration method	Line conc. system		Point conc. system	
Solar field type	PT	LF	CR	PD
State of the art	commercial	pre-commercial	early projects	demo
Cost of solar field [€/m2]	200-250	150-200	250-300	>350
Typical unit size [MW]	5-200	1-200	10-100	0,010
Operating temperature [°C]	390	270-550	550-1000	800-900
Heat transfer fluid	synthetic oil, water	synthetic oli, water	air, molten salt, water	air
Thermodynamic power cycle	Rankine	Rankine	Rankine, Brayton	Stirling, Brayton

In conclusion, parabolic trough and linear Fresnel systems are referred to as *line-focus* facilities, since the sunlight is focused on a linear receiver; the latter one

usually consists of an evacuated glass layer over a steel pipe, to ensure thermal insulation.
On the other hand, solar tower and parabolic dish technologies ensure much higher values of concentration ratios, being the solar radiation focused in only one point (at least, ideally). Unfortunately, their tracking systems necessitate a greater degree of accuracy than line-focus plants [29].

3.2 Solar receiver

The solar receiver is the heart of the CSP technology: it collects the concentrated solar radiation and then it transmits it to a suitable heat transfer fluid, at remarkably high temperatures (600-1200 °C) [14].
In this thesis work, the interest is focused on a receiver that acts also as a reactor, for the realization of endothermic chemical reactions, in which the source of energy is guaranteed by the high temperature heat absorbed by the receiver itself. For this purpose, parabolic trough and linear Fresnel technologies are not suitable, due to the modest concentration ratios and temperatures (generally lower than 500 °C) [44]. Thus solar tower and parabolic dish are the leftover facilities for this application, ensuring much higher temperatures (up to 2300 K), able to drive thermochemical processes [14].
Broadly speaking, the solar receiver exploits cavities, black-painted walls, porous absorbers to mimic a blackbody's ability to capture solar power [45].
According to geometry, two design alternatives are available: *external receiver* and *cavity receiver*. The first receivers are typically characterized by a cylindrical shape and solar radiation hits them on the external surface. In the second case, a tiny aperture allows the direct solar radiation to enter the receiver. The cavity exhibits a blackbody behaviour as a result of the numerous reflections among its walls [14]. Thus, a balance between the amount of absorbed energy and the re-emitted one through the cavity is needed and can be accomplished by modulating the cavity dimension.
A further classification of solar receivers can be made, resulting in: *Directly Irradiated Receivers (DIR)* and *Indirectly Irradiated Receivers (IIR)*. The former ones employ fluids, particle streams that are directly subjected to the direct solar radiation. DIR are also known as *volumetric receivers*, because the concentrated solar radiation enters the receiver and permeates its whole volume [14].
On the other hand, in the latter ones the heat is transferred to the HTF through the absorbing walls of the receiver, that are exposed to the concentrated solar radiation [45]. An example is the tubular receiver with absorbing surfaces made up of a vast number of pipes, in which the heat transfer fluid is pumped upwards (fig.3.10).

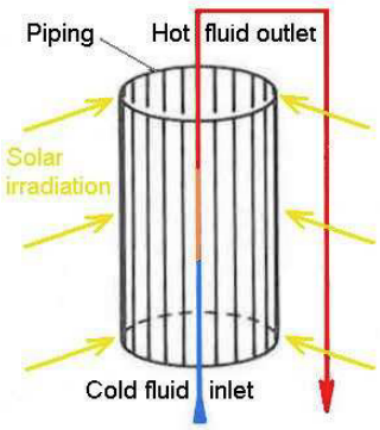

Figure 3.10: Indirectly irradiated tube receiver[36]

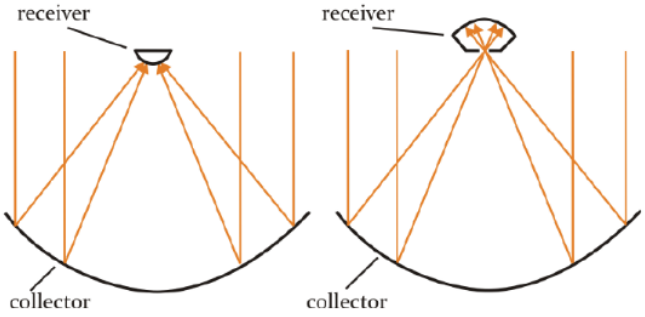

Figure 3.11: External (on the left) and cavity (on the right) receiver[39]

Being interest in high temperature applications, the cavity receiver is the most suitable one, ensuring also lower losses [39]. In particular, radiative heat losses are reduced because the majority of the radiation that is released stays inside the cavity and it is absorbed once more. Moreover, compared to external receivers, cavity ones are subjected to inferior convective heat losses too.

3.3 Efficiency of a CSP system and concentration ratio

The maximum efficiency of a CSP plant can be obtained by multiplying two efficiencies: the one of the receiver ($\eta_{receiver}$) and the one of the heat-to-electricity conversion ($\eta_{conversion}$) [46].

Receiver efficiency

$\eta_{receiver}$ is related to the conversion process of solar radiation into high temperature heat. Taking into account that the useful heat Q available at the receiver's level is given by the difference between the absorbed energy and the heat losses (both radiative and convective ones), according to eq.3.1 [46]:

$$Q = CG\tau\alpha A - \epsilon\sigma A(T^4 - T_{amb}^4) - hA(T - T_{amb}) \tag{3.1}$$

where:

- G is the solar irradiance
- τ is the receiver transmittance
- α is the absorptance of the receiver
- A is the area of the absorber [2]
- ϵ is the emissivity if the receiver
- σ is the Stefan-Boltzmann constant, equal to $5{,}67 \cdot 10^{-8} \quad \frac{W}{m^2K^4}$
- h is the convection coefficient
- T is the temperature of the absorber
- T_{amb} is the ambient temperature (i.e. 300 K)
- C is the *concentration ratio*. It is given by the ratio between the heat flux focused on the receiver and the radiant flux from the Sun. It can be approximated as the ratio between the concentrator aperture area and the receiver aperture area. In particular, the former one is the area that catches and reflects the Sun's heat flux; while the latter refers to the receiver's surface that faces the concentrated heat flux.

$$C = \frac{A_c}{A_r} \tag{3.2}$$

[2]The absorber is the part of the receiver in which sunlight is turned into heat [46]

Thus $\eta_{receiver}$ can be obtained by dividing the useful heat Q by the total solar energy input:

$$\eta_{receiver} = \frac{Q}{CGA} = \tau\alpha - \frac{\epsilon\sigma(T^4 - T_{amb}^4) + h(T - T_{amb})}{CG} \tag{3.3}$$

By neglecting the heat convective losses, the receiver efficiency becomes:

$$\eta_{receiver} = \tau\alpha - \frac{\epsilon\sigma(T^4 - T_{amb}^4)}{CG} \tag{3.4}$$

Moreover, assuming that the receiver behaves like a black body, $\alpha = \epsilon = \tau = 1$ and thus:

$$\eta_{receiver} = 1 - \frac{\sigma(T^4 - T_{amb}^4)}{CG} \tag{3.5}$$

Maximum efficiency of a CSP system

Assuming that the conversion efficiency ($\eta_{conversion}$) achieves its maximum ideal value, that is the Carnot efficiency(η_{Carnot}), then the maximum efficiency of the CSP system (η), is given by eq.3.6:

$$\eta = (1 - \frac{\sigma(T^4 - T_{amb}^4)}{CG})(1 - \frac{T_{amb}}{T}) \tag{3.6}$$

in which $\eta_{Carnot} = 1 - \frac{T_{amb}}{T}$

Table 3.2: Typical performances of the four CSP plants layouts [46]

	Annual efficiency (%)	Peak efficiency (%)	Conc.ratio
PT	14	25	80
Solar tower	16	22	1000
LF	13	18	30
PD	20	32	1500

Table 3.2 provides an overview of the performances of the four kinds of concentrated solar power facilities previously described, including information on the annual efficiency, peak efficiency and concentration ratio.
In particular, *peak efficiency* is the maximum instantaneous value of efficiency, usually attained at solar noon, whereas *annual efficiency* takes into account also the changes occurring during the day and the seasons [46].

Figure 3.12 depicts the trend of η against temperature, as function of various values of concentration ratios:

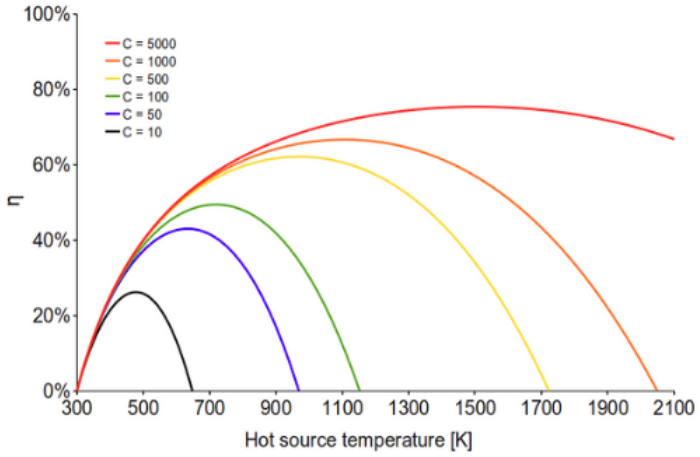

Figure 3.12: Efficiency of the overall CSP system [27]

Hence we can notice the importance of the concentration ratio: a useful parameter in optimizing the efficiency of a CSP facility. The higher C, the higher the amount of light concentrated on the collector; however this parameter cannot be increased without limitations. From a thermodynamic point of view, the existance of a maximum value of C is pretty clear: by continuously increasing the concentration ratio there will be a moment in which the temperature of the absorber is higher than the one of the Sun, from which the radiation is coming, breaking the 2^{nd} law of thermodynamics [46].

In particular, *Günther et al.* [17] evaluated the maximum values of concentration ratio for line concentration ($C_{max,linear}$) and point concentration ($C_{max,point}$) systems to be equal to:

$$C_{max,linear} = 215 \tag{3.7}$$

$$C_{max,point} = 46200 \tag{3.8}$$

Taking into account the temperature, fig.3.12 shows that each curve intersects the x-axis and thus the overall efficiency is equal to zero in two points: when the temperature of the absorber is equal to the ambient one and when T reaches its stagnation value (the receiver and the Sun are in thermal equilibrium).
Moreover, for a specific value of C, there is a theoretical temperature able to return a maximum value of efficiency.
It is interesting to follow the analysis of *Günther et al.* [17] to obtain the maximum temperature that the absorber can achieve, as function of the concentration ratio. Recalling that the total power emitted by the Sun (P_s) is directly proportional to the fourth power of its temperature (Stefan-Boltzmann law):

$$P_s = 4\pi r_s^2 \sigma T_s^4 \tag{3.9}$$

in which:

- r_s=695000 km, radius of the Sun
- T_s=temperature of the Sun $\approx$ 5780 K

and eq.2.6 that defines the solar constant G_{sc}, the solar power reaching the concentrator aperture area A_c is[3]:

$$\dot{Q}_c = A_c G_{sc} = A_c \cdot \frac{P_s}{4\pi r_{se}^2} = A_c \cdot \frac{4\pi r_s^2 \sigma T_s^4}{4\pi r_{se}^2} = A_c \sigma T_s^4 \frac{r_s^2}{r_{se}^2} \tag{3.10}$$

On the other hand, eq.3.11 refers to the radiant power emitted by the receiver (characterized by aperture area A_r and temperature T_r):

$$\dot{Q}_r = A_r \sigma T_r^4 \tag{3.11}$$

To obtain the maximum temperature achievable by the absorber, these last two radiant powers must balance each other:

$$\dot{Q}_c = \dot{Q}_r \tag{3.12}$$

hence:

$$A_c \sigma T_s^4 \frac{r_s^2}{r_{se}^2} = A_r \sigma T_r^4 \tag{3.13}$$

Taking into account eq.3.8 and eq.3.2 and by introducing a maximum value of concentration ratio:

$$\frac{1}{C_{max}} = \frac{r_s^2}{r_{se}^2} = \frac{1}{46200} \tag{3.14}$$

[3]Eq.3.10 is obtained under the assumption of not taking into account the extinction processes occurring in the atmosphere, described in section 2.3

we obtain:

$$T_r = T_s \cdot \left(\frac{C}{C_{max}}\right)^{1/4} = 5780K \cdot \left(\frac{C}{46200}\right)^{1/4} \tag{3.15}$$

The trend of eq.3.15 is illustrated in figure 3.13: as the concentration ratio increases, the absorber temperature rises too.

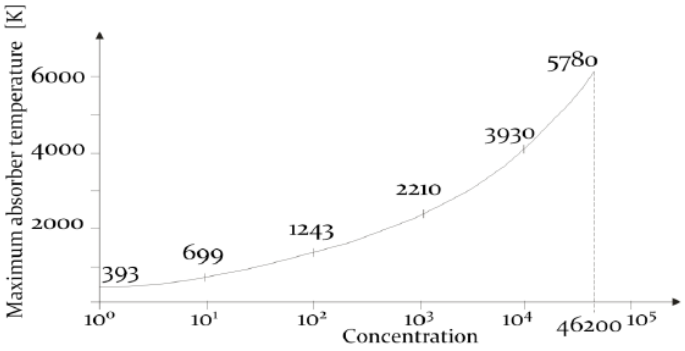

Figure 3.13: Maximum absorber's theoretical temperature as function of concentration ratio [17]

Nonetheless, this result is valid only in theory, due to the many approximations made; first of all, the assumption that the Sun and the absorber perfectly mimic a blackbody. Then the choice of disregarding the convective and conductive heat losses, that would have cause a further decrement of the reachable temperature by the absorber. At last, as already mentioned, the attenuation of the solar radiation due to the extinction processes has been neglected, ensuring a higher temperature of the receiver.
According to eq.3.15 and fig.3.13, the limit case of theoretical maximum temperature corresponds to $T_r = T_s = 5780$ K, by having $C = C_{max}$.

Another aspect that limits the concentration ratio is related to optical issues; the solar radiation does not reach the Earth's surface with parallel beams but rather it is spread in a conical way with an angle of 0,53°, called *solar beam angle* [17]. The result is the impossibility of focusing the incoming solar flux in one single point (instead, it is concentrated on an area around that point) and thus the concentration ratio is restricted to finite values.
In this case, the concentrator rim angle Ψ_{rim} determines the highest concentration ratio that can be reached. Figure 3.14 depicts the rim angle, that represents the largest angle between the center line of the collector and its edge.

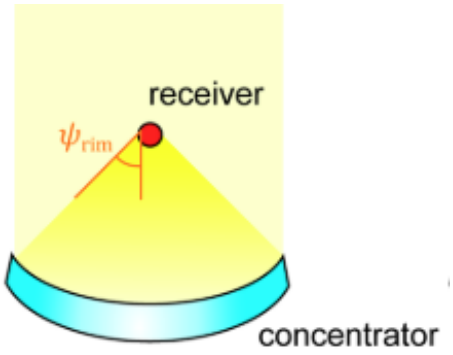

Figure 3.14: Rim angle Ψ_{rim} [46]

As a consequence, the maximum values of concentration ratios for line concentration and point concentration systems are reported below, taking into account the fact that the solar beams are not focused in one point, but within the Sun's image [17]:

$$C_{max,linear,opt} = \frac{1}{2} C_{max,linear} \approx 108 \tag{3.16}$$

$$C_{max,point,opt} = \frac{1}{4} C_{max,point} = 11550 \tag{3.17}$$

It can be noted that eq.3.16 and eq.3.17 are reasonable only in case of ideal mirrors and certain defined geometries. As regards real systems, the values of concentration ratios are [17]:

$$C_{real,linear} = 82 \tag{3.18}$$

$$C_{real,point} = 2000 \div 6000 \tag{3.19}$$

Indeed, actual CSP systems are affected by imperfections in their geometry: both microscopic and macroscopic defects present on the surface of mirrors as well as inaccuracy in the orientation of the collector, that further decrease the value of C. In addition, the analysis has been carried out under the hypothesis of mirrors with a reflection coefficient equal to one, that is far from the truth, due to material's flaws.

3.4 Further aspects on parabolic dish collector

As already mentioned in section 3.1, this kind of collector is able to concentrate on its focus only the direct solar radiation that is parallel to its axis, according to the properties of the paraboloidal configuration (see fig.3.15).

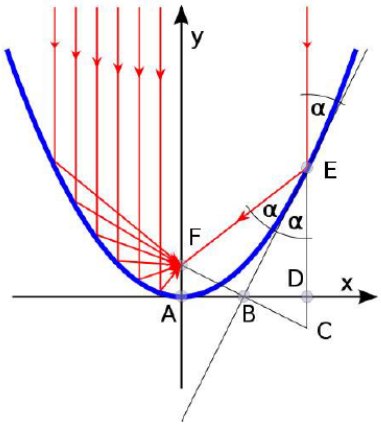

Figure 3.15: Path of Sun beams parallel to the parabola's axis[30]

Actually, the direct solar radiation ha a specific beam spread and hence it is focused on an area around the focal spot, characterized by a diameter given by eq.3.20 [41]:

$$d_{focal\,area} = \frac{f \cdot \Theta}{cos\Psi_{rim} \cdot (1 + cos\Psi_{rim})} \tag{3.20}$$

in particular, f is the *focal length*, that is the distance between the vertex and the focus [47] and can be expressed as function of the concentrator's diameter D_{conc}:

$$f = \frac{D_{conc}}{4 \cdot tan(\Psi_{rim}/2)} \tag{3.21}$$

While Ψ_{rim} is the rim angle, already defined in section 3.3. Moreover, as shown in figure 3.17, Ψ_{rim} may be used also to determine the curvature of the solar dish; in general, the smaller the rim angle, the flatter the parabolic concentrator.

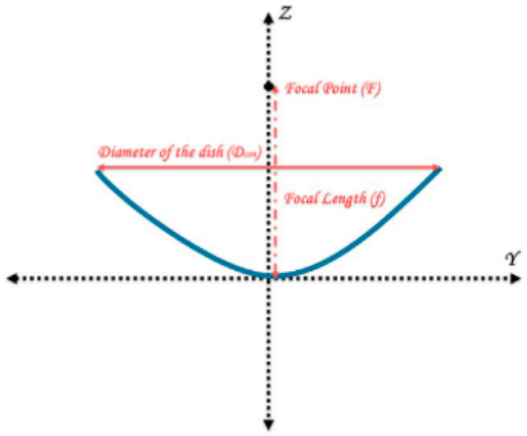

Figure 3.16: Focal length, focal point and diameter of the concentrator (D_{conc})[41]

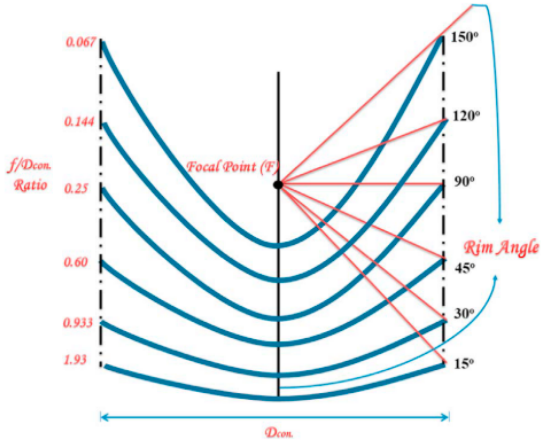

Figure 3.17: Different values of rim angle and focal length[41]

Chapter 4

Chemical looping

Chemical looping is a cycling technique that involves redox reactions to transport oxygen from the air to the fuel, by means of a solid metal oxide.
It is a highly flexible method that can be employed in a wide spectrum of processes such as emissions reduction, energy savings, electricity production and the generation of fuels and chemicals [48].
The interest in chemical looping is outstanding when considering the so called *heat pathway*: a formulation that depicts the collection in thermal form of the energy produced by RES and then exploited for the production of power or chemicals.
The main role in chemical looping technology is played by the so-called *oxygen carrier*, which is usually a metal oxide, that acts as an oxygen reservoir for oxygen donation and regeneration [49].
A classic chemical looping process involves two or more reduction and oxidation steps that create a *redox loop*. During the reduction, the oxygen carrier provides its lattice oxygen, under high temperature and low partial pressure environment. The two steps redox loop is closed when the lattice vacancy is refilled after the exposure of the oxygen carrier to an oxidant.
Moreover, chemical looping is an extremely versatile technology, characterized by high efficiency and the use of the oxygen carrier guarantees several advantages: in the first place, the redox reactions can be further broken down into other sub-steps. In the second place, the oxygen carrier not only acts as a reactant, but also as a mass separation agent, ensuring an *in situ* product separation: in other words, it prevents the mixing among the products of each sub-step.
Thus, being the split of the products the most energy intensive step in the chemical industry, this technology provides an important chance for energy conservation.

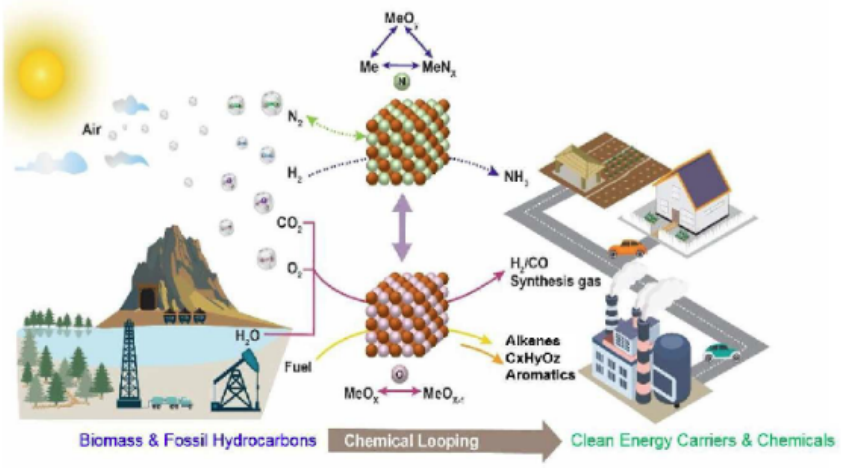

Figure 4.1: Schematic illustration of chemical looping potential applications[48]

In the following sections some applications of chemical looping are explored.

4.1 Chemical looping combustion (CLC)

CLC is a very fascinating technology for fossil fuel combustion, since it hinders the CO_2 dilution with the flue gases. This method requires two interconnected fluidized bed reactors (the air and the fuel reactor) and an oxygen carrier that circulates between them.

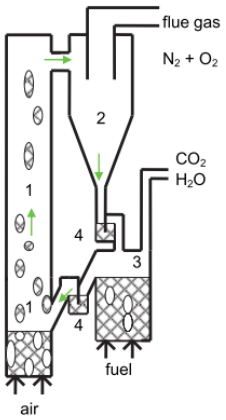

Figure 4.2: Fluidized bed reactor system. 1) air reactor 2) cyclone 3) fuel reactor 4) loop seals[50]

In the air reactor the oxygen carrier oxidation occurs according to the equation 4.1 [51]

$$4Me + 2O_2 \rightarrow 4MeO \tag{4.1}$$

In the fuel reactor the combustion of the fuel (e.g. methane) occurs according to the equation 4.2[51]

$$CH_4 + 4MeO \rightarrow CO_2 + 2H_2O + 4Me \tag{4.2}$$

Thus by considering the overall reaction, the conventional fuel combustion is obtained:

$$CH_4 + 2O_2 \rightarrow CO_2 + 2H_2O \tag{4.3}$$

The heat generated during the CLC process is equal to the heat of combustion, hence there are no enthalpy gains involved.
Picture 4.3 shows the CLC technology: after the oxidation from Me to MeO in the air reactor, the oxygen carrier is separated from the other products in a cyclone and then it is reduced back in the fuel reactor, providing oxygen for the combustion of the fuel.

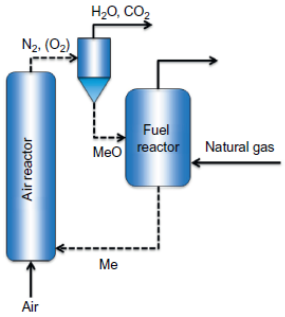

Figure 4.3: Schematic illustration of chemical looping combustion[51]

The products of the complete combustion in the fuel reactor are CO_2 and H_2O, that can be easily separated by condensing H_2O and thus avoiding the additional cost of a further CO_2 separation technology.
Another positive aspect is the reduction of the NO_x emissions, since the fuel combustion, occurring in the dedicated reactor, is characterized by the lack of air.

4.2 Chemical looping reforming (CLR)

CLR describes a series of chemical looping techniques in which a carbon-based fuel is reformed to syngas or pure hydrogen [51]. Indeed, the actual most used technology for H_2 production is *steam methane reforming (SMR)* that unfortunately

is a highly endothermic and energy intensive process. In particular, this method usually involves three steps: a high temperature catalytic reformer for syngas production, an intermediate temperature water gas shift (WGS) to increase the H_2 yield and decrease the concentration of CO; at last, a low temperature chemical or physical separation to get rid of CO_2 [52].
On the other hand, CLR offers the opportunity of producing syngas or hydrogen through *reforming or partial oxidation reactions*, following the same idea of CLC and starting from carbonaceous feedstock. Moreover, CLR guarantees that almost 100% of CO_2 can be captured, by merely separating the H_2O in the flue gases of the fuel reactor, without further costs [53].

4.2.1 Chemical Looping Steam Reforming

An interesting application of CLR is chemical looping steam reforming, in which three different reactors are involved, allowing the production of two distinct streams of H_2 and CO_2 [54]. Considering iron oxides as oxygen carriers, we can notice:

- **Fuel reactor**: in which Fe_2O_3 are reduced to FeO, while methane oxidizes to H_2O and CO_2, according to the deeply endothermic reaction:

$$12Fe_2O_3 + 3CH_4 \rightarrow 24FeO + 6H_2O + 3CO_2 \tag{4.4}$$

- **Steam reactor**: FeO oxidizes to Fe_3O_4. The H_2O introduced in the reactor guarantees the production of hydrogen, a totally decarbonized new fuel. In this step, the process is exothermic:

$$24FeO + 8H_2O \rightarrow 8Fe_3O_4 + 8H_2 \tag{4.5}$$

- **Air reactor**: the air introduced ensures the oxidation of Fe_3O_4 in Fe_2O_3, with a strongly exothermic reaction:

$$8Fe_3O_4 + 2O_2 \rightarrow 12Fe_2O_3 \tag{4.6}$$

The entire loop results to be exothermic and the overall reaction is:

$$3CH_4 + 2H_2O + 2O_2 \rightarrow 3CO_2 + 8H_2 \tag{4.7}$$

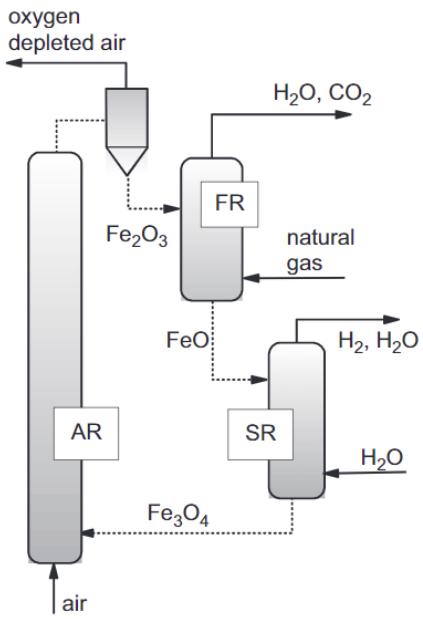

Figure 4.4: Schematic illustration of three-reactors chemical looping process for hydrogen production[54]

The process depicted is very appealing because it shows a further application of the chemical looping technology: the decarbonization of a fuel in three steps, with an overall efficiency of about 70% [55].

4.2.2 Chemical Looping Dry Reforming (CLDR)

CLDR represents a substitute to chemical loopoing steam reforming, since the role of the oxidant is now played by CO_2 instead of steam. Considering CH_4 as the starting carbonaceous fuel, the reactions involved in the loop are:

$$4Me + 4CO_2 \rightarrow 4MeO + 4CO \tag{4.8}$$

$$4MeO + CH_4 \rightarrow 4Me + CO_2 + 2H_2O \tag{4.9}$$

and the overall reaction can be written as:

$$CH_4 + 3CO_2 \rightarrow 4CO + 2H_2O \tag{4.10}$$

This last equation recalls the conventional *dry reforming of methane* [51], with the difference that chemical looping dry reforming aims at maximizing the CO production, instead of the syngas one. Hence, this technique points out a path in

which the exploitation of CO_2 ensures the generation of the much more flexible carbon monoxide.

4.2.3 Chemical Looping Partial Oxidation (CLPO)

CLPO longs for realizing an incomplete oxidation of the fuel and can be obtained by alterating the internal circulation rates and the oxygen carriers employed in the chemical looping combustion [51]. Unfortunately, besides the partial oxidation of the fuel, several further reactions occur, depending on the time, the temperature and the place considered within the reactor. In particular, at the beginning, when there is plenty of oxygen availability, the complete combustion of the fuel (e.g. methane) is favoured:

$$CH_4 + 4Me_xO_y \rightarrow CO_2 + 2H_2O + 4Me_xO_{y-1} \tag{4.11}$$

and only after some time the partial oxidation begins, according to 4.12

$$CH_4 + Me_xO_y \rightarrow CO + 2H_2 + Me_xO_{y-1} \tag{4.12}$$

However, another cascade of reactions follows the previous ones, such as:

- **Carbon deposition**:
$$CH_4 \rightarrow C + 2H_2 \tag{4.13}$$
- **Carbon gasification**:
$$C + H_2O \rightarrow CO + H_2 \tag{4.14}$$
- **Boudouard reaction**:
$$C + CO_2 \rightarrow 2CO \tag{4.15}$$
- **Steam reforming 4.16 or alternatively dry reforming 4.17**:
$$CH_4 + H_2O \rightarrow CO + 3H_2 \tag{4.16}$$
$$CH_4 + CO_2 \rightarrow 2CO + 2H_2 \tag{4.17}$$
- **Water gas shift**:
$$CO + H_2O \rightarrow CO_2 + H_2 \tag{4.18}$$

As a consequence, besides the aimed syngas production, there are also some undesired effects: carbon deposition, generation of CO_2, H_2O and the presence of unreacted fuel, that require further separation techniques or, in other words, extra costs and lower overall efficiency [51].

4.3 Chemical Looping Air Separation (CLAS)

CLAS represents a promising way for the production of oxygen: the second-highest volume industrial gas produced worldwide [56]. Pure oxygen is essential for one of the most used carbon capture techniques, that is *oxyfuel combustion* and *cryogenic air separation* is presently employed for this latter target. Thus, chemical looping air separation depicts an alternative to the conventional methods and oxygen decoupling is achieved by the well-known two steps redox reactions:

$$Me_xO_y \rightarrow Me_xO_{y-2} + O_2 \tag{4.19}$$

$$Me_xO_{y-2} + O_2 \rightarrow Me_xO_y \tag{4.20}$$

Two types of reactors can be used for this technique: the fluidised bed reactor and the packed bed one.
In the first case, the presence of two interconnected beds causes the reduction to occur in one bed and the oxidation in the other one, hence they are spatially separated. This kind of reactor guarantees a better control of the temperature and of the heat exchanged but also higher costs due to the transport of the oxygen carrier between the reactors [57].
On the other hand, in the packed bed reactor there is just a temporal separation of the reactions, ensured by regularly switching the input gas between reducing and oxidising conditions.
The operation at high temperatures enables the reutilization of heat from the air separation process in two ways: as a component of the CLAS process itself or as heat to feed an external power cycle [57].
Being a technique that requires a low energy demand, CLAS is quite efficient [58] and it represents a valid substitute to the pretty complex and expensive cryogenic distillation that, on the other hand, is feasible only for large-scale applications [59].
The most suitable oxygen carriers for CLAS are the Cu-based, Mn-based and Co-based ones [59]. At last, the oxygen produced can be used as mentioned before to feed oxyfuel combustion or it can be compressed and stored for other purposes.

4.4 Dissociation of CO_2 and H_2O through chemical looping

As already mentioned when combined with renewable energy, chemical looping technology is a sustainable method that can be adopted in order to produce energy, fuels, chemicals. A fascinating application of chemical looping is related to the dissociation of CO_2 and H_2O by means of concentrated solar power, with the goal of producing *syngas*: a mixture of CO and H_2. Thus, starting from the

high temperature heat provided by concentrated solar powers systems, syngas is obtained by means of the two well-known steps of CL technology, characterized by two different temperature levels:

- **High temperature step (or thermal reduction)**
- **Low temperature step (or thermal oxidation)**

In the first phase, high temperature heat is used to perform a reduction on a metal oxide, according to 4.21:

$$MeO_x + O_2 \rightarrow MeO_{x-\delta} + \frac{\delta}{2}O_2 \tag{4.21}$$

In the second step, the metal oxide is oxidised back to its original form, taking the necessary oxygen from very stable molecules entering the loop: H_2O (4.22) or CO_2 (4.23)

$$MeO_{x-\delta} + \delta H_2O \rightarrow MeO_x + \delta H_2 \tag{4.22}$$

$$MeO_{x-\delta} + \delta CO_2 \rightarrow MeO_x + \delta CO \tag{4.23}$$

Hence, during the oxidation phase, the splitting of H_2O in H_2 or the one of CO_2 in CO takes place. This process usually requires two interconnected reactors, with metal oxides circulating within them.
The temperature at which the redox loop occurs strongly depends on the oxygen carrier selected; in general the reduction phase requires a temperature between 1200 and 2400 K, depending on the mechanism of the reaction, while the oxidation of the metal oxides occurs at a temperature between 1000 and 1300 K [60]. Thus, since the reduction reaction asks for much higher temperatures than the oxidation one, a solution could be the adoption of a reducing agent (e.g. methane), that enhances the reduction process and decreases the temperature needed during it.

In this thesis, we are going to couple these thermochemical processes with the heat collected by a receiver, belonging to a concentrated solar power system. In particular, the solar beams are reflected by the parabolic dish and focuse on the cylindrical receiver, that quickly heats up, making the redox loop happen.

4.5 Oxygen carriers

Oxygen carriers are the heart of thermochemical processes: they turn raw materials into the desired products, circulating between two or more reactors [52].
The main features that these materials have to achieve are: [61]

- Adequate oxygen transport capability
- High reactivity for reduction and oxidation reactions, even after many redox cycles
- Negligible carbon deposition, that would release CO_2, lowering the CO_2 capture efficiency
- Cost effectiveness
- Environmental sustainability

Account must be taken of the fact that the main point of oxygen carriers in thermochemical cycles is not the production of materials with certain features (e.g. elevated porosity, high surface area) but rather that these characteristics are preserved in conditions of very high temperatures and recurrent thermal cycling [14].
Usually the most used oxygen carriers are *metal oxides*, such as nickel, iron and cerium-based ones, characterized by several oxidation states; they can be divided in two families, depending on their behaviour during the thermal reduction:

- *Volatile oxygen carriers*
- *Non-volatile oxygen carriers*

4.5.1 Volatile oxygen carriers

During the thermal reduction these materials experience a phase change from solid to gas, since their evaporation point is lower than the temperature of the heat provided.
A positive aspect of volatile oxygen carriers is that their transition to other oxidation states is stoichiometric; it means that the oxide is completely reduced, ensuring a much higher oxygen exchange ability and specific energy storage, with respect to non-volatile oxygen carriers [62]. Typical examples of these materials are ZnO and SnO_2.
However, volatile oxygen carriers require very high temperatures during the reduction and thus also high quality materials for the concentrators and the receivers, able to withstand such high temperatures. In addition, it is necessary to fastly separate the metal oxide from the oxygen after the thermal reduction, due to the high risk of recombination.
Taking into account the ZnO/Zn thermochemical process, the reduction step occurs at temperatures higher than 2000 °C [55] and its boiling point is at 1180 K [14].
In case of SnO_2/SnO cycle, the temperatures involved are: 1873 K for the reduction

of SnO_2 into SnO, evaporation point at 1800 K, while the exothermic oxidation occurs at 873 K [14].
These types of oxygen carrier have been employed for the production of syngas, hydrogen and also for biomass gasification [63].

4.5.2 Non-volatile oxygen carriers

The metal oxides belonging to this family remain solid during the thermal reduction, but the reaction is no longer stoichiometric:

$$MeO_x + hightemperatureheat \rightarrow MeO_{x-\delta} + \frac{\delta}{2}O_2 \tag{4.24}$$

where:

- x is the number of original oxygen atoms
- δ is the number of oxygen atoms removed; it increases as temperature rises, enhancing the reduction of the oxide

An advantage of these materials is the relatively low temperature requested for the thermal reduction (1200 - 1500 °C) moreover, being at the solid state, they are easy to manage and the recombination issue that affected the other group of metal oxides, now disappears.
With respect to volatile oxygen carriers, non-volatile ones are characterized by higher activity at low temperature and a faster kinetic [62]. Thus, the choice between these two families strongly depends on a compromise, considering the benefits and disadvantages of both of them.
The most used non-volatile oxygen carriers are the Ni, Fe, Cu, Mn and Co-based ones.
In figure 4.5 these materials are compared in terms of oxygen transport capacity, that expresses the amount of oxygen available during one redox cycle, while in picture 4.6 other characteristics are shown[64]:

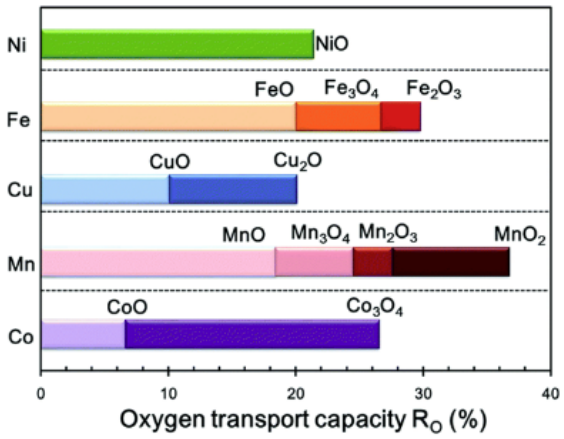

Figure 4.5: Oxygen transport capacity of different metal oxides[64]

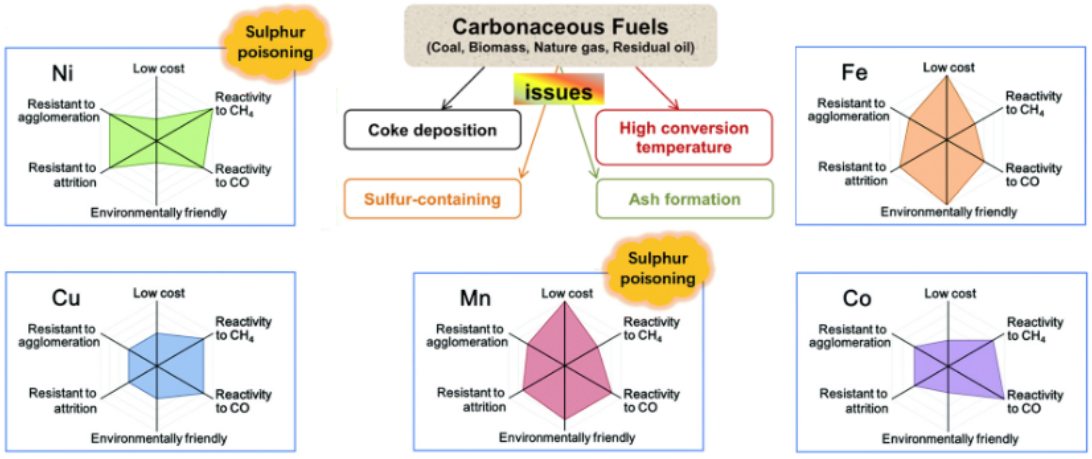

Figure 4.6: Other features of different metal oxides[64]

The use of fossil fuels and biomass to feed the chemical looping process provides negative aspects, such as sulfur poisoning and coke deposition, that leads to the deactivation of the oxygen carrier, especially in case of Ni and Mn-based oxides.

Iron oxides

Iron oxides are one of the most common oxygen carriers, characterized by large availability, low cost and high mechanical strength. The manufacturing cost of Fe-based oxides is much lower than the one of other transition metals (like Co, Ni,

Cu, Mn) because of its high abundance and the already well-developed production technologies [65].
In chemical looping, three different species of iron are involved:

- **Wustite** FeO in which Fe has the lowest oxidation state: Fe^{2+}
- **Magnetite** Fe_3O_4 in which Fe has an intermediate oxidation state: $Fe^{2,6+}$
- **Hematite** Fe_2O_3 in which Fe has the highest oxidation state: Fe^{3+}

Unfortunately, because of the very high temperatures required for the thermal reduction (higher than 1300 °C), iron oxides are subjected to sintering during cycling and their consequent deactivation [62]. Indeed, during sintering, the size of the oxygen carrier particles increases, negatively affecting the lattice oxygen transport rate and causing the unwanted carbon deposition phenomenon [52].
A solution to increase the activity of these materials and their resistance to sintering is the inclusion of *promoters*. For instance, Fe-Ni, Fe-Co and Fe-Cu converted respectively 92%, 83% and 85% of methane in CLR at 900°C, in contrast to Fe-based materials that showed only 84% of methane conversion [66].
Promoters such as Ni and Cu can be employed also to increase the reactivity of iron oxides at relatively lower temperatures. An example of application is when methane is adopted as reducing agent: the temperature required for the thermal reduction decreases to about 1023K [53].
Other promoter materials investigated in literature are: Al_2O_3, MgO, TiO_2, SiO_2, $MgAl_2O_4$, CaO, ZrO_2, CeO_2 [64]. Nonetheless, during the redox reactions, new phases tend to form, such as $AlFe_2O_4$, $MgFe_2O_4$, $FeTiO_3$, Fe_2SiO_4, $CeFeO_3$. Even though they still ensure a protection against sintering, they are also responsible for a deep decrease of the oxygen storage capacity, beacause of the tougher reducing and oxidising conditions now requested for the regeneration of the oxygen carrier [64].
A very promising support is CeO_2, characterized by high reactivity with methane and no carbon deposition. An easy and reversible release of lattice oxygen is guaranteed by the redox couple Ce^{4+} and Ce^{3+} [67]. As a result, the interaction between CeO_2 and Fe_2O_3 improves the reducibility of Fe_2O_3, when this kind of promoter is used [64].

Chapter 5

Experimental test

5.1 Thermogravimetric analysis (TGA)

TGA is a technique that evaluates a sample's weight change over time and at a specific temperature.
The analysis gives information on both chemical and physical events, such as chemisorption, solid-gas reactions (e.g. redox ones), phase change, absorption and adsorption [68]
There are three different kinds of TGA:

- **Static TGA**: while measuring the sample mass, temperature is kept constant
- **Dynamic TGA**: while measuring the sample mass, temperature changes in time
- **Quasistatic TGA**: the sample is heated at various temperature levels and kept at each interval for a certain time, until the mass stabilizes.

Moreover, TGA allows the evaluation of the thermal stability of a compound, by measuring the weight loss of the sample but it does not give information about the species released during the test. In that case, a mass spectrometer has to be coupled to the thermobalance.
The instrument used in the experimental test is the *STA 2500 Regulus*, manufactured by NETZSCH.

Figure 5.1: STA 2500 Regulus [69]

The device is made up of a thermobalance with a sample pan placed in a furnace and a thermocouple that measures the temperature.
In particular, the principal elements included in the thermogravimetric analyzer are listed below:

- **Thermobalance**: it tracks the sample's weight change. Figure 5.2 shows a schematic illustration of the thermobalance incorporated in STA 2500 Regulus. The monitoring system uses photodiodes to continuously check the position of the two arms of the balance; an arm contains the sample and is kept in the furnace, while the other one holds a reference empty crucible.

- **Furnace**: it has to be made of specific materials, able to withstand very high temperatures. Usually refractory materials are adopted for this purpose, such as Al_2O_3 ($T_{melting} > 2000$ °C).

- **Crucibles**: they are used to hold the sample and counterweight it. They are made of inert materials, in our case of Al_2O_3.

- **Temperature control system**: it includes thermocouples (type S) installed inside the furnace, close to the sample, that keep on measuring the temperature for the entire duration of the test.

- **Purge gas system**: it ensures a controlled atmosphere inside the furnace and

the removal of unwanted gaseous species released during the decomposition of the sample.

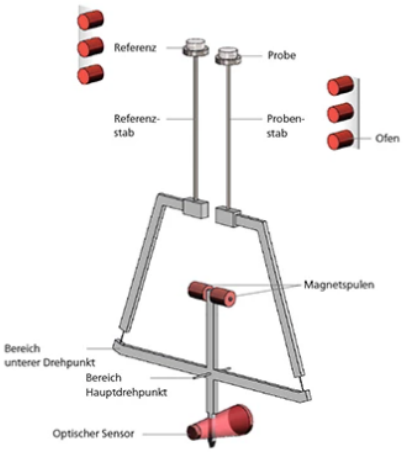

Figure 5.2: Schematic illustration of the thermobalance inside the STA 2500 Regulus [69]

During the test a *heating ramp* is performed: the sample is heated at a specific rate, starting from room temperature. The equipment measures both the weight and the temperature several times per second and then it records the variations of weight and the rate of weight changes.
Moreover, the atmosphere inside the furnace is controlled and the analysis may be performed under multiple conditions: inert gas, vacuum, oxidizing or reducing gases, etc.
The technical specifications of the instrument adopted are reported in table 5.1:

Table 5.1: STA 2500 Regulus datasheet[69]

STA 2500 Regulus	
Furnace data	
Max sample temperature	1600 °C
Heating rate	0,001 to 100 K/min
Temperature precision	0,3 K
Balance and sensor data	
Weighting range	±250 mg
Max sample load	1 g
Thermogravimetric resolution	0,03 μg
Thermocouple	Type S
Atmosphere	
Gas atmospheres	inert, oxidizing, vacuum

The crucible adopted is made of alumina, an inert material, with a purity of 99,7%. The pan is a cylinder with a 5,2 mm diameter and a height of 2,6 mm [69]. In this thesis we are interesting in performing a static TGA thus, the result of the analysis will be depicted on the *thermogram*, in which the sample mass is plotted against time, at a given temperature.

5.2 Experimental section

TGA is performed on commercial hematite (Fe_2O_3) particles, available at the Environmental Park laboratory, in Turin; unfortunately its specific composition is not known. Specifically, the alumina crucible is filled with 40 mg of Fe_2O_3 powder, previously weighted by means of a precision balance.
The test begins with the injection of 80 ml/min of Argon at ambient temperature, for 5 minutes. Then the heating ramp starts: temperature rises from the initial value (20 °C) up to 820 °C, with a heating rate of 20 K/min, keeping the supply of Argon (80 ml/min).
The redox reactions are performed at the constant temperature of 820 °C and are repeated for 20 cycles. Each cycle is made up of a redution, a stabilization and an oxidation step. In particular, the reduction phase is characterized by the injection of a mixture: 3 ml/min of CH_4 and 77 ml/min of Ar, for a total volume flow rate of 80 ml/min and it lasts 30 minutes.
The following oxidation step involves a mixture of 16 ml/min of CO_2 and 64 ml/min of Ar and it lasts 30 minutes too.
Between the reduction and the oxidation of hematite, there is the injection of pure

Argon for 5 minutes, in order to guarantee the stabilization of the process and the removal of unwanted species. In addition, the Argon flow rate acts also as a protective agent, requested by the instrument itself.
The temperature of 820 °C for the two steps of the redox reactions has been chosen according to *Monazam et al.* [70]; indeed, figure 5.3 shows that, within a certain time, higher the temperature, higher the reduction efficiency (considering a temperature range of 750 - 825 °C). In particular, the trend corresponding to $T = 825$ °C is much better than the other two proposed.

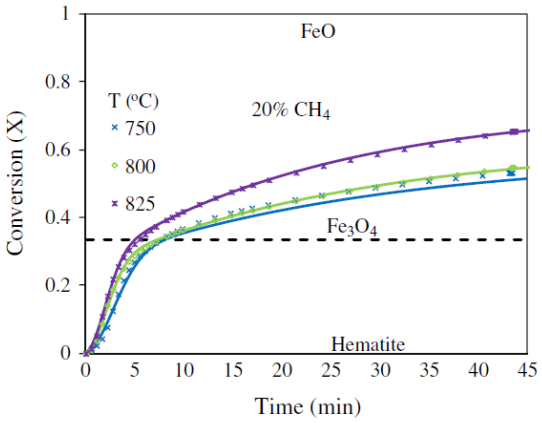

Figure 5.3: Effect of temperature on hematite conversion [70]

The process followed in the experiment is repeated 20 times and it is summarized in table 5.2

Table 5.2: Steps of the experimental test

Step	Temperature [°C]	Duration or slope	Gas injected
1	20	5 min	Ar
2	20 - 820	20 K/min	Ar
3	820	30 min	$CH_4 + Ar$
4	820	5 min	Ar
5	820	30 min	$CO_2 + Ar$
...	...	...	...
...	...	...	...
...	...	...	...
63	820	30 min	$CH_4 + Ar$
64	820	5 min	Ar
65	820	30 min	$CO_2 + Ar$
66	820 - 20	-20 K/min	Ar

Hence, we can notice that CH_4 is the reducing agent adopted to enhance the reduction reactions, while CO_2 is the stable molecule chosen to oxidize back the iron oxide.
The entire test lasts 24 hours and 50 minutes and the analysis on the data retrieved from the experiment is illustrated in figure 5.4

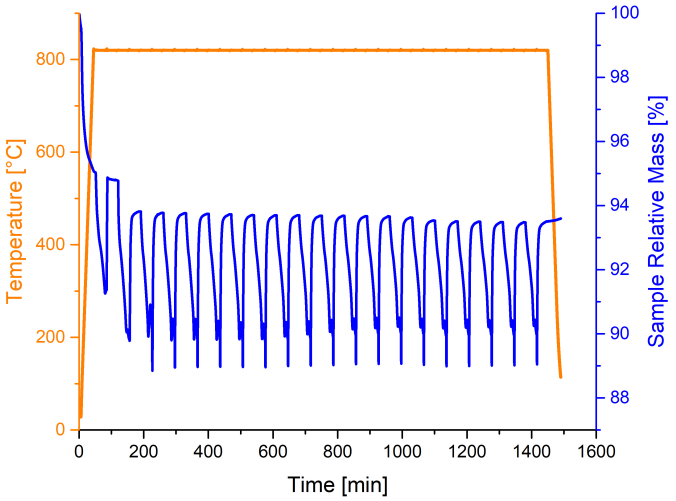

Figure 5.4: Sample relative mass and temperature measurement

This last diagram (5.4) represents the sample relative mass variation during reduction and oxidation for 20 cyclic tests, at 820 °C.
Mass fluctuations generally correspond to chemical reactions (e.g. redox ones), with a few exceptions; indeed, drying is a typical example: it causes a severe drop of the sample mass when the heating ramp starts. Indeed, as soon as the temperature reaches 820 °C, the relative mass of hematite abruptly falls from 100% to about 95% of the initial value. Thus, in picture 5.5 a zoom of the previous plot is reported, putting aside the first 4 cycles, in which Fe_2O_3 powder mass is not yet stabilized and undergoes phenomena like evaporation of some chemical impurities belonging to the sample itself.

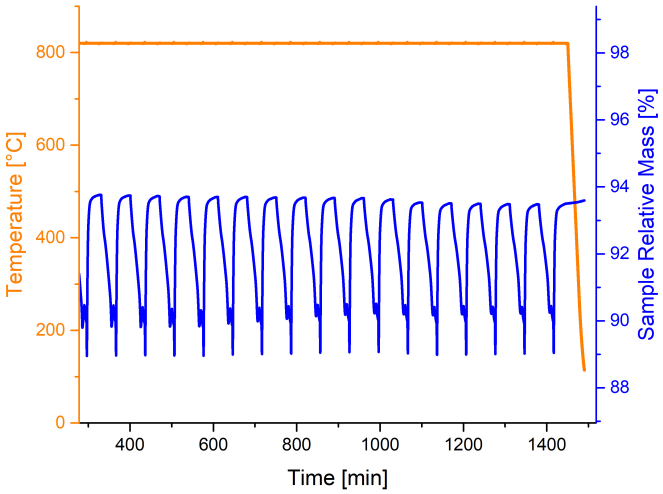

Figure 5.5: Zoom of the last 16 cycles

Now a comparison with a similar experimental test found in literature can be made. *Monazam et al.* [70] performed 10 redox cycles at 825 °C on 60 mg of hematite, using 20% CH_4 in N_2 during the reduction and zero-grade air during the oxidation. The total flow rate employed in each step is 45 sccm. The oxidation time is equal to the one of this work thesis, while reduction lasts longer: 45 minutes. Figure 5.6 shows the result of the analysis

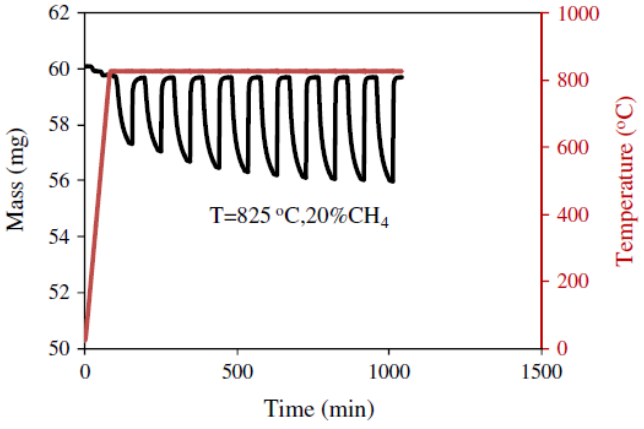

Figure 5.6: Mass and temperature measurement from Monazam [[70]]

Firstly, we can underline the different conditions under which the two tests are

carried out; the percentage of CH_4 used by *Monazam et al.* is much higher than the one chosen in Environmental park laboratory, indeed, in this last case it was possible to use only 3,7% of CH_4 in Ar, in order to comply with the flammability limits. Also the starting sample mass is different: 60 mg in the reference work and 40 mg in the present one. As regards the purge gas flow rate, a higher value is adopted in the current experiment and this could lead to a higher reduction efficiency, ensuring a more favourable lower oxygen partial pressure.
But, at a first glance, the comparison between picture 5.4 and 5.6 highlights a remarkable difference in the trend of the sample mass variation; while the oxidation steps are quite similar, the reduction ones widely differ. Indeed, the reduction curves of the present work show two *inflection points*, in which they change their slope.

This last aspect can be further investigated in picture 5.7; in this case besides the sample's remaining original weight, also the flow rates of CH_4 and CO_2 injected are plotted. Between the green and pink curves, the intake of pure Argon takes place. By focusing on the reduction phases, they are triggered by the introduction of the reducing agent (CH_4) and then they change their slopes on the graph twice (while in the reference work, this phenomenon occurs only once and with smaller evidence).

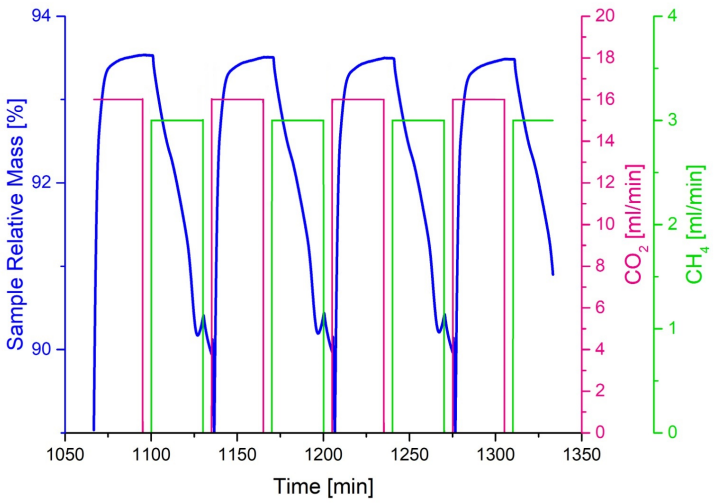

Figure 5.7: Sample mass and gas purge measurement

In particular, the first inflection point occurs 9 minutes after the beginning of each reduction step, causing a decrement of the process speed. On the other hand, the second change of slope, that induces a rise in the velocity, takes place 14 minutes after the initiation of the reduction.
Another peculiar behaviour happens 11 minutes before the end of the reductions: a slight increase of the sample mass; it could be explained by the carbon deposition that usually occurs during these reactions. The immediately after introduction of pure Ar ensures the recovery of the usual trend.
At last, a signal drop can be noticed every time the CO_2 purge is switched on, most likely witnessing that such behaviour is not characteristic of the redox reaction; indeed this event does not find feedback in *Monazam et al.* analysis. As depicted in figure 5.7, it causes the sample's remaining weight to be about 89% of the initial amount.

5.3 Reduction reactivity

As noted earlier, it is possible to put aside the first 4 cycles of the experiment, due to the lack of a regular variation of the sample mass and thus take into account the behaviour illustrated in figure 5.5.
As a consequence, we need to get rid of the starting sample mass used in the test (i.e. 40 mg of Fe_2O_3) and replace it with an *apparent mass* corresponding to the utterly oxidized sample mass of the first cycle represented in figure 5.5. Specifically, the apparent mass is about 93,7% of the initial 40mg, hence equal to 38,8 mg of Fe_2O_3.
Since there was not the chance to couple the TGA device to a gas chromatograph in order to analyze the gases emitted during the reactions, it can be now assumed that, according to the overall reaction of hematite to FeO reported by *Monazam et al.* [70], after 30 minutes of reduction, the gases released are the ones reporte in table 5.3

Table 5.3: Gas emitted during the reduction

CO	0,756 mg
CO_2	1,58 mg
H_2	0,144 mg

Nonetheless, this is just a rough approximation of the products obtained during the reduction steps and a more detailed computational analysis of the kinetic models and the variation of the gas emitted in time will be addressed in the following chapter.

The degree of conversion for reduction (or reduction reactivity) can be expressed as [64]:

$$x = \frac{M_{ox} - M(t)}{M_{ox} - M_{red}} \tag{5.1}$$

in which:

- M_{ox} is the weight of the sample in its oxidation state
- M_{red} is the weight of the sample in its reduction state
- $M(t)$ is the instantaneous weight of the sample, while exposed to CH_4

Thus, in this study M_{ox} is considered equal to the previously defined apparent mass of 38,8 mg. The result of the application of equation 5.1 is depicted in figure 5.8

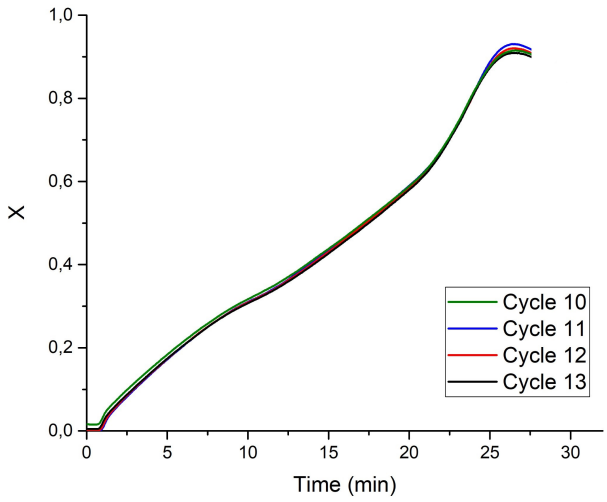

Figure 5.8: Reduction reactivity for cylcles 10, 11, 12, 13

An analogous procedure can be applied to the oxidation reaction, obtaining figure 5.9

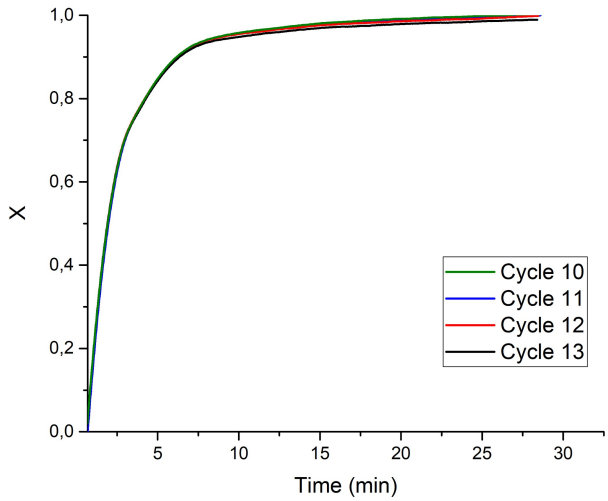

Figure 5.9: Oxidation reactivity for cylcles 10, 11, 12, 13

In figure 5.9 the curve rapidly increases and in about 15 minutes, the value of x approximately reaches 1; the obtained plateau indicates a complete hematite oxidation. Unfortunately this consideration is no longer valid for the reduction case (fig. 5.8), indeed no plateau appears. Furthermore, two inflection points are visible and they may demonstrate the presence of possible side reactions, following different kinetics.

Chapter 6

Simulation

In this chapter the software COMSOL Multiphysics is used; it is a program that encompasses every stage of the modeling process: from the definition of the geometry to the choice of the materials and the physics of the phenomenon under investigation, with the goal of carrying out computations and assessing the outcomes. In this thesis work, the software is employed to simulate the temperature distribution on the solar receiver of the paraboloid CSP system present on the Energy Center rooftop. The result will be then used in a second simulation, to verify the occurrence of the reduction of iron oxides and thus the feasibility of the thermochemical process.

COMSOL Multiphysics firstly requires the selection of the space dimension (3-D one in this case) and the type of study to carry out: whether stationary or time dependent. Being interested in the change of variables over time, a time dependent study is chosen; it will allow the investigation of temperature variation in time, when taking into account the heat transfer physics interface. While in the chemistry part, it will enable the calculation of the reaction kinetics and of the system's chemical composition.
The next step is the selection of the settings regarding the geometry and the materials, explored in the following section.

6.1 Geometry and materials

As already mentioned, this numerical analysis puts aside the parabolic dish concentrator, involving only the solar receiver reactor; the role played by the former one is approximated by a heat flux concentrated on the focal area, that will be one of the boundary conditions analyzed in section 6.2.

The geometry of the receiver is a hollow cylinder made of alumina, shown in figure 6.1[1]

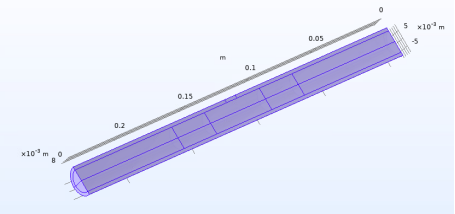

Figure 6.1: Receiver's geometry

More in detail, figure 6.2 depicts the solid domain, made up of alumina, figure 6.3 shows the porous domain, made up of hematite powder and glass wool, while figure 6.4 represents the fluid domain, in which nitrogen flows from left to right.

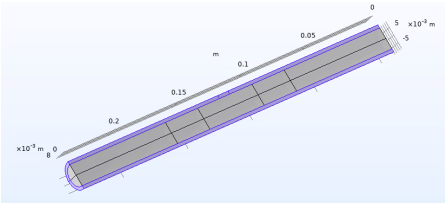

Figure 6.2: Solid domain

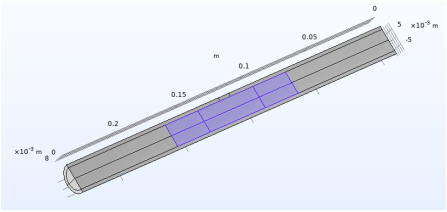

Figure 6.3: Porous domain

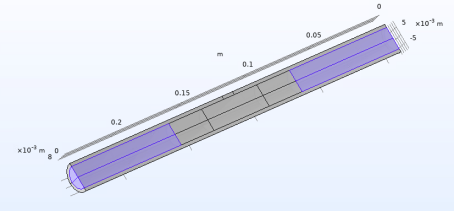

Figure 6.4: Fluid domain

The receiver's internal (D_{int}) and external (D_{ext}) diameters, as well as its length (L) are retrieved from actual measurements of the reactor and they are reported in table 6.1.

[1]For the sake of visualization, half cylinder is reported in fig.6.1 and all the following ones.

Table 6.1: Geometrical information

Geometry of the receiver		
Internal diameter	D_{int}	13 mm
External diameter	D_{ext}	18 mm
Length	L	240 mm

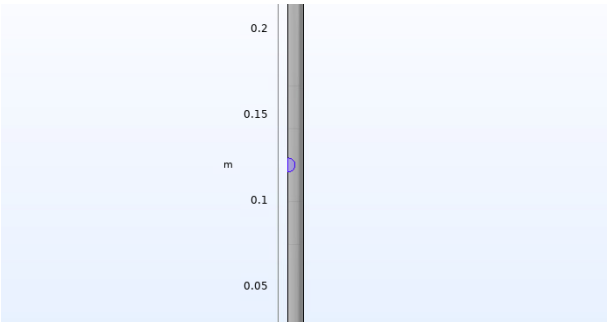

Figure 6.5: Detail of the focal area where the solar power is concentrated

In addition, the center of the cylinder is characterized by a porous region, being filled with hematite powder and glass wool; the former is approximated by a small cylinder with a $\frac{L}{D}$ ratio equal to 1,5 (fig.6.6). On the other hand, glass wool is adopted with the aim of holding in place the iron oxides and it can be seen as two cylinders with a length of 25 mm each (fig.6.7).

The remaining domain (fig.6.4) is occupied by nitrogen, flowing in the axial direction, with a speed of 0,045 m/s.

Table 6.2 summarizes the paramount properties implemented in COMSOL about alumina, hematite, glass wool and nitrogen.

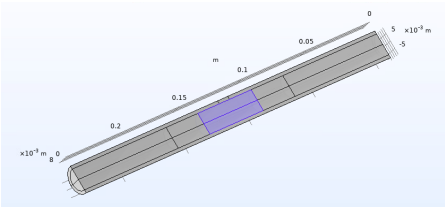

Figure 6.6: Hematite domain

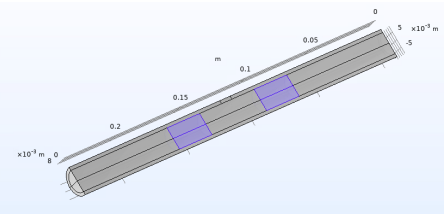

Figure 6.7: Glass wool domain

Table 6.2: Material properties implemented in COMSOL

Alumina (Al_2O_3)		
ρ	$[kg/m^3]$	3900
c_p	$[J/(kg \cdot K)]$	900
k	$[W/(m \cdot K)]$	27
α	$[1/K]$	$8 \cdot\ 10^{-6}$
Hematite (Fe_2O_3)		
ρ	$[kg/m^3]$	5300
c_p	$[J/(kg \cdot K)]$	938
k	$[W/(m \cdot K)]$	17,6
ϵ	$[-]$	0,836
μ	$[m^2]$	10^{-9}
Glass wool		
ρ	$[kg/m^3]$	22
c_p	$[J/(kg \cdot K)]$	850
ϵ	$[-]$	0,2
Nitrogen		
R^*	$[J/(kg \cdot K)]$	296,8
c_p	$[J/(kg \cdot K)]$	1040
γ	$[-]$	1,4
M	$[kg/mol]$	0,02801

6.2 Temperature distribution

In this section a brief analysis of the equations implemented in COMSOL is reported, followed by the outcomes obtained.

6.2.1 Relevant equations

The two physical interfaces chosen in the modeling are *Heat transfer in porous media* and *Chemistry*; on the other hand, the fluid dynamic model has been disregarded, in order to avoid an excessive computational time.
The Heat transfer in porous media interface gives a solution for the energy equation (eq.6.1), valid throughout the domain.

$$(\rho c_p)_{eff} \cdot \frac{\delta T}{\delta t} + \rho_f c_{p,f} \cdot \mathbf{u} \cdot \nabla T + \nabla \mathbf{q} = Q \tag{6.1}$$

$$\mathbf{q} = -k_{eff} \cdot \nabla T \tag{6.2}$$

The heat transfer equation (eq.6.1) is applicable under the hypothesis of local thermal equilibrium [2], negligible pressure work and viscous dissipation.

In particular:

- $(\rho c_p)_{eff}$ is the effective volumetric heat capacity at constant pressure
- $\mathbf{u}$ is the velocity field
- $\mathbf{q}$ is the conductive heat flux vector, defined by Fourier's law of conduction (eq.6.2)
- Q is the heat source term (i.e. the concentrated solar power)
- ρ_f is the density of the fluid. Nitrogen is assumed to be an ideal gas and thus its density is given by eq.6.3:

$$\rho_f = \frac{p}{R^* \cdot T} \tag{6.3}$$

- k_{eff} is the effective thermal conductivity

More in detail, both $(\rho c_p)_{eff}$ and k_{eff} are obtained considering a weighted average mean of solid (ρ_p, $c_{p,p}$, k_p) and fluid ((ρ_f, $c_{p,f}$, k_f) properties:

$$(\rho c_p)_{eff} = \epsilon \rho_p c_{p,p} + (1-\epsilon)\rho_f c_{p,f} \tag{6.4}$$

$$k_{eff} = \epsilon k_p + (1-\epsilon) k_f \tag{6.5}$$

[2]The assumption of local thermal equilibrium denotes a common temperature for the solid and fluid phase [71]

It can be noted that ϵ refers to the porosity of hematite.
The *Chemistry* interface involves the implementation of the overall reduction reaction of hematite, that will be deeply investigated in section 6.3 and it is now useful to take into account the thermochemical characteristics of the ideal gas mixture in the pipe.

6.2.2 Boundary conditions and results

As regards the values of solar irradiance and wind speed, that are among the boundary conditions imposed, they are retrieved from experimental data, collected on the Energy Center rooftop. These meteorological data have been recorded for about two months and in this simulation the best one are chosen; as can be seen in figures 6.8 and 6.9, we are dealing with solar radiation, wind speed and air temperature of 26^{th} May 2023.

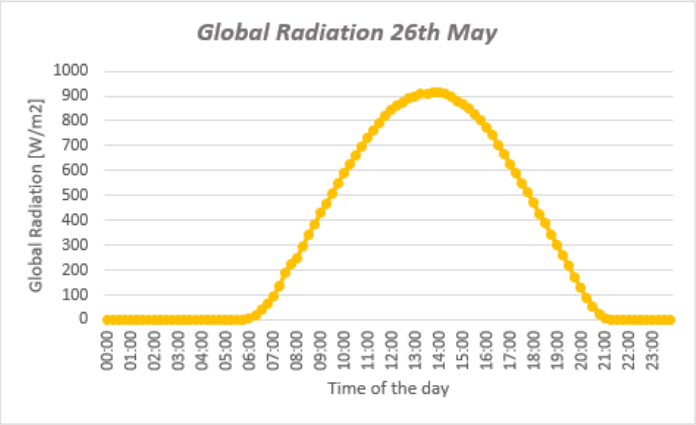

Figure 6.8: Global radiation on 26^{th} May 2023

Moreover, in order to exploit the best meteorological conditions, we can focus on the hours within 1 pm and 3 pm, since they are the ones characterized by the highest values of solar radiation, as shown in picture 6.10.

Hence, the values of solar irradiance and wind speed implemented in COMSOL are given by the arithmetic mean of those values in the time range taken into account.
Particularly, a first boundary condition is related to the thermal flux and is described by equation 6.6:

$$-\mathbf{n} \cdot \mathbf{q} = q_0 \tag{6.6}$$

in which:

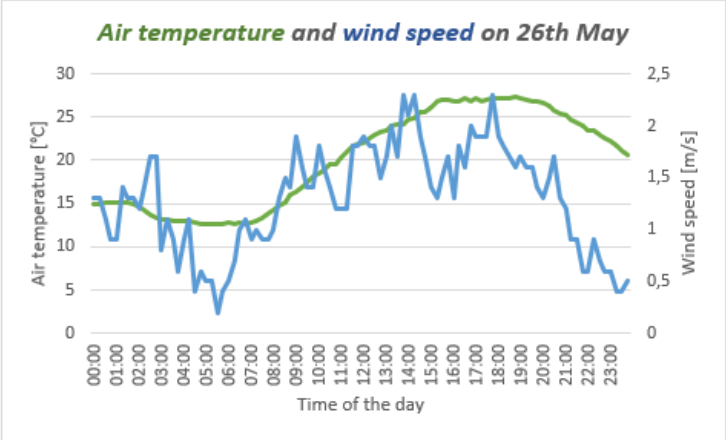

Figure 6.9: Temperature of air and wind speed on 26^{th} May 2023

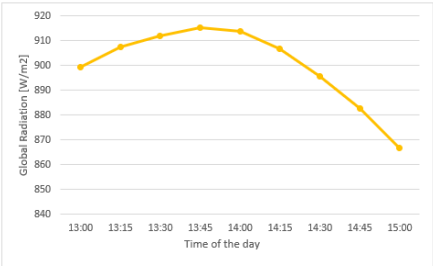

Figure 6.10: Detail of solar radiation on 26^{th} May 2023

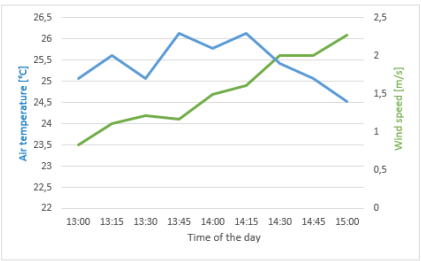

Figure 6.11: Detail of air temperature and wind speed on 26^{th} May 2023

- **q** is the conductive heat flux vector
- **n** is the normal vector on the boundary
- q_0 is the inward heat flux, perpendicular to the boundary

In this analysis, q_0 takes into account the solar irradiance concentrated on the focal area of the receiver (described in section 3.4) and is equal to 899 W/m^2. As already mentioned, this value approximates the role of the solar dish, which has been disregarded in this simulation.
The second thermal-related boundary condition is applied to the external walls of the receiver, except for the focal area, and it deals with the convective cooling due to the surrounding air. In this case, equation 6.6 becomes:

$$-\mathbf{n} \cdot \mathbf{q} = h(T_{ext} - T) \tag{6.7}$$

where:

- h is the convective heat transfer coefficient
- T_{ext} is the air temperature, far away from the boundary (i.e. 293 K)
- T is the temperature of the receiver

The primary challenge is related to the determination of the convective heat transfer coefficient, which depends on the properties of the fluid and the temperature on the surface of the pipe [71].
In this analysis, external forced convection on a cylinder in cross flow is selected and the convective heat transfer coefficient implemented in COMSOL is:

$$h = \frac{k}{D}\left(0{,}3 + \frac{0{,}62 R_{eD}^{1/2} P_r^{1/3}}{\left(1 + \left(\frac{0{,}4}{P_r}\right)^{2/3}\right)^{1/4}}\left(1 + \left(\frac{R_{eD}}{282000}\right)^{5/8}\right)^{4/5}\right) \tag{6.8}$$

In particular:

- k is the thermal conductivity of the fluid [W/mK]
- $P_r = \frac{\mu c_p}{k}$ is the Prandtl number
- $R_{eD} = \frac{\rho U D}{\mu}$ is the Reynolds number

The material properties are evaluated by the software at $\left(\frac{T+T_{ext}}{2}\right)$, while the input values introduced are:

- D=0,18 m cylinder diameter
- U=1,9 m/s velocity of the fluid

The other boundary conditions are related to the dimension of the different domains, already described in section 6.1.
Figure 6.12 shows the temperature distribution in the no-load condition: the alumina pipe is filled only with air.

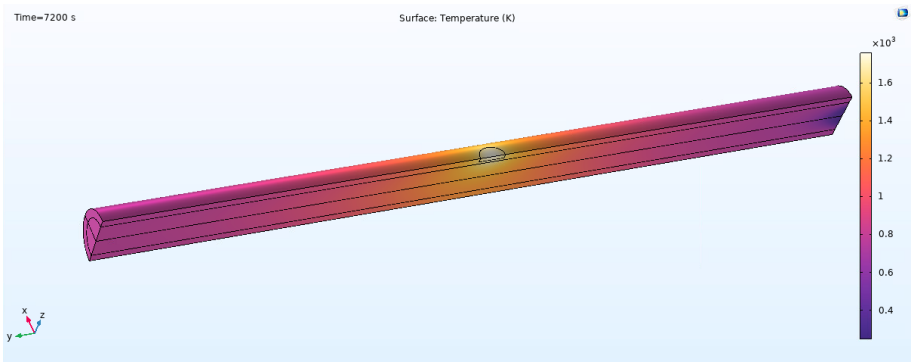

Figure 6.12: No-load test

A more complete result is depicted in figure 6.13; in this case, the receiver has a central porous domain, made of hematite and glass wool, while the remaining internal volume is filled with nitrogen. The focal area reaches a temperature of 1300 K, while looking at the portion where hematite is located, temperature is about 1200 K. Moving from the central part to the edges of the receiver, temperature decreases due to the presence of the glass wool (a thermal insulator) and to the fact that we are getting away from the focal area, where the thermal flux is concentrated. The temperature at the edges of the pipe is around 400 K. This outcome is obtained after a 2 hours simulation, with the aim of getting a configuration as stable as possible.

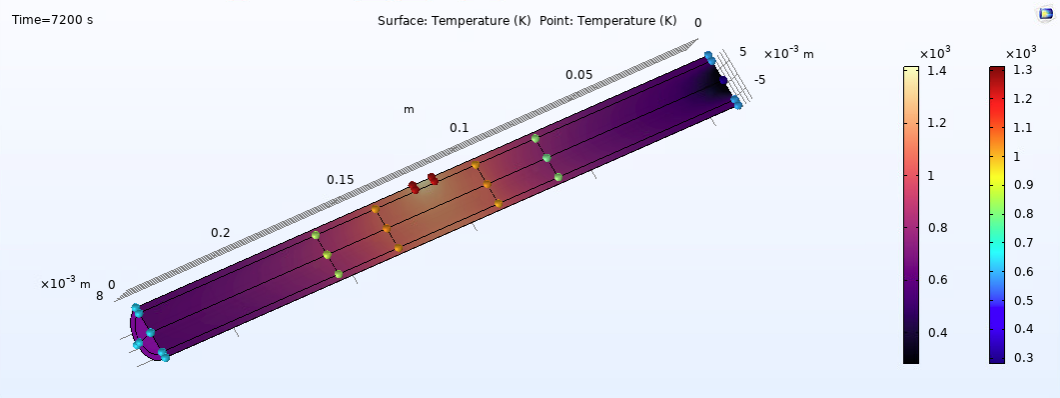

Figure 6.13: Loaded test

6.3 Reduction Reaction

Being the thermal reduction reaction the most problematic step in chemical looping technology, it is now investigated from a kinetic point of view and then simulated in COMSOL.

6.3.1 Reaction mechanism

The kinetic studies carried out by *Monazam et al.* [70] demonstrate that the reduction of Fe_2O_3 with CH_4 is a multi-step process, involving two parallel reactions: R_1 and R_2. In particular, R_1 is a 1^{st} order reaction, while R_2 is a sigmoid curve, that take place at the same time and are depicted in figure 6.14 together with their sum $(R_1 + R_2)$.

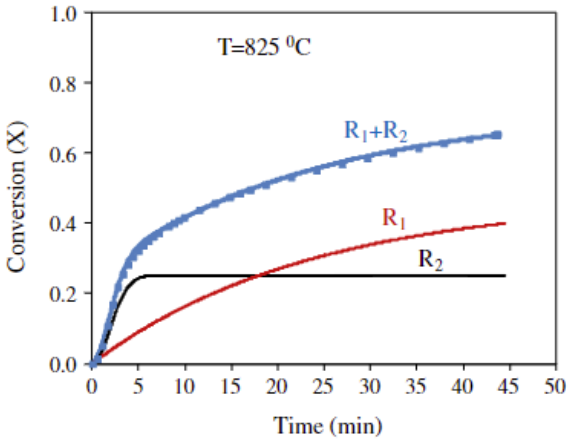

Figure 6.14: Predicted curves of conversion of hematite with 20% of methane as function of time [70]

Figure 6.14 records the degree of conversion (X) against time, at a constant temperature (825 °C) regarding the reduction of Fe_2O_3 with 20% CH_4. Approximately in the first 10 minutes, the entire reduction $(R_1 + R_2)$ is mainly ruled by the behaviour of reaction R_2 and therefore R_1 will have a small impact on these early stages. On the other hand, reaction R_1 shows a lower time response and a higher influence only in its final stages [70].
Moreover, both R_1 and R_2 in figure 6.14 achieve a steady state condition, even though it happens for distinct values of X.

As regards the activation energy for a multi-step process, *Vyazovkin and Linert* [72] showed that it is determined by the activation energies of the individual reactions and their contributions to the entire process rate at a certain degree of conversion. Figure 6.15 depicts the decrement of the activation energy when the extent of conversion (X) rises; this trend is compliant with a multi-step reduction model, characterized by nucleation and growth processes.

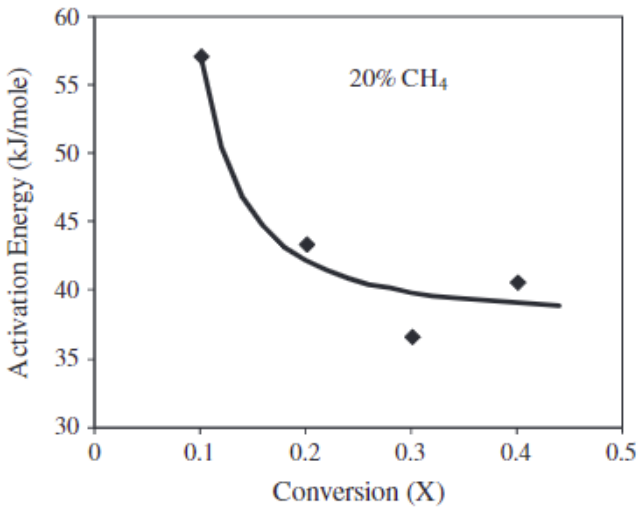

Figure 6.15: Activation energy as function of X[70]

In proposing their kinetic model, *Monazam et al.* highlight that the hematite to magnetite reduction most likely happens in an exothermic way, in the early stages of conversion, which leads to elevated activation energy. Indeed, this starting high value is due to two contributions; the enthalpy of reversible processes and the activation energy of irreversible ones.
On the contrary, the lower value of activation energy with increased conversion is a feature of a reversible endothermic process [70].
Eventually, a plausible reaction mechanism involves two steps:

- **Decomposition of methane and reduction of Fe_2O_3 to Fe_3O_4**

$$3CH_4 \rightarrow 3C + 6H_2 \qquad \Delta H^0_{r,800C} = 268{,}34 \quad kJ/mol \tag{6.9}$$

$$CH_4 + 12Fe_2O_3 \rightarrow 8Fe_3O_4 + CO_2 + 2H_2O \qquad \Delta H^0_{r,800C} = 164{,}1 \quad kJ/mol \tag{6.10}$$

$$3C + 12Fe_2O_3 \rightarrow 8Fe_3O_4 + CO_2 + 2CO \qquad \Delta H^0_{r,800C} = 346{,}2 \quad kJ/mol \tag{6.11}$$

$$H_2 + 3Fe_2O_3 \rightarrow 2Fe_3O_4 + H_2O \qquad \Delta H^0_{r,800C} = -6{,}75 \quad kJ/mol \tag{6.12}$$

$$\begin{aligned} &4CH_4 + 27Fe_2O_3 \rightarrow 18Fe_3O_4 + 2CO_2 + 2CO + 3H_2O + 5H_2 \\ &\Delta H^0_{r,800C} = 771{,}86 \quad kJ/mol \end{aligned} \tag{6.13}$$

- **Decomposition of methane and reduction of Fe_3O_4 to FeO**

$$2CH_4 \rightarrow 2C + 4H_2 \qquad \Delta H^0_{r,800C} = 178{,}9 \quad kJ/mol \tag{6.14}$$

$$CH_4{+}4Fe_3O_4 \rightarrow 3FeO{+}2H_2O{+}CO_2 \qquad \Delta H^0_{r,800C} = 377{,}9 \quad kJ/mol \tag{6.15}$$

$$2C + 3Fe_3O_4 \rightarrow 9FeO + CO_2 + CO \qquad \Delta H^0_{r,800C} = 377{,}5 \quad kJ/mol \tag{6.16}$$

$$H_2 + Fe_3O_4 \rightarrow 3FeO + H_2O \qquad \Delta H^0_{r,800C} = 46 \quad kJ/mol \tag{6.17}$$

$$\begin{aligned} &3CH_4 + 8Fe_3O_4 \rightarrow 24FeO + 2CO_2 + CO + 3H_2O + 3H_2 \\ &\Delta H^0_{r,800C} = 981 \quad kJ/mol \end{aligned} \tag{6.18}$$

The overall reaction of hematite (Fe_2O_3) to wustite (FeO) is given by eq.6.19

$$\begin{aligned} &7CH_4 + 27Fe_2O_3 \rightarrow 10Fe_3O_4 + 24FeO + 4CO_2 + 3CO + 6H_2O + 8H_2 \\ &\Delta H^0_{r,800C} = 1752{,}9 \quad kJ/mol \end{aligned} \tag{6.19}$$

In particular, equation 6.13 represents the already mentioned reaction R_2, while eq.6.18 explicitly expresses R_1. *Monazam et al.* evaluated an activation energy of 39,3 kJ/mol for R_2 and of 34,4 kJ/mol for R_1 [70].

Figure 6.16 illustrates the gases emitted during the reduction against time, at T=825 °C, obtained by means of a mass spectrometer. As regards the behaviour of methane concentration: it rises quickly, reaching a provisional maximum at approximately one minute after the beginning of the reaction.
At the same time, also the concentrations of CO_2 and H_2 achieve a peak; after that, CO_2 concentration rapidly decreases and it reaches zero within the first five minutes of the reduction. On the contrary, H_2 concentration drops in a smoother way. Meanwhile, the concentration of CH_4 slightly rises until the end of the 45 minutes.

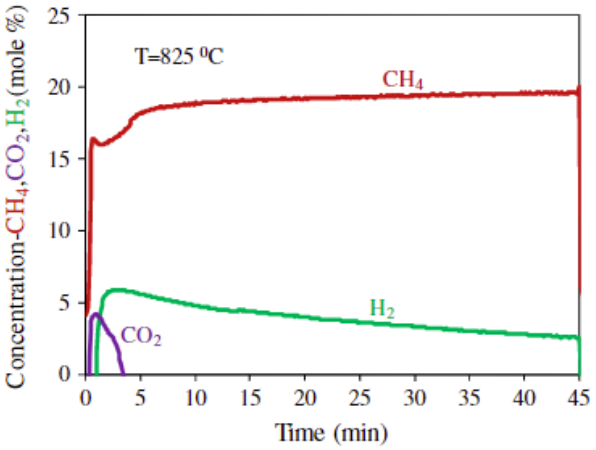

Figure 6.16: Outlet gases for hematite reduction with 20% CH_4[70]

However, *Monazam et al.* [70] highlight that part of methane is only partially oxidised to CO and H_2; as a consequence they realized that their study, initially devoted to chemical looping combustion, involved also chemical looping partial oxidation. Thus, the outcome is not only a CO_2 stream ready to be captured, but also a mixture of H_2 and CO (e.g. syngas).
In addition, the beginning of the Fe_2O_3 reduction follows a topochemical model [70], since the almost immediate release of CO and H_2 is ensured by the reactivity of CH_4. Then, after the deposition of a thin film of wustite on the surface, the mechanism switches to two concurrent reaction processes:

- The conversion of Fe_2O_3 to FeO, producing CO and H_2, follows intrinsic topochemical kinetics;
- The conversion ofFe_2O_3 to Fe_3O_4 with the production of CO_2 and H_2O, is ruled by nucleation and growth kinetics.

6.3.2 Reaction simulation

Reaction engineering physics is implemented in COMSOL, considering a zero-dimensional model, in order to simulate the reduction reaction.
The input parameters introduced in the software are:

- Temperature $T = 1300$ K, as previously obtained for the focal area of the receiver [3]
- Total inlet flow rate of 500 $\frac{cm^3}{min}$, made up of 35% CH_4 and 65% N_2.

As regards the kind of reactor, a constant volume, CSTR (Continuos Stirred-Tank Reactor) is selected among the proposed ones; the main feature of this reactor is the assumption of perfect mixing, meaning that the output composition is the same as the composition of the species within the reactor itself.
In particular, COMSOL implements the equation of the volumetric production rate, v_p:

$$v_p = \frac{R_g \cdot T}{p} \cdot V_r \cdot \Sigma R_i \tag{6.20}$$

where:

- R_g is the gas constant $[\frac{J}{mol \cdot K}]$
- T is the operating temperature [K]

[3]The selection of T allows the exclusion of the energy balance in the model

- p is the operating pressure [Pa]
- V_r is the reactor volume $[m^3]$
- R_i is the species rate $[\frac{mol}{m^3 \cdot s}]$

The software requires the insertion of the value of V_r: it consideres the portion of the receiver where the reduction reaction takes place. Thus, the volume of the reactor can be evaluated taking into account the internal diameter of the pipe ($D_i = 0{,}013$ m) and the L/D ratio equal to 1,5. The result is

$$V_r = \pi \cdot \left(\frac{D_i}{2}\right)^2 \cdot L = 2{,}59 \cdot 10^{-6} \quad m^3 \tag{6.21}$$

In this analysis, hematite particles are approximated as spheres with a diameter of 80 μm [73].
Taking into account the definition of the specific area, eq. 6.22 [74]:

$$a = \frac{N_{spheres} \cdot A_{sphere}}{V_{reactor}} = \frac{6 \cdot (1-\epsilon)}{d} \quad \left[\frac{m^2}{m^3}\right] \tag{6.22}$$

in which:

- ϵ is the porosity
- d is the diameter of the sphere

deriving the number of spheres within our volume:

$$N_{spheres} = \frac{6 \cdot (1-\epsilon) \cdot V_{reactor}}{\pi d^3} = 6758356 \tag{6.23}$$

and thus the area of reaction A_r to implement in the software:

$$A_r = N_{spheres} \cdot 4\pi \left(\frac{d}{2}\right)^2 = 0{,}14 \quad m^2 \tag{6.24}$$

As regards the amount of hematite introduced inside the receiver, it is set to 2,7 g corresponding to 0,017 mol and leading to a surface concentration of 0,12 $\frac{mol}{m^2}$. Nonetheless, since hematite includes three oxygen atoms per molecule, there are more reactive sites; as a consequence the surface concentration introduced in COMSOL is set to 0,37 $\frac{mol}{m^2}$, obtained by tripling the previous value of 0,12 $\frac{mol}{m^2}$.
The initial concentrations $[mol/m^3]$ of all the gaseous species involved are considered

to be null.
Now the software requires the addition of all the chemical reactions taking place. Following the work of *Monazam et al.* [70], we are dealing with both chemical looping combustion and chemical looping reforming (in particular, chemical looping partial oxidation). As a consequence, we can introduce equation 6.19 describing the reduction of hematite to wustite and equation 4.12, that take into account the partial oxidation of the fuel; by applying this latter one to the sequential reduction of iron oxides ($Fe_2O_3 \rightarrow Fe_3O_4 \rightarrow FeO$), we obtain:

$$Fe_2O_3 + CH_4 \rightarrow 2FeO + CO + 4H_2 \tag{6.25}$$

$$Fe_3O_4 + CH_4 \rightarrow 3FeO + CO + 2H_2 \tag{6.26}$$

Nonetheless, as already mentioned, CLPO comes with a series of side reactions, that have to be introduced in COMSOL, to get more accurate results:

- Carbon deposition on the oxygen carrier (eq.4.13), due to the lower and lower O_2 availability. It increases the overall production of hydrogen but it also fouls the catalyst, undermining the efficiency of the entire process.
- Carbon gasification (eq.4.14) and the Boudouard reaction (eq.4.15) can occur when steam is introduced in the reactor, mitigating carbon deposition
- Steam reforming (eq.4.16) that takes place due to the favourable high temperature and the presence of H_2O.

All these reactions are assumed to be irreversible and COMSOL needs for each of them the values of the activation energy and frequency factor; indeed, the software implements the reaction constants in the Arrhenius equation:

$$k = A \cdot \left(\frac{T}{T_{ref}}\right)^n \cdot exp\left(\frac{E}{R_g \cdot T}\right) \tag{6.27}$$

where:

- $T_{ref} = 1K$
- T is the operating temperature [K]
- R_g is the gas constant $[\frac{J}{mol \cdot K}]$
- n is the temperature exponent; in this study $n = 0$, because all the other parameters of eq. 6.27 are referred to the operating temperature
- k is the rate constant, that indicates the connection between the rate of a chemical reaction and the concentration of the reacting components [75]

- A is the frequency factor (also called Arrhenius factor or pre-exponential factor); it concerns the frequency of molecules colliding in the proper orientation and with enough energy to start a reaction. Being related to molecular collision, it depends on temperature. It has to be empirically determined, since it varies according to the reaction. It is expressed in $[\frac{m^3}{mol \cdot s}]$ in case of a 2^{nd} order rate constant, in $[\frac{1}{s}]$ for a 1^{st} order rate constant or in $[\frac{m}{s}]$ for a 0^{th} order one [76]
- E is the activation energy, a threshold value that has to be provided to make the reaction occur. It is expressed in $[\frac{kJ}{mol}]$

In the following table are summarized the values of frequency factor and activation energy inserted in COMSOL for all the chemical reactions implemented, retrieved from *Lu et al.*[77] and *Slycke et al.* [78]:

Table 6.3: Frequency factor A and activation energy E values [77] [78]

Reaction	A $[m^3/(mol \cdot s)]$	E $[kJ/mol]$
Reduction of Fe_2O_3 to Fe_3O_4 (eq.6.13)	$133 \cdot y_{CH4}^{1,06}$	74
Reduction of Fe_3O_4 to FeO (eq.6.18)	$4{,}759 \cdot y_{CH4}^{0,636}$	74
Partial oxidation of CH_4 with Fe_2O_3 (eq.6.25)	$133 \cdot y_{CH4}^{1,06}$	93
Partial oxidation of CH_4 with Fe_3O_4 (eq.6.27)	$133 \cdot y_{CH4}^{1,06}$	93
Carbon deposition (eq.4.13)	$1{,}3 \cdot 10^7$ [m/s]	214
Carbon gasification (eq.4.14)	$1{,}8 \cdot 10^4$	172
Boudouard reaction (eq.4.15)	$1{,}2 \cdot 10^6$	185
Steam reforming (eq.4.16)	$1{,}3 \cdot 10^7$ $[1/s]$	214

The result of the simulation in COMSOL is depicted in figure 6.17 that shows the concentration of the outlet gases (expressed in $[\frac{mol}{m^3}]$) produced during 30 minutes of reduction:

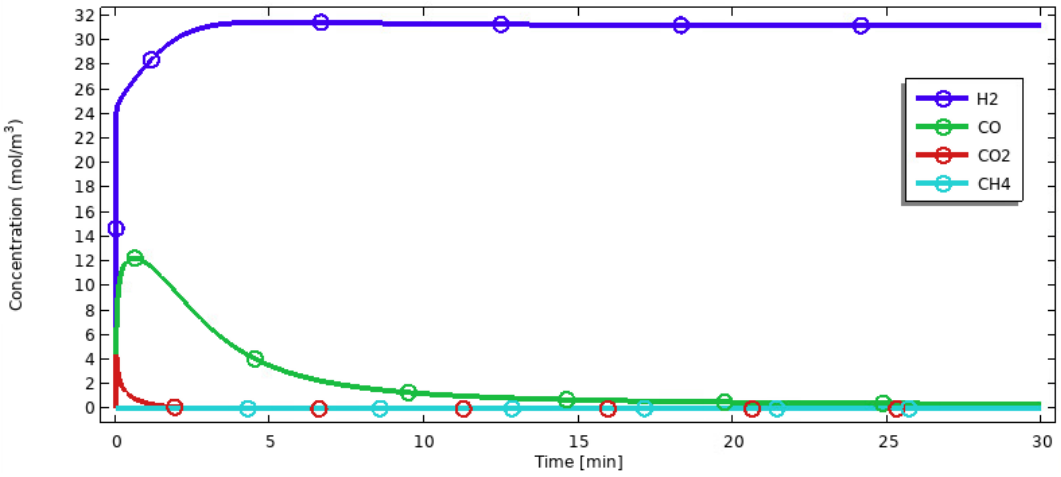

Figure 6.17: Concentration of outlet gases against 30 minutes

As soon as methane is injected (at 0 minutes), hydrogen, carbon monoxide and carbon dioxide are produced; CO_2 reaches its peak of about 4 mol/m^3 immediately, then quickly decreases and eventually disappears.
CO rapidly rises and in about one minute achieves its maximum value of 12 mol/m^3 and then smoothly reduces. The decrement in the production of carbon dioxide and carbon monoxide might be due to the rise of carbon deposition over the oxygen carrier, shown in figure 6.19.
A completely different behaviour is the one followed by hydrogen: in only three and a half minutes, it reaches around 30 mol/m^3 and then it does not vary for the rest of the reduction time.
The fact that methane is not present as an outlet gas of the reduction reaction, meaning that it all reacted, is more likely a consequence of a maybe too idealistic model.
A similar outcome is obtained by plotting the concentration of the produced gases in [mole%] against time, as in figure 6.18

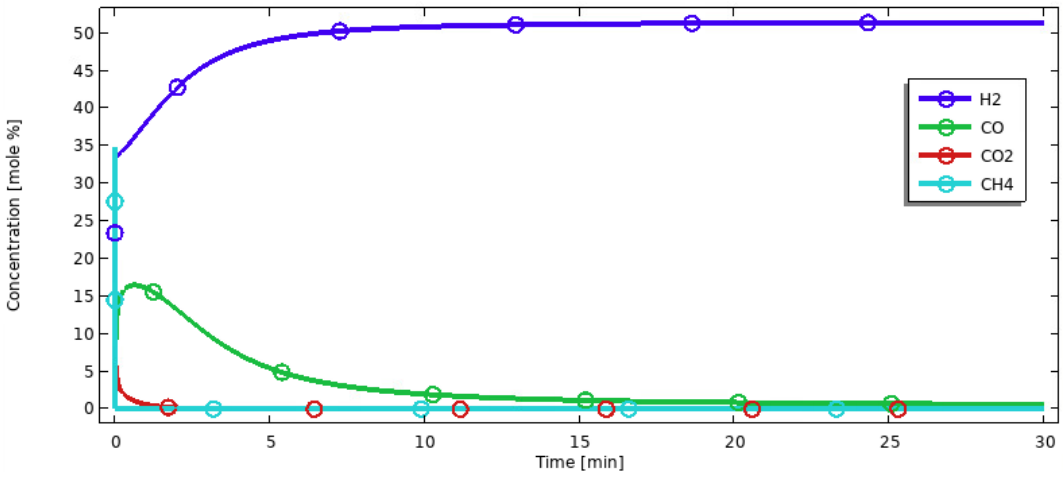

Figure 6.18: Concentration of outlet gases in [mole %] against 30 minutes

Another interesting image is 6.19 that depicts the fluctuations of the solid reactants against time:

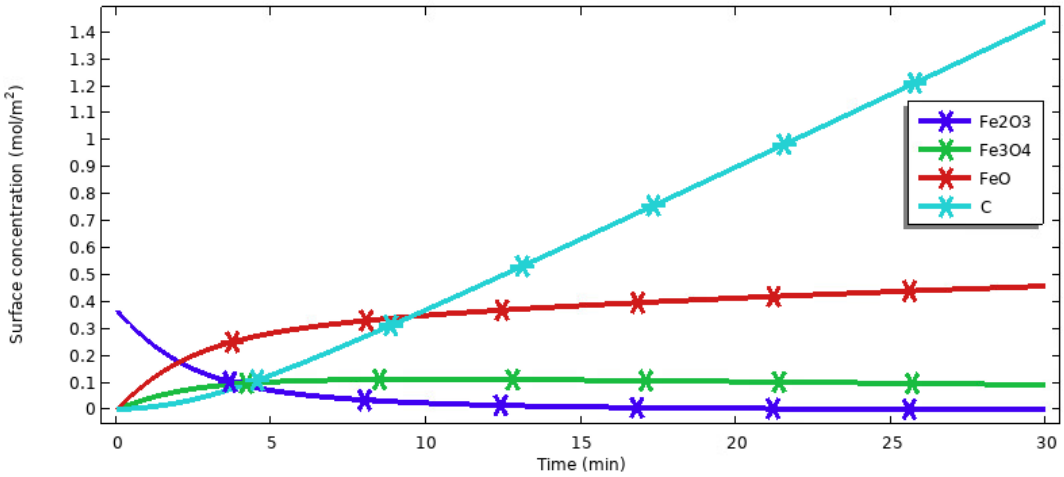

Figure 6.19: Surface concentration of solid reagents in time

In particular, on the vertical axis the surface concentration of the solid components is reported.
As already mentioned, a starting value of 0,37 mol/m^2 of Fe_2O_3 is introduced in COMSOL and figure 6.19 shows its evident decrement.
The reduction of hematite, following two simultaneous reactions (6.13 and 6.18), produces magnetite and wustite. In only five minutes, both Fe_3O_4 and FeO reach a stable value: 0,1 mol/m^2 and approximately 0,45 mol/m^2, respectively. Thus, the complete reduction of Fe_2O_3 to FeO prevails over the partial one to Fe_3O_4.
Unfortunately, the curve that shows the highest increase is the one of carbon, witnessing the presence of a deep carbon deposition. Indeed, the surface concentration of carbon keeps increasing during the entire simulation, reaching a value higher than 1,4 mol/m^2 after 30 minutes. As already mentioned, the high operating temperature fosters the cracking of CH_4 molecules, causing carbon atoms to stratify over the surface of iron oxides and thus deactivating them.

Chapter 7

Second experimental section

In this section a brief description of the parabolic dish collector exploited during the experimental tests is provided. Then an investigation of the most suitable materials for the solar receiver is carried out, focusing on two ceramics: alumina (Al_2O_3) and silicon carbide (SiC).

7.1 Solar dish collector by El.Ma.

In this thesis work, the CSP system taken into account is the parabolic dish collector installed on the Energy Center rooftop, manufactured by El.Ma. Electronic Machining.
Picture 7.1 illustrates the original prototype, meant to produce electricity through a Stirling engine, placed on the focus of the paraboloid.

Figure 7.1: Parabolic dish concentrator by El.Ma.[79]

Figure 7.2: Detail of the parabolic dish concentator by El.Ma.[79]

The main elements that constitute the considered solar collector are:

- **Paraboloidal dish concentrator**: it is made of aluminum and internally

coated by a flexible and economic polymer film; in particular, as depicted in fig.7.2, the reflecting surface is made up of six big petals and then each of them includes eight smaller petals, featuring a reflective factor close to the unit [79]

- **Receiver support**: it includes an arm assembled on the vertex of the paraboloidal
- **Receiver**: it is a cavity receiver, made of alumina. It replaces the Stirlimg engine of the original prototype
- **Bearing structure**: it keeps the concentrator in a given position and it lets it rotate alonf two axes
- **Sun tracking system**: being a point-concentrating system, the solar dish necessitates a 2-axes tracking, in order to guarantee an optimal exposure to the Sun rays. In the specific case, the plant has an automatic solar tracking system that can be also run manually, by setting the desired values for altitude and azimuth angle. Figure 7.3 shows the two-axes system, according to altitude-azimuth tracking:

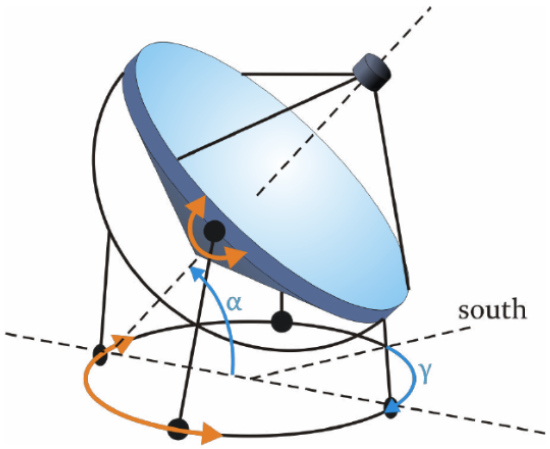

Figure 7.3: Altitude-azimuth tracking system[39]

In particular, the altitude angle defines the paraboloidal's angular direction in relation to the horizontal plane, while the azimuth angle is related to the angular position with respect to the South in the same plane.

Table 7.1 summarizes the productive features of this prototype, assuming a solar direct irradiance of 800 W/m^2:

Table 7.1: Productive characteristics of El.Ma. solar dish [79]

Absorbing surface	4,5 m^2
Optimal concentrated power	2,8 kW
Temperature in the focal point	higher than 1800 °C

7.2 Receiver materials

As already mentioned in section 3.2, the solar receiver is the core of CSP systems and the choice of suitable materials is paramount to enable the receiver withstand the remarkable thermal gradients to which it is exposed.
To figure out which are the most proper materials, several parameters are taken into account, such as thermal conductivity, chemical stability, thermal shock resistance, coefficient of thermal expansion.
Thanks to their outstanding chemical stability [1] and high melting point, ceramic materials are extensively used for this purpose; nonetheless, they feature a modest resistance to thermal stresses [80]. Particularly, the sudden temperature variations generate mechanical stresses within the material that in turn cause crack nucleation and propagation; eventually, failure can occur.
This last phenomenon is related to thermal shock resistance, that cen be expressed in terms of temperature variation by eq.7.1[81]:

$$\Delta T = \frac{\sigma(1-\nu)}{E \cdot \alpha} \tag{7.1}$$

in which:

- α is the coefficient of thermal expansion
- ν is the Poisson's ratio
- σ is the applied stress
- E is the Young's module

[1] Good chemical stability prevents chemical reactions within the material (i.e. corrosion and oxidation)

Thus, a material experiences high compression under thermal stress, because of its high surface temperature and wide temperature profile [81].
Figure 7.4 depicts an overview about thermal shock resistance of different ceramic materials.

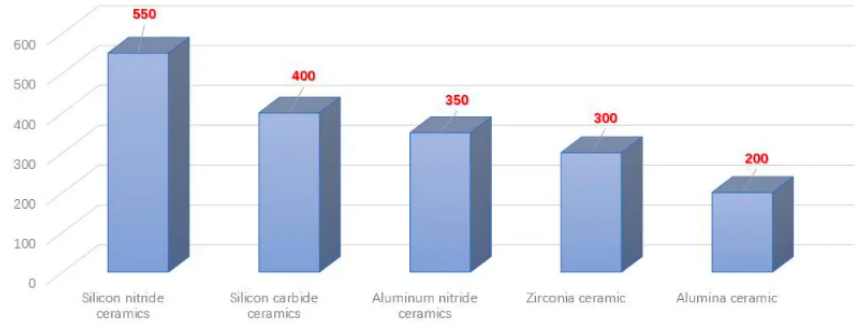

Figure 7.4: Thermal shock resistance of various ceramics [82]

Regarding the thermal expansion coefficient, it should be as low as possible; in this way, the size and shape of the materials show only little variations in response to abrupt temperature changes, decreasing the detrimental effects of thermal stresses. Ceramics are characterized by values of thermal expansion coefficients of the order of magnitude of 10^{-6} 1/°C, which are much lower than the ones of metals and plastics [83].
In the following subsections, alumina and silicon carbide ceramics samples are tested as receiver materials; their main properties are listed in table 7.2.

Table 7.2: Density ρ, Young's modulus E, coefficient of thermal expansion α, thermal shock resistance ΔT and thermal conductivity k of alumina and silicon carbide [84]

	ρ [g/cm^3]	E [GPa]	α [$10^{-6}/K$]	$\Delta T[K]$	k [W/mK]
Al_2O_3	3,9	380	8	200	30
SiC	3,1	500	4,6	450	170

7.2.1 Alumina receiver

The alumina solar receiver adopted in the experimental tests has a cylindrical shape, whose main features are reported in table 7.3:

Table 7.3: Geometry of alumina receiver

Alumina receiver		
Internal diameter	D_{int}	13 mm
External diameter	D_{ext}	18 mm
Length	L	240 mm

A preliminary analysis with Al_2O_3 was carried out in June 2023 to estimate the temperature achievable on the receiver. The outcomes were almost 1000 °C, nonetheless the receiver could not withstand the high ΔT and thus it failed.
A deeper study of thermal trends has been performed during the autumn season by carrying out three experimental tests in three different days: 10^{th}, 11^{th}, 12^{th} November 2023. In particular, in order to record the temperature reached by the sample, a thermocouple was placed in contact with the external surface of the alumina receiver, at the back of the focal area. The results are shown in the following figures:

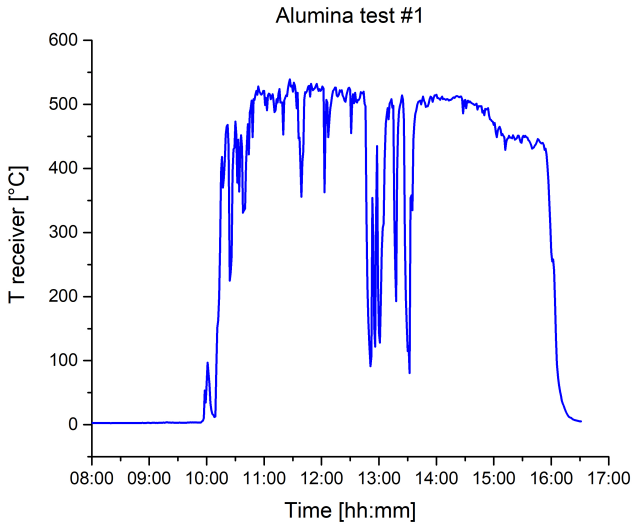

Figure 7.5: First experiment on alumina receiver

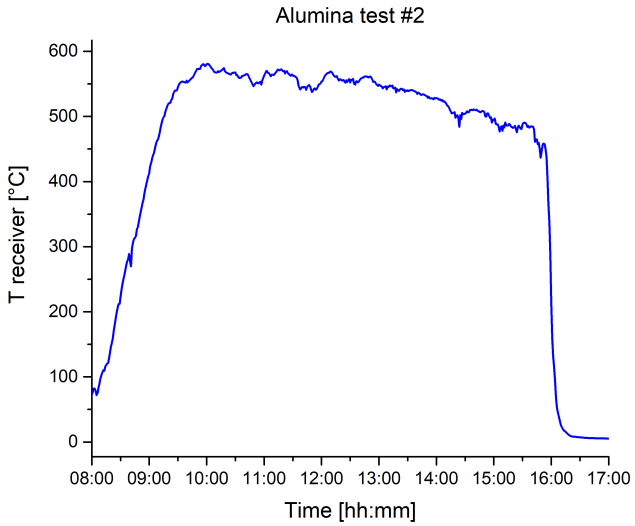

Figure 7.6: Second experiment on alumina receiver

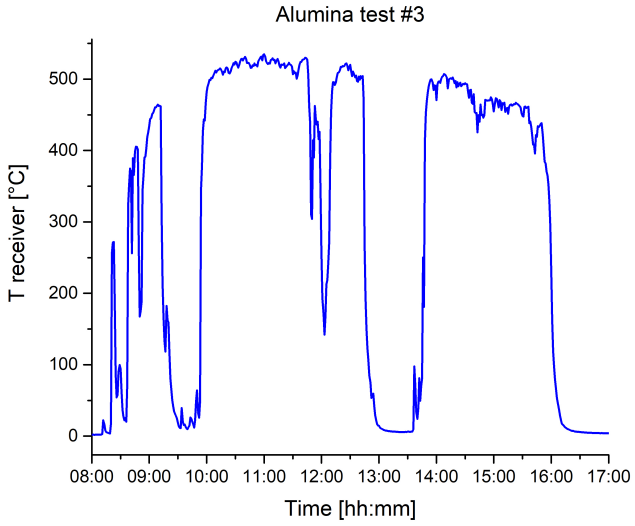

Figure 7.7: Third experiment on alumina receiver

The temperature achievable on the receiver mainly depends on two factors: solar irradiance and wind speed. As already explained, the higher the solar irradiance, the higher the power concentrated on the focal area of the receiver. On the other hand, as regard the wind speed, as the velocity increases, the convective losses rise too, causing a decrement of the reachable temperature.

Figure 7.6 shows a quite constant trend of the receiver's temperature within 9:30 a.m. and 4 p.m. On the contrary, figure 7.5 and figure 7.7 do not exhibit the same behaviour: several temperature variations occur in short time ranges. A possible reason is related to the passage of clouds (that decrease the direct component of the solar radiation) and to an increment of the wind velocity.
The maximum temperatures and the times at which they are achieved are reported in table 7.4.

Table 7.4: Max T in the three tests

	Max T [°C]	UTC Time
Test #1	539	11:27
Test #2	581	10:01
Test #3	535	11:00

The maximum temperature difference recorded during the entire day, taking into account all the three tests is 580 °C; however, looking at picture 7.5, it can be noted a temperature variation of about 430 °C occurring in only seven minutes (from 12:44 a.m. to 12:51 a.m.).

Since after these three tests the alumina receiver was undamaged, it can be deduced that it is able to withstand such temperature differences. Most likely the weather conditions in June 2023 are more extreme than the ones of October 2023, as witnessed by the following graphs:

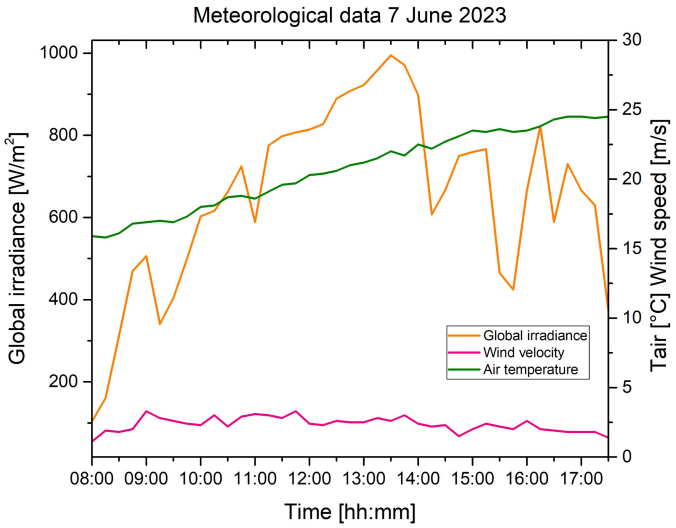

Figure 7.8: Meteorological data 7 June 2023

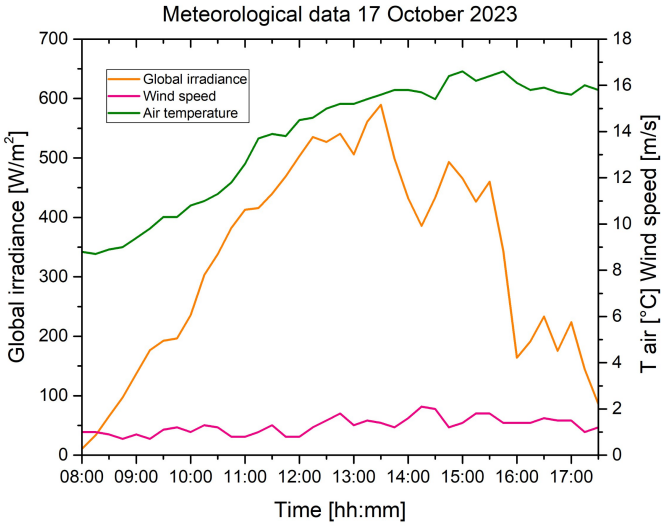

Figure 7.9: Meteorological data 17 October 2023

Hence, in order to investigate wider thermal gradients that could lead to the receiver's failure, these tests should be carried out during summer. Moreover, to prevent crack nucleation and propagation in the alumina receiver, we could improve the thermal shock resistance of this material by adding nanostructured coating [80]; otherwise, as done in this work thesis, we can exploit new materials, such as

silicon carbides.

7.2.2 Silicon carbide receiver

In this subsection the experimental tests performed with silicon carbide materials are reported. In this case, there is no availability of entire receivers made of SiC, but only little samples, in particular we are dealing with SiC matrix reinforced with UBE Tyranno S/PyC (black SiC) and SiC matrix reinforced with SiC/BN fibers (white SiC).
Table 7.5 reports the values of thermal expansion coefficients α for these two materials, valid in the temperature range 200-600 °C.

Table 7.5: Thermal expansion coefficients of silicon carbide

	$\alpha[10^{-6}/K]$
White SiC	5,2
Black SiC	5,4

In both cases, we are dealing with composite materials, particularly with SiC-based ceramic matrix composites (CMCs); the fascination in these materials is related to their high temperature applications, indeed they are employed in hot-zone elements of gas turbines and nuclear reactors [85].
SiC-based CMCs are characterized by different fibers embedded in a ceramic matrix (made up of either fibers or particles). Currently, pyrolytic carbon (PyC) and boron nitride (BN) are the most frequently employed interphase materials for SiC composites [86].
The enhanced properties guaranteed by such materials are several: high mechanical strength, chemical inertness, elevated thermal stability [85]

- **SiC matrix reinforced with SiC/BN fibers (white SiC)**
  In this material both SiC and boron nitride (BN) fibers are embedded into SiC matrix, ensuring high thermal resistance, elevated thermal conductivity and low thermal expansion coefficient [86]. The result is a CMC featuring improved thermal and mechanical characteristics with respect to the simple matrix material.
  The sample used in the experiments is a small rod, with a height of 17,11 mm and a thickness of 3,11 mm, depicted in figure 7.10

Figure 7.10: White SiC rod

As already done for the alumina receiver, the white SiC sample is placed on the receiver support and a thermocouple measures the temperature (as described in section7.2.1).

Figure 7.11: Receiver support and White SiC sample

Figure 7.12: White SiC sample installed in the solar dish system

Four tests have been performed in four different days: 3^{rd}, 6^{th}, 7^{th}, 8^{th} November 2023. The outcomes are depicted in the following figures:

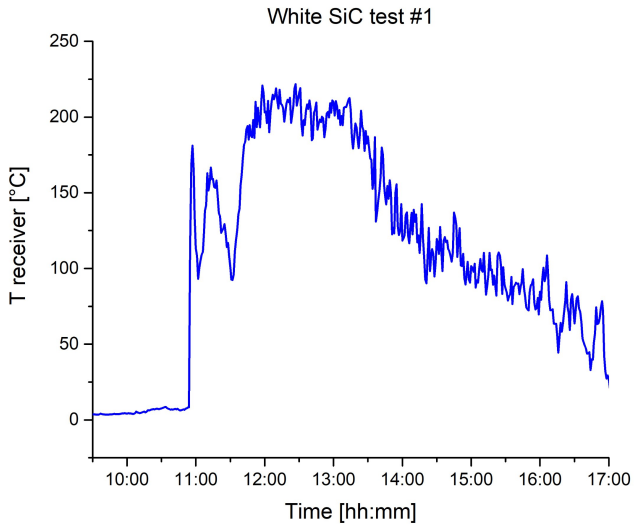

Figure 7.13: First experiment on white SiC sample

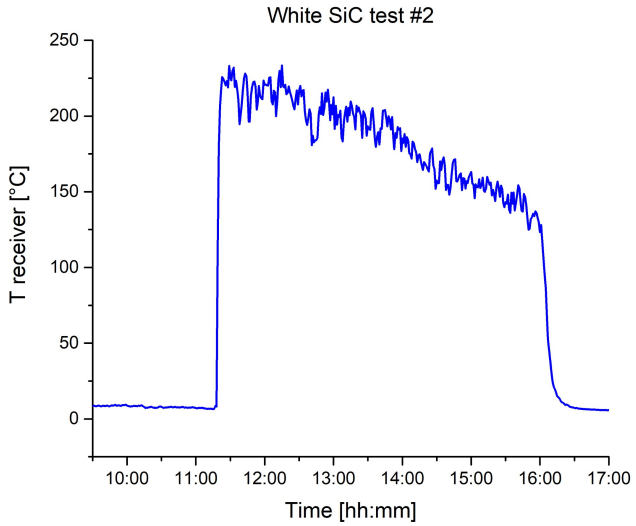

Figure 7.14: Second experiment on white SiC sample

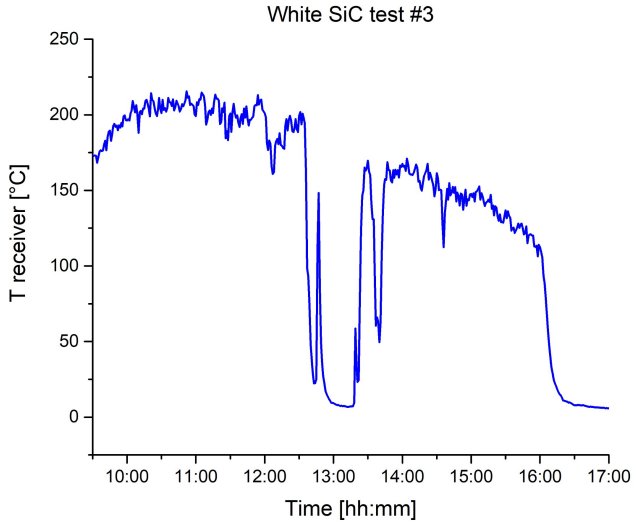

Figure 7.15: Third experiment on white SiC sample

Table 7.6 summarizes the maximum temperatures achieved in the experimental tests; as already explained during the analysis of the alumina receiver, also in this case the values of temperature are not so high, due to the not proper weather conditions of November 2023.

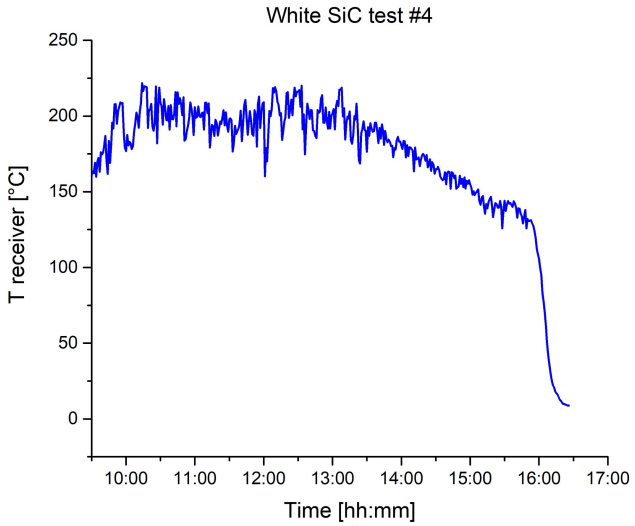

Figure 7.16: Fourth experiment on white SiC sample

Table 7.6: Max T in the four tests

	Max T [°C]	UTC Time
Test #1	222	12:27
Test #2	233	12:15
Test #3	216	10:52
Test #4	222	10:14

- **SiC matrix reinforced with UBE Tyranno S/PyC (black SiC)**
  This material was produced by BJS Ceramics GmbH in Augsburg, Germany [87]. In this case the SiC matrix of the CMC is coupled with Tyranno silicon carbide, by means of chemical vapor deposition. In addition, pyrolytic carbon is used as coating material for SiC fibers [87].
  Figure 7.17 shows the black SiC sample; its dimensions are the same of the white SiC specimen. In picture 7.19 is evident the presence of the thermocouple behind the focal area.

Figure 7.17: Black SiC sample

Figure 7.18: Black SiC sample installed in the receiver support

Figure 7.19: Black SiC sample and thermocouple for the measurement of temperature

The experimental tests on the black SiC specimen have been carried out on 17^{th}, 25^{th}, 27^{th}, 31^{st} October 2023 and the outcomes are reported below:

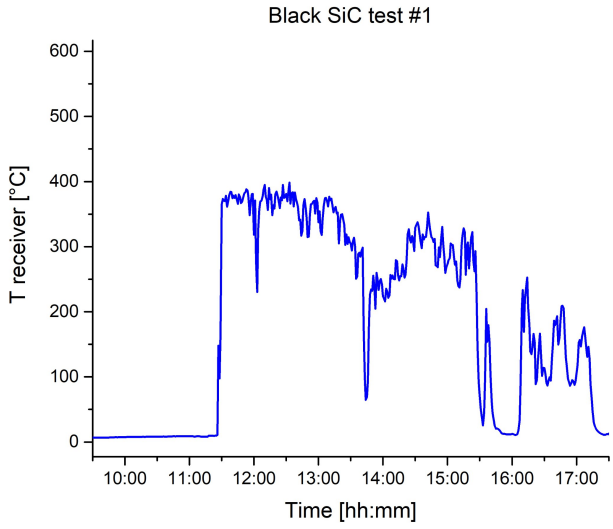

Figure 7.20: First experiment on black SiC sample

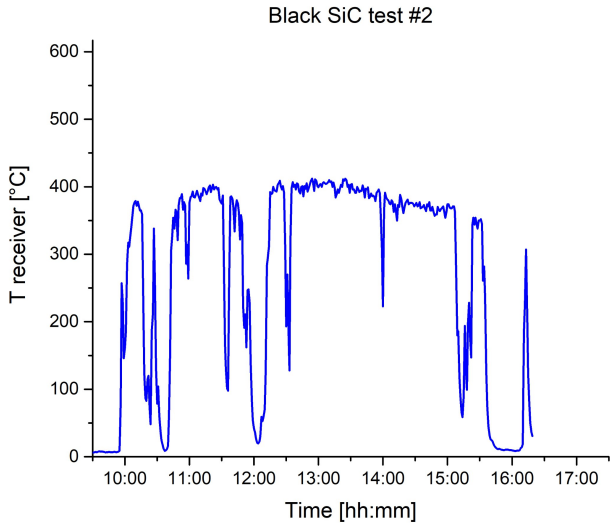

Figure 7.21: Second experiment on black SiC sample

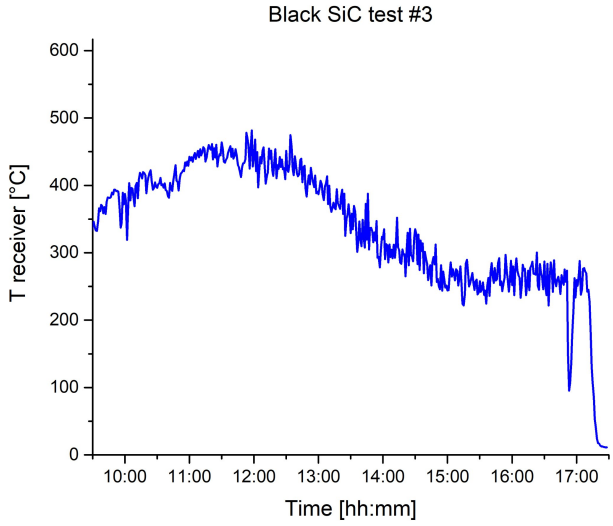

Figure 7.22: Third experiment on black SiC sample

Figures 7.20 and 7.21 show a temperature trend of the specimen characterized by several variations, while pictures 7.22 and 7.23 do not involve significant ΔT during the entire tests.
Table 7.7 sums up the maximum values of temperature achieved by the sample and their related UTC times.

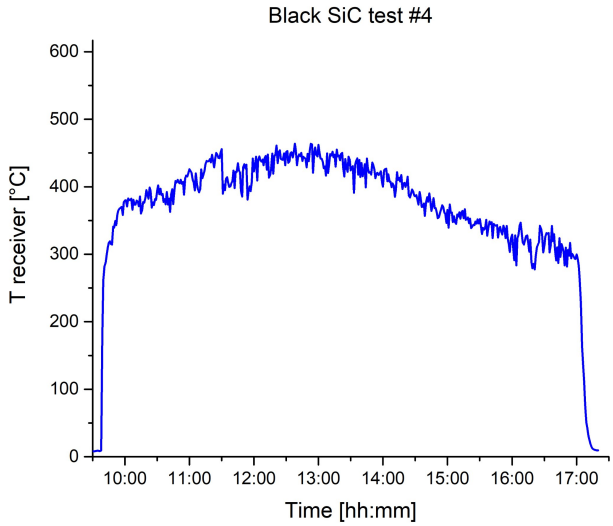

Figure 7.23: Fourth experiment on black SiC sample

Table 7.7: Max T in the four tests

	Max T [°C]	UTC Time
Test #1	398	12:33
Test #2	412	12:54
Test #3	482	11:58
Test #4	464	12:38

Taking into account test #1 and test #2, the most relevant temperature differences are analyzed; in the experiment performed on 17^{th} October 2023 (test #1), it can be noted a quite considerable ΔT equal to 362 °C, occurring in only five minutes, between 11:26 a.m. and 11:31 a.m. The other temperature variations visible in figure 7.20 are much lower than the latter, failing to exceed 300 °C.
On the other hand, the test carried out on 25^{th} October 2023 (test #2) features higher temperature differences; for instance, $\Delta T = 290$ °C in three minutes (10:24 a.m.-10:27 a.m.) and in the afternoon, it can be observed a temperature variation of 312 °C, occurring in 9 minutes, between 15:05 and 15:14. At last, around midday, ΔT reaches 371 °C in twelve minutes (12:03-12:15).

Further thoughts can be made taking into account the meteorological data, in terms of global irradiance and wind speed, made available by the weather station, regarding the days in which the four tests on black SiC specimen were

performed. In particular, the following pictures allow a comparison between the temperature achievable on the sample and the weather conditions.

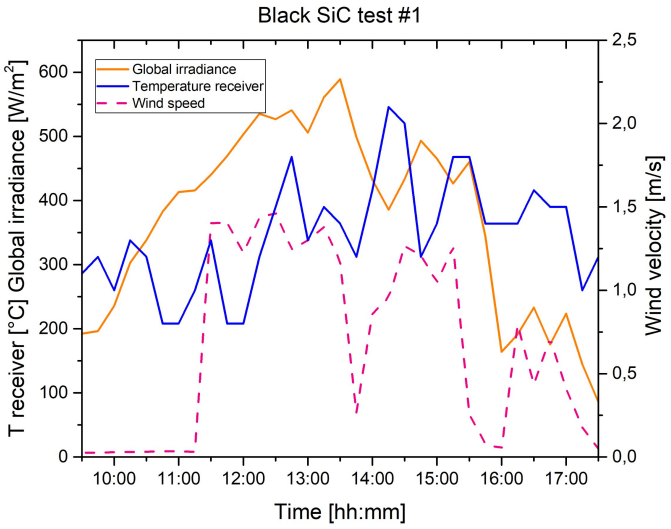

Figure 7.24: Comparison black SiC sample test #1

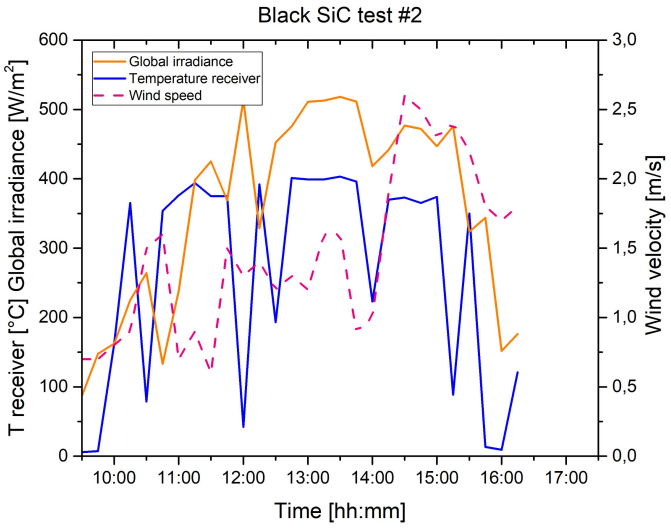

Figure 7.25: Comparison black SiC sample test #2

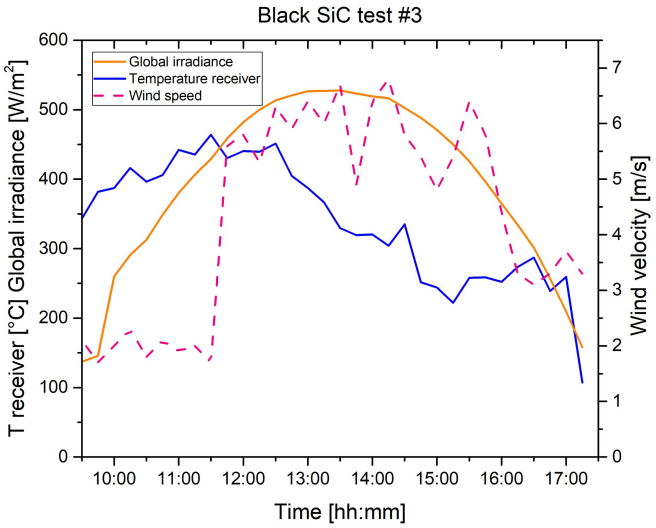

Figure 7.26: Comparison black SiC sample test #3

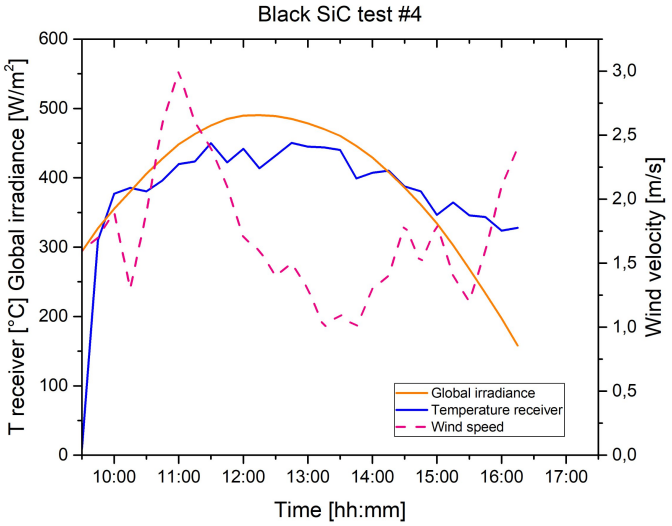

Figure 7.27: Comparison black SiC sample test #4

Taking a look at figure 7.25, the temperature of the receiver follows almost exactly the trend of the global solar irradiance, from 10 a.m. to 4:30 p.m. As already mentioned, the temperature achievable by the specimen strongly depends on the values of wind speed and solar radiation, hence table 7.8 summarizes these latter parameters, recorded on 25^{th} October 2023.

Table 7.8: Main weather parameters of 25^{th} October 2023

25^{th} October 2023	
Gmax [W/m^2]	518
Gmin [W/m^2]	87
Vmax [m/s]	2,6
Vmin [m/s]	0,6

The first temperature peak of 365 °C is recorded at 10:00 a.m. and it is mainly ensured by the low wind velocity (around 0,8 m/s), since the global solar irradiance at the same time is quite poor (about 200 W/m^2). In fifteen minutes (from 11:30 to 11:45) the wind speed increases by 1 m/s, causing a large temperature drop (ΔT = 370 °C), that occurs some minutes later (from 12:00 to 12:15). Indeed, nonetheless the quite high global irradiance of about 500 W/m^2 reached at midday, the effect of the rise in the wind velocity is stronger, decreasing the temperature of the specimen to only 42 °C.
The maximum value of wind speed is 2,6 m/s and it is achieved at 14:30 and then it remains constant for about an hour, leading to another temperature drop: T=374 °C at 15:00 while at 15:30 the temperature recorded is only 88 °C. Thus, only when the value of wind velocity is kept below 1m/s, the temperature of the black SiC specimen is able to reach higher values, such as T=376 °C before midday.

Considering figure 7.26 regarding the experimental test performed on 27^{th} October 2023, it can be noted that the global irradiance follows an interesting trend, typical of clear sky, sunny days, even though the reached values are far lower than the ones of summer season. In this case, the temperature variations recorded are mainly due to changes in the wind speed. In particular, the rise of this latter parameter from 1,7 m/s to 5,6 m/s in only fifteen minutes (11:30-11:45) is responsible for the temperature decrement that already begins at 12:00 and then keps going until the end of the test.

In the end, as noted previously, the quite poor solar irradiance available in the fall season does not allow a complete analysis of the materials' resistance to thermal stresses. Particularly, the above investigation shows a maximum thermal gradient of about 400 °C recorded during the experiments and all the three materials tested were capable of withstanding it. Nonetheless, further experimental assessments should be carried out during the summer months, to obtain a deeper understanding of alumina and silicon carbide ceramics suitability for CSP applications.

Chapter 8

Conclusions and future development

In this work, the reduction of iron oxides in chemical looping process for the production of solar fuels is explored.
At first, a literature review on solar radiation is reported, inevitable to understand the energy source that will be then exploited by concentrated solar power facilities, in particular by parabolic dish systems.
A further investigation is performed as concerns the chemical looping technology, with a focus on iron oxides, which are the inexpensive and environmentally sound oxygen carriers adopted in this work.
Then a first experimental section is shown; a thermogravimetric analysis is performed to evaluate the feasibility of 20 cycles of reduction-oxidation of 40 mg of hematite. Methane is used as reducing agent, whereas carbon dioxide guarantees the following oxidation of the iron ores. The whole test lasts more than 24 hours and the outcomes indicate relevant values of both reduction and oxidation reactivity.
To figure out whether the coupling of the solar dish installed on the Energy Center rooftop and the chemical looping technology is viable, a numerical simulation is performed; in the first place, it investigates the temperatures reached on the solar receiver of the CSP system, observing a temperature of 1300 K on the focal area. In the second place, starting from this latter value, a chemical simulation proves the feasibility of the hematite reduction reaction. The analysis of the gases emitted in 30 minutes witnesses the presence of hydrogen and carbon monoxide production already during the reduction step of the chemical looping. Nonetheless, the elevated operation temperature is also responsible for the undesirable carbon deposition, that deactivates the oxygen carriers.
The receiver-reactor adopted in the numerical analysis is made of alumina and it is afterwards experimentally tested on the parabolic dish of the Energy Center; the

outcomes demonstrate that this material is able to withstand temperature gradients of about 400 °C. Nonetheless, a deeper analysis focused on parameters such as thermal conductivity and thermal shock resistance, shows a low compatibility of Al_2O_3 with the purpose of this work. Hence, several experimental tests are made on two different silicon carbide materials: SiC matrix reinforced with UBE Tyranno S/PyC (black SiC) and SiC matrix reinforced with SiC/BN fibers (white SiC).
Nevertheless, the low global irradiance recorded during the tests (carried out between October and November 2023) does not enable a full understanding of the materials' behaviour when subjected to relevant thermal stresses. In particular, it can be noted that the black SiC is preferable to the white one, thanks to its color that allows it to better mimic the blackbody's capability to harvest solar power.
It can be observed that the use of a mass spectrometer coupled with the TGA analyzer could have made possible a validation of the COMSOL model. In particular, the amount of gases emitted during 30 minutes of reduction, obtained in the numerical analysis, could have been compared to the ones released during the same step in the TGA test.
Another development of this thesis work could involve a valdation of the numerical model performed in COMSOL by means of experimental tests that could prove the feasibility of iron oxides' reduction and their subsequent oxidation. This lats step could hence corroborate and quantify the solar fuel production (either hydrogen or syngas).
Furthermore, there is the strong need to test the silicon carbides specimens during the summer season, to fully assess their high thermal shock resistance and suitability for CSP applications. At that point, the implementation of entire solar receivers made of SiC could make inroads in further experiments.
In addition, future tests could be performed by replacing the iron oxides with the highly promising perovskites, as oxygen carriers. Perovskites are a group of compounds with a peculiar crystal structure, which is described by the chemical formula ABX_3. Particularly, A is represented by a large cation, like alkaline earth or a rare earth metal, B is the site occupied by a small transition metal cation, while X is an anion, resulting in a cubic structure. The profound captivation in perovskites is the possibility of adopting a broad spectrum of elements with unique features to formulate them. This aspect enables the oxygen carrier's characteristics to be adjusted to better suit the demands of a certain utilization.
Among their several advantages, *Othman et al.* highlight an outstanding lattice oxygen mobility, great thermal stability and a strong selectivity towards syngas [88]. Moreover, these materials feature high stability over a broad spectrum of oxygen partial pressure and a strong tendency to react with and convert reducing gases [89].

At last, even though solar chemical looping is still in its early stages, it will surely play a key role in the energy transition, by producing clean fuels, such as

hydrogen and syngas, that can be easily stored and transported for several further applications.

Bibliography

[1] URL: https://climateknowledgeportal.worldbank.org/overview#:~:text=Climate%20change%20is%20the%20significant,change%20from%20natural%20weather%20variability (cit. on p. 1).

[2] URL: https://ourworldindata.org/grapher/temperature-anomaly (cit. on p. 1).

[3] URL: https://www.ipcc.ch/report/ar6/wg3/ (cit. on p. 2).

[4] Hannah Ritchie, Max Roser, and Pablo Rosado. «CO and Greenhouse Gas Emissions». In: *Our World in Data* (2020). https://ourworldindata.org/co2-and-greenhouse-gas-emissions (cit. on pp. 2–4).

[5] URL: https://ourworldindata.org/explorers/climate-change?facet=none&country=OWID_WRL~ATA~Gulkana%2BGlacier~Lemon%2BCreek%2BGlacier~OWID_NAM~South%2BCascade%2BGlacier~Wolverine%2BGlacier~Hawaii&Metric=CO%E2%82%82%2Bconcentrations&Long-run%2Bseries=false (cit. on p. 2).

[6] URL: https://ec.europa.eu/eurostat/statistics-explained/index.php?title=Glossary%3AGlobal-warming_potential_%28GWP%29 (cit. on p. 3).

[7] Hannah Ritchie. «Sector by sector: where do global greenhouse gas emissions come from?» In: *Our World in Data* (2020). https://ourworldindata.org/ghg-emissions-by-sector (cit. on pp. 4, 5).

[8] URL: https://www.consilium.europa.eu/en/5-facts-eu-climate-neutrality/ (cit. on p. 5).

[9] Iea. *Carbon capture, utilisation and storage - energy system*. URL: https://www.iea.org/energy-system/carbon-capture-utilisation-and-storage (cit. on p. 6).

[10] Wikipedia contributors. *Syngas — Wikipedia, The Free Encyclopedia*. 2023. URL: https://en.wikipedia.org/w/index.php?title=Syngas&oldid=1172293990 (cit. on p. 6).

[11] URL: https://fluitron.com/what-is-syngas-and-why-is-it-important/ (cit. on p. 6).

[12] Boyan Kavalov and Stathis Peteves. «Status and Perspectives of Biomass-to-Liquid Fuels in the European Union». In: *European Commission Joint Research Centre EUR* (Jan. 2005) (cit. on p. 6).

[13] Raghda Ahmed El-Nagar and Alaa Ali Ghanem. *Syngas production, properties, and its importance*. Nov. 2019. URL: https://www.intechopen.com/chapters/69842 (cit. on p. 7).

[14] Christos Agrafiotis, Martin Roeb, and Christian Sattler. *A review on solar thermal syngas production via redox pair-based water/carbon dioxide splitting thermochemical cycles*. 2015. DOI: 10.1016/j.rser.2014.09.039 (cit. on pp. 7, 27, 45, 46).

[15] Holly Zell. *Anatomy of the sun*. Mar. 2015. URL: https://www.nasa.gov/mission_pages/sunearth/science/solar-anatomy.html (cit. on p. 8).

[16] Libretexts. *1.1: Blackbody radiation cannot be explained classically*. Apr. 2023. URL: https://chem.libretexts.org/Bookshelves/Physical_and_Theoretical_Chemistry_Textbook_Maps/Physical_Chemistry_%28LibreTexts%29/01%3A_The_Dawn_of_the_Quantum_Theory/1.01%3A_Blackbody_Radiation_Cannot_Be_Explained_Classically (cit. on p. 11).

[17] Matthias Günther, Martin Eickhoff, Tarek Khalil, and Mirko Meyer-Grünefeldt. «Advanced CSP Teaching Materials Chapter 2 Solar Radiation». In: 2011. URL: https://api.semanticscholar.org/CorpusID:51533171 (cit. on pp. 12, 16, 17, 19, 31–34).

[18] URL: https://www.britannica.com/science/solar-constant (cit. on p. 12).

[19] URL: https://www.sws.bom.gov.au/Educational/2/1/12#:~:text=The%20variation%20in%20the%20solar,by%20up%20to%20one%20percent. (cit. on p. 13).

[20] Author links open overlay panelHuashan Li a et al. *Solar constant values for estimating solar radiation*. Feb. 2011. URL: https://www.sciencedirect.com/science/article/abs/pii/S0360544210007565#:~:text=The%20total%20solar%20radiation%20energy,W%2Fm2%20%5B62%5D. (cit. on p. 13).

[21] URL: https://earthobservatory.nasa.gov/features/EnergyBalance/page4.php (cit. on pp. 13, 14).

[22] Jan. 2021. URL: https://www.fondriest.com/environmental-measurements/parameters/weather/photosynthetically-active-radiation/ (cit. on p. 14).

[23] Wikipedia contributors. *Solar irradiance — Wikipedia, The Free Encyclopedia*. 2023. URL: https://en.wikipedia.org/w/index.php?title=Solar_irradiance&oldid=1179356040 (cit. on p. 14).

[24] Santiago Velasquez. *Solar irradiance | ESS explain the difference between DNI, GHI & DIF — essearth.com*. https://www.essearth.com/solar-irradiance/ (cit. on p. 20).

[25] *Solar resource maps of World — solargis.com*. https://solargis.com/maps-and-gis-data/download/world (cit. on p. 20).

[26] *Concentrating Solar Power — nrel.gov*. https://www.nrel.gov/csp/ (cit. on p. 21).

[27] Wikipedia contributors. *Concentrated solar power — Wikipedia, The Free Encyclopedia*. 2023. URL: https://en.wikipedia.org/w/index.php?title=Concentrated_solar_power&oldid=1182964337 (cit. on pp. 21, 31).

[28] Wilfried van Sark and Blanca Corona. «Chapter 12 - Concentrating solar power». In: *Technological Learning in the Transition to a Low-Carbon Energy System*. Ed. by Martin Junginger and Atse Louwen. Academic Press, 2020, pp. 221–231. ISBN: 978-0-12-818762-3. DOI: https://doi.org/10.1016/B978-0-12-818762-3.00012-1. URL: https://www.sciencedirect.com/science/article/pii/B9780128187623000121 (cit. on pp. 21, 22, 24).

[29] Angel G. Fernández, Judith Gomez-Vidal, Eduard Oró, Alan Kruizenga, Aran Solé, and Luisa F. Cabeza. «Mainstreaming commercial CSP systems: A technology review». In: *Renewable Energy* 140 (2019), pp. 152–176. ISSN: 0960-1481. DOI: https://doi.org/10.1016/j.renene.2019.03.049. URL: https://www.sciencedirect.com/science/article/pii/S0960148119303544 (cit. on pp. 21, 27).

[30] Matthias Günther, Michael Joemann, Simon Csambor, Reviewers Amenallah Guizani, Dirk Krüger, and Tobisas Hirsch. *Advanced CSP Teaching Materials Parabolic Trough Technology* (cit. on pp. 22, 35).

[31] Wikipedia contributors. *Andasol Solar Power Station — Wikipedia, The Free Encyclopedia*. 2023. URL: https://en.wikipedia.org/w/index.php?title=Andasol_Solar_Power_Station&oldid=1170267043 (cit. on p. 22).

[32] Ranjit R. Desai. «Thermo-Economic Analysis of a Solar Thermal Power Plant with a Central Tower Receiver for Direct Steam Generation». In: 2013. URL: https://api.semanticscholar.org/CorpusID:107866910 (cit. on p. 23).

[33] Wikipedia contributors. *Fresnel lens — Wikipedia, The Free Encyclopedia*. 2023. URL: https://en.wikipedia.org/w/index.php?title=Fresnel_lens&oldid=1182759667 (cit. on p. 23).

[34] Matthias Günther, Martin Eickhoff, Tarek Khalil, and Mirko Meyer-Grünefeldt¦ *Advanced CSP Teaching Materials Linear Fresnel Technology Author* (cit. on pp. 23, 24).

[35] *Novatec Solar — transfield.com.au*. https://www.transfield.com.au/THfirst60years/21-novatec-solar (cit. on p. 24).

[36] Authors Johannes Sattler et al. *Advanced CSP Teaching Materials Solar Tower Technology* (cit. on pp. 24, 28).

[37] *How does a solar power tower work? — youtube.com*. https://www.youtube.com/watch?v=wg7pv6ZBdeQ&ab_channel=Coxabengoa. [Accessed 20-11-2023] (cit. on p. 25).

[38] https://www.facebook.com/Treehugger. *31 million yearly readers — treehugger.com*. https://www.treehugger.com/environment-4846081. [Accessed 20-11-2023] (cit. on p. 25).

[39] Matthias Günther, Reza Shahbazfar, Reviewers Thomas Fend, and Mohammad Hamdan. *Advanced CSP Teaching Materials Chapter 7 Solar Dish Technology* (cit. on pp. 25, 28, 83).

[40] *7.4. Parabolic Dish CSP Technology | EME 812: Utility Solar Power and Concentration — e-education.psu.edu*. https://www.e-education.psu.edu/eme812/node/648. [Accessed 20-11-2023] (cit. on p. 25).

[41] A.Z. Hafez, Ahmed Soliman, K.A. El-Metwally, and I.M. Ismail. «Design analysis factors and specifications of solar dish technologies for different systems and applications». In: *Renewable and Sustainable Energy Reviews* 67 (2017), pp. 1019–1036. ISSN: 1364-0321. DOI: https://doi.org/10.1016/j.rser.2016.09.077. URL: https://www.sciencedirect.com/science/article/pii/S1364032116305676 (cit. on pp. 25, 35, 36).

[42] *Dish/Engine System Concentrating Solar-Thermal Power Basics — energy.gov*. https://www.energy.gov/eere/solar/dishengine-system-concentrating-solar-thermal-power-basics. [Accessed 20-11-2023] (cit. on p. 26).

[43] by German. *Concentrating Solar Power for Seawater Desalination Final Report AQUA-CSP AQUA-CSP*. URL: http://www.dlr.de/tt/aqua-csp (cit. on p. 26).

[44] Christos Agrafiotis, Henrik Von Storch, Martin Roeb, and Christian Sattler. *Solar thermal reforming of methane feedstocks for hydrogen and syngas production - A review*. 2014. DOI: 10.1016/j.rser.2013.08.050 (cit. on p. 27).

[45] Manuel Romero and Aldo Steinfeld. *Concentrating solar thermal power and thermochemical fuels*. Nov. 2012. DOI: 10.1039/c2ee21275g (cit. on p. 27).

[46] Lee A. Weinstein, James Loomis, Bikram Bhatia, David M. Bierman, Evelyn N. Wang, and Gang Chen. *Concentrating Solar Power*. Dec. 2015. DOI: 10.1021/acs.chemrev.5b00397 (cit. on pp. 29–31, 34).

[47] «Performance Analysis Methodology for Parabolic Dish Solar Concentrators for Process Heating Using Thermic Fluid». In: *IOSR Journal of Mechanical and Civil Engineering (IOSR-JMCE* 12 (1), pp. 101–114. DOI: 10.9790/1684-1212101114. URL: www.iosrjournals.orgwww.iosrjournals.org (cit. on p. 35).

[48] Xing Zhu, Qasim Imtiaz, Felix Donat, Christoph R. Müller, and Fanxing Li. *Chemical looping beyond combustion-a perspective*. Mar. 2020. DOI: 10.1039/c9ee03793d (cit. on pp. 37, 38).

[49] Liang Zeng, Zhuo Cheng, Jonathan A. Fan, Liang Shih Fan, and Jinlong Gong. *Metal oxide redox chemistry for chemical looping processes*. Nov. 2018. DOI: 10.1038/s41570-018-0046-2 (cit. on p. 37).

[50] Anders Lyngfelt and Carl Linderholm. «Chemical-Looping Combustion of Solid Fuels - Status and Recent Progress». In: vol. 114. Elsevier Ltd, 2017, pp. 371–386. DOI: 10.1016/j.egypro.2017.03.1179 (cit. on p. 38).

[51] Saurabh Bhavsar, Michelle Najera, Amey More, and Götz Veser. «Chemical-looping processes for fuel-flexible combustion and fuel production». In: Elsevier Inc., Aug. 2014, pp. 233–280. ISBN: 9780444595782. DOI: 10.1016/B978-0-444-59566-9.00007-7 (cit. on pp. 39, 41, 42).

[52] Hao Zheng, Xiaofeng Jiang, Yanxiu Gao, Andrew Tong, and Liang Zeng. «Chemical looping reforming: process fundamentals and oxygen carriers». In: *Discover Chemical Engineering* 2 (1 July 2022). DOI: 10.1007/s43938-022-00012-3 (cit. on pp. 40, 44, 48).

[53] Ming Luo, Yang Yi, Shuzhong Wang, Zhuliang Wang, Min Du, Jianfeng Pan, and Qian Wang. *Review of hydrogen production using chemical-looping technology*. Jan. 2018. DOI: 10.1016/j.rser.2017.07.007 (cit. on pp. 40, 48).

[54] Paolo Chiesa, Giovanni Lozza, Alberto Malandrino, Matteo Romano, and Vincenzo Piccolo. «Three-reactors chemical looping process for hydrogen production». In: *International Journal of Hydrogen Energy* 33 (9 May 2008), pp. 2233–2245. ISSN: 03603199. DOI: 10.1016/j.ijhydene.2008.02.032 (cit. on pp. 40, 41).

[55] Massimo Santarelli. *Polygeneration and advanced energy systems - Chemical looping*. 2022 (cit. on pp. 41, 45).

[56] URL: https://www.uigi.com/oxygen.html (cit. on p. 43).

[57] Mohammad Saghafifar, Matthias A. Schnellmann, and Stuart A. Scott. «Limits of performance of chemical looping air separation in packed bed coupled with electricity production». In: *International Journal of Greenhouse Gas Control* 118 (July 2022). ISSN: 17505836. DOI: 10.1016/j.ijggc.2022.103668 (cit. on p. 43).

[58] Behdad Moghtaderi. «Application of chemical looping concept for air separation at high temperatures». In: vol. 24. Jan. 2010, pp. 190–198. DOI: 10.1021/ef900553j (cit. on p. 43).

[59] Yoran De Vos, Marijke Jacobs, Pascal Van Der Voort, Isabel Van Driessche, Frans Snijkers, and An Verberckmoes. *Development of stable oxygen carrier materials for chemical looping processes—A review*. Aug. 2020. DOI: 10.3390/catal10080926 (cit. on p. 43).

[60] Bo Wei, Reza Fakhrai, Bahram Saadatfar, Gowtham Mohan, and Torsten Fransson. «The design of a solar-driven catalytic reactor for CO2 conversions». In: vol. 57. Elsevier Ltd, 2014, pp. 2752–2761. DOI: 10.1016/j.egypro.2014.10.307 (cit. on p. 44).

[61] Juan Adánez, Alberto Abad, Francisco García-Labiano, Pilar Gayán, Luis F de Diego, and Miguel Luesma Castán. *Progress in Chemical-Looping Combustion and Reforming Technologies. A review*. 2012 (cit. on p. 44).

[62] Stéphane Abanades. *A Review of Oxygen Carrier Materials and Related Thermochemical Redox Processes for Concentrating Solar Thermal Applications*. May 2023. DOI: 10.3390/ma16093582 (cit. on pp. 45, 46, 48).

[63] Srirat Chuayboon, Stéphane Abanades, and Sylvain Rodat. «Solar chemical looping gasification of biomass with the zno/zn redox system for Syngas and zinc production in a continuously-fed solar reactor». In: *Fuel* 215 (2018), pp. 66–79. DOI: 10.1016/j.fuel.2017.11.021 (cit. on p. 46).

[64] Jiawei Hu, Vladimir V. Galvita, Hilde Poelman, and Guy B. Marin. *Advanced chemical looping materials for CO2 utilization: A review*. July 2018. DOI: 10.3390/ma11071187 (cit. on pp. 46–48, 59).

[65] Zhongliang Yu, Yanyan Yang, Song Yang, Qian Zhang, Jiantao Zhao, Yitian Fang, Xiaogang Hao, and Guoqing Guan. *Iron-based oxygen carriers in chemical looping conversions: A review*. Apr. 2019. DOI: 10.1016/j.crcon.2018.11.004 (cit. on p. 48).

[66] Rouzbeh Ramezani, Luca Di Felice, and Fausto Gallucci. «A review of chemical looping reforming technologies for hydrogen production: recent advances and future challenges». In: *JPhys Energy* 5 (2 Apr. 2023). ISSN: 25157655. DOI: 10.1088/2515-7655/acc4e8 (cit. on p. 48).

[67] Shiwei Ma, Shiyi Chen, Ahsanullah Soomro, and Wenguo Xiang. «Effects of CeO2, ZrO2, and Al2O3 Supports on Iron Oxygen Carrier for Chemical Looping Hydrogen Generation». In: *Energy and Fuels* 31 (8 Aug. 2017), pp. 8001–8013. ISSN: 15205029. DOI: 10.1021/acs.energyfuels.7b01141 (cit. on p. 48).

[68] Dec. 2022. URL: https://en.wikipedia.org/wiki/Thermogravimetric_analysis (cit. on p. 49).

[69] URL: https://analyzing-testing.netzsch.com/en (cit. on pp. 50–52).

[70] Esmail R. Monazam, Ronald W. Breault, Ranjani Siriwardane, George Richards, and Stephen Carpenter. «Kinetics of the reduction of hematite (fe2o3) by methane (CH4) during chemical looping combustion: A global mechanism». In: *Chemical Engineering Journal* 232 (2013), pp. 478–487. DOI: 10.1016/j.cej.2013.07.091 (cit. on pp. 53, 56, 58, 70–74, 76).

[71] *Heat Transfer Module User's Guide*. 1998. URL: www.comsol.com/blogs (cit. on pp. 65, 68).

[72] Sergey Vyazovkin and Wolfgang Linert. *Kinetic Analysis of Reversible Thermal Decomposition of Solids* (cit. on p. 71).

[73] Zhiyuan Chen, Christiaan Zeilstra, Jan van der Stel, Jilt Sietsma, and Yongxiang Yang. «Reduction Mechanism of Fine Hematite Ore Particles in Suspension». In: *Metallurgical and Materials Transactions B: Process Metallurgy and Materials Processing Science* 52 (4 Aug. 2021), pp. 2239–2252. ISSN: 10735615. DOI: 10.1007/s11663-021-02173-y (cit. on p. 75).

[74] Eliodoro Chiavazzo. *Energy Storage - Sensible TES*. 2021 (cit. on p. 75).

[75] *Rate constant | chemistry — britannica.com*. https://www.britannica.com/science/rate-constant. [Accessed 21-11-2023] (cit. on p. 76).

[76] *6.2.3.1: Arrhenius Equation — chem.libretexts.org* (cit. on p. 77).

[77] Chunqiang Lu, Kongzhai Li, Hua Wang, Xing Zhu, Yonggang Wei, Min Zheng, and Chunhua Zeng. «Chemical looping reforming of methane using magnetite as oxygen carrier: Structure evolution and reduction kinetics». In: *Applied Energy* 211 (2018), pp. 1–14. ISSN: 0306-2619. DOI: https://doi.org/10.1016/j.apenergy.2017.11.049. URL: https://www.sciencedirect.com/science/article/pii/S0306261917316343 (cit. on pp. 77, 78).

[78] J.T. Slycke, E.J. Mittemeijer, and M.A.J. Somers. «1 - Thermodynamics and kinetics of gas and gas–solid reactions». In: *Thermochemical Surface Engineering of Steels*. Ed. by Eric J. Mittemeijer and Marcel A.J. Somers. Oxford: Woodhead Publishing, 2015, pp. 3–111. ISBN: 978-0-85709-592-3. DOI: https://doi.org/10.1533/9780857096524.1.3. URL: https://www.sciencedirect.com/science/article/pii/B978085709592350001X (cit. on pp. 77, 78).

[79] El.Ma. srl Electronic Machining. *Use and maintenance manual of the solar dish concentrator (manuale di uso e manutenzionedel concentratore solare a disco)* (cit. on pp. 82–84).

[80] Honghong Su, Guohui Hou, Zhiqiang Cheng, Biao Xia, Xufei Fang, Bo Yan, and Xue Feng. «Thermal shock resistance of alumina ceramics enhanced by nanostructured conformal coatings using metal–organic frameworks». In: *Scripta Materialia* 119 (2016), pp. 38–42. ISSN: 1359-6462. DOI: https://doi.org/10.1016/j.scriptamat.2016.03.020. URL: https://www.sciencedirect.com/science/article/pii/S1359646216300951 (cit. on pp. 84, 89).

[81] Oluseyi P. Oladijo, Samuel A. Awe, Esther T. Akinlabi, Resego R. Phiri, Lebudi L. Collieus, and Rebaone E. Phuti. «High-Temperature Properties of Metal Matrix Composites». In: *Encyclopedia of Materials: Composites*. Ed. by Dermot Brabazon. Oxford: Elsevier, 2021, pp. 360–374. ISBN: 978-0-12-819731-8. DOI: https://doi.org/10.1016/B978-0-12-819724-0.00096-3. URL: https://www.sciencedirect.com/science/article/pii/B9780128197240000963 (cit. on pp. 84, 85).

[82] Great Ceramic. *Why use aln ceramics?* June 2023. URL: https://great-ceramic.com/thermal-shock-resistance-of-technical-ceramics/ (cit. on p. 85).

[83] *Advantages of sic thermal shock resistance*. Oct. 2022. URL: https://resources.system-analysis.cadence.com/blog/msa2021-advantages-of-sic-thermal-shock-resistance (cit. on p. 85).

[84] URL: https://www.ceratech.co.jp/en/product/material/alumina/a9951s/ (cit. on p. 85).

[85] Amjad S. Almansour and Gregory N. Morscher. «Tensile creep behavior of SiCf/SiC ceramic matrix minicomposites». In: *Journal of the European Ceramic Society* 40.15 (2020), pp. 5132–5146. ISSN: 0955-2219. DOI: https://doi.org/10.1016/j.jeurceramsoc.2020.07.012. URL: https://www.sciencedirect.com/science/article/pii/S0955221920305677 (cit. on p. 90).

[86] Maolin Chen, Ling Pan, Xiaodong Xia, Wei Zhou, and Yang Li. «Boron nitride (BN) and BN based multiple-layer interphase for SiCf/SiC composites: A review». In: *Ceramics International* 48.23, Part A (2022), pp. 34107–34127. ISSN: 0272-8842. DOI: https://doi.org/10.1016/j.ceramint.2022.07.021. URL: https://www.sciencedirect.com/science/article/pii/S0272884222024087 (cit. on p. 90).

[87] URL: https://elib.dlr.de/141449/1/pamm.202000202.pdf (cit. on p. 95).

[88] Nur Hidayati Othman, Norhasyimi Rahmat, Nur Hashimah Alias, and Fauziah Marpani. «15 - Composite perovskite-based material for chemical-looping steam methane reforming to hydrogen and syngas». In: *Hybrid Perovskite Composite Materials*. Ed. by Imran Khan, Anish Khan, Mohammad Mujahid Ali Khan, Shakeel Khan, Francis Verpoort, and Arshad Umar. Woodhead Publishing Series in Composites Science and Engineering. Woodhead Publishing, 2021, pp. 315–333. ISBN: 978-0-12-819977-0. DOI: https://doi.org/10.1016/B978-0-12-819977-0.00015-9. URL: https://www.sciencedirect.com/science/article/pii/B9780128199770000159 (cit. on p. 103).

[89] Lei Liu, Zhenshan Li, Yang Wang, Zuoan Li, Yngve Larring, and Ningsheng Cai. «Industry-scale production of a perovskite oxide as oxygen carrier material in chemical looping». In: *Chemical Engineering Journal* 431 (2022), p. 134006. ISSN: 1385-8947. DOI: https://doi.org/10.1016/j.cej.2021.134006. URL: https://www.sciencedirect.com/science/article/pii/S1385894721055790 (cit. on p. 103).